CAPILLARY PHENOMENA IN POROUS MEDIA: PORE AND GRAIN SCALE STUDIES

A Dissertation
Presented to
The Academic Faculty

by

Zhonghao Sun

In Partial Fulfillment
of the Requirements for the Degree
Doctor of Philosophy in the
School of Civil and Environmental Engineering

Georgia Institute of Technology
August 2018

CAPILLARY PHENOMENA IN POROUS MEDIA: PORE AND GRAIN SCALE STUDIES

Approved by:

Dr. J. Carlos Santamarina, Advisor
School Civil and Environmental Engineering
Georgia Institute of Technology

Dr. Sheng Dai
School of Civil and Environmental Engineering
Georgia Institute of Technology

Dr. J. David Frost
School of Civil and Environmental Engineering
Georgia Institute of Technology

Dr. Guillermo Goldsztein
School of Mathematics
Georgia Institute of Technology

Dr. Susan E. Burns
School of Civil and Environmental Engineering
Georgia Institute of Technology

Date Approved: May 4, 2018

ACKNOWLEDGEMENTS

Many people have offered support and suggestions over the last five years; I own thanks to you all. I want to thank my Ph.D. advisor, Carlos Santamarina, for providing me such a great opportunity and wonderful time in my life. I am deeply grateful for his persevering guidance and support. Experiences of working with him taught me valuable lessons, both professional and personal.

I thank my thesis committee members, Dr. Susan E. Burns, Dr. J. David Frost, Dr. Sheng Dai, and Dr. Guillermo Goldsztein, for valuable comments and suggestions. Special thanks to Dr. J. David Frost for generous support.

I am grateful to Qi Liu and Junbong Jang for the time we worked together. The collaboration helped me deepen my insight of capillary phenomena and broaden my thinking of doing research. I thank Budi Zhao for assisting me fabricate the microchip and Gabrielle Abelskamp for polishing my writing.

It is my privilege to work with a group of good friends and colleagues in the Particulate Media Research Laboratory and the Energy Geo-Engineering Laboratory; I am indebted to you all. Special thanks to Junghee Park, Liang Lei, Xunchang Fei, and Yuanjie Shen for enriching my work and life. I am grateful to my friends in Atlanta for the support.

Finally, I thank my parents and family for the unconditional love and support that always go along with me.

TABLE OF CONTENTS

LIST OF TABLES

LIST OF FIGURES

SUMMARY

Multiphase flow is a common phenomenon in porous media in both natural and industrial processes such as hydrocarbon recovery, geological CO_2 storage, remediation of contaminated ground, and flow in unsaturated soils. Capillary phenomena play a critical role in determining flow regimes, residual fluid distribution, displacement efficiency, and all forms of fluid-solid interactions. This study aims to advance the physical understanding of key capillary phenomena in porous media by using pore-scale and bench-scale experiments complemented with physical and mathematical analyses.

The non-cylindrical pore geometry has profound effects on multiphase flow. The non-circular transverse pore geometry ensures the connectivity of wetting fluids along pore edges and corners. On the other hand, the converging-diverging longitudinal pore geometry results in non-constant capillary pressures across pore constrictions; interfacial instabilities such as Haines jumps and snap-offs may take place in this case. The evolution of instabilities depends on nearby interacting menisci.

Surfactants and particles adsorb to the fluid-fluid interface and change interfacial characteristics such as the interfacial tension and the contact angle. Transient changes in the surfactant surface density in converging-diverging pores alter capillary phenomena. The shell-like mechanical property of particle-coated interfaces results in profoundly different displacement behavior in pores and abnormal fingering instabilities as observed in Hele-Shaw cells.

The interfacial tension resists the capillary pressure between immiscible fluids, and it transfers the tension onto the grains. These forces may create openings that facilitate the migration of the non-wetting fluid in deformable porous media such as sediments. Opening-mode discontinuities vary from cavities to fractures depending on the stress state, the mechanical properties of sediments, and the invaded volume.

CHAPTER 1. INTRODUCTION

1.1 Motivation

Sediments consist of a granular skeleton and pores filled with fluids. Therefore, sediments are inherently porous and pervious, and fluids are often multi-phase. Developments in geotechnical engineering have enabled the construction of advanced and intricate urban facilities and infrastructure by focusing primarily on engineering the granular skeleton.

Emerging issues related to energy and the environment, however, require an increased research effort to understand and engineer multi-phase flow in soils and rocks. The efficient displacement of immiscible fluids is critical to oil and gas recovery, hydrate bearing sediments, geological CO_2 storage, and the remediation of contaminated ground.

Capillary phenomena controls multiphase flow in porous media and the response of the granular skeleton. This thesis aims to develop a fundamental understanding of key capillary phenomena in porous media. These include the effect of pore geometry on flow, instabilities, displacement of particle-coated interfaces, gas-sediment interactions, and long-term pore filling. These phenomena are studied at the pore and pore-network scales using laboratory experiments, and are further analyzed with physically-based mathematical models.

1.2 Thesis Organization

The thesis is organized into 9 chapters. It starts with an overview of capillary phenomena in porous media (*Chapter 2*), followed by six chapters, each of which focuses on a specific phenomenon.

One key feature of pore spaces in sediments is the non-uniform geometry. *Chapter 3* investigates the effect of non-cylindrical pore geometry on capillary pressure and displacement across a pore throat, with or without the presence of surfactants. This chapter builds on earlier work by fellow PhD student Junbong Jang.

Following the various pore-scale instabilities observed in *Chapter 3*, *Chapter 4* explores the mechanisms behind one relevant type of instability, i.e. Haines jumps. It identifies three underlying mechanisms and discusses the possibility of manipulating this type of instabilities.

Results in *Chapter 4* suggest that the displacement behavior is different when the interfacial characteristics change. Therefore, *Chapter 5* focuses on the mechanical response of nanoparticle-coated interfaces. This study involves a collaboration with fellow PhD student Qi Liu.

Chapter 6 investigates the effect of particle-coated interfaces on flow in pores and in Hele-Shaw cells. Abnormal fingering patterns are reported and analyzed by a physical model which considers the adsorption of particles onto the interface.

Chapter 7 explores the effect of time. It documents a long-term experimental study of non-conductive pore filling phenomena which is relevant to prolonged displacement.

Pore spaces are assumed undeformable in the previous chapters. *Chapter 8* uses the transparent soil technique to visualize and investigate pressurized gas-sediment interactions during gas migration in soft sediments.

Finally, *Chapter 9* concludes with salient findings and implications.

CHAPTER 2. AN OVERVIEW OF CAPILLARY PHENOMENA IN POROUS MEDIA

2.1 Introduction

Multiphase fluids are ubiquitous in porous media and play a critical role in a wide range of applications, such as infrastructure, resource recovery, agriculture, atmosphere-subsurface interaction, and biological systems. Examples from the field of energy-geoengineering include: oil and gas recovery, contamination by non-aqueous phase liquids NAPL and environmental remediation (dense DNAPL: heavy oils, coal tars; light LNAPL: gasoline and supercritical CO_2), methane hydrate bearing sediments, geological storage of CO_2 and backfill in nuclear waste repositories. These examples involve gases (air, vapor, methane), supercritical fluids (e.g., CO_2), liquids (water, brine, oil and contaminants), and even solids (e.g., hydrate).

Capillary phenomena in porous media control the distribution of phases and residual saturation, determine relative permeability and flow regimes, impact effective stress and mechanical properties of porous media, and are responsible for a wide range of emergent phenomena – from lung collapse to desiccation cracks in mud ponds. Although the basic laws of capillarity are well understood, complexities arise in porous media and natural systems, in part due to multi-scale geometric effects and physical couplings. The purpose of this manuscript is to explore the wealth of capillary phenomena in porous media and to identify emergent phenomena with emphasis on energy geo-engineering applications.

2.2 Fundamental Concepts

Two contiguous phases in equilibrium experience incessant jumping of molecules from one phase to the other (limited by their mutual solubilities), and differences in attractive molecular interactions within each phase. These apply to all mixed-phase systems such as air-water, methane-water, brine-oil and hydrate-water.

2.2.1 Surface/Interfacial Tension

Surface tension results from differences in attractive interactions that occur between molecules at the interface and molecules within the bulk fluids away from the interface (Figure 2.1 (a)). Surface tension γ is the work per unit area required to increase the interface area [J/m^2] or the force per unit length the interfacial "membrane" exerts [N/m].

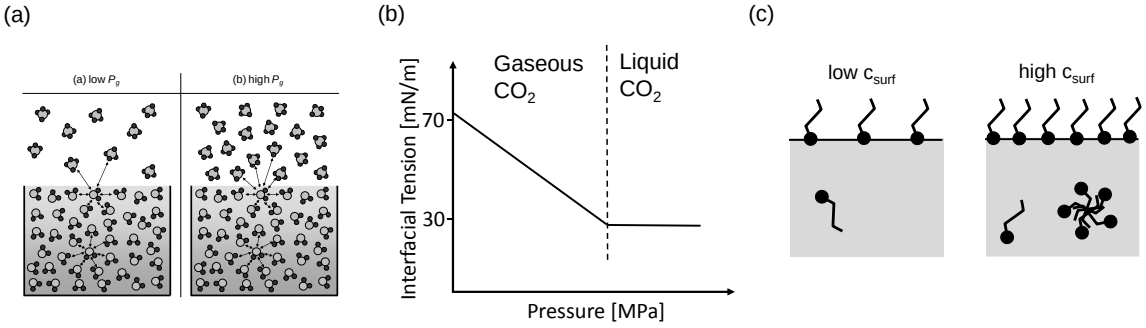

Figure 2.1. Interfacial tension. (a) Molecular-scale attractive interactions. (b) Pressure dependency in gas-liquid systems (data in Espinoza and Santamarina, 2010). (c) The effect of surfactants.

Temperature. In general, the surface tension decreases with the increase in temperature due to the increased molecular vibration relative to attraction forces. An asymptotic linear trend describes changes near stable conditions $\gamma = \alpha - \tau T$. For example, the

rate of change τ=0.1477 (mN/m)/°C for air-water surface tension at p=1atm [Jasper, 1972]. Some water-alcohol mixtures exhibit surface tension that increases with temperature [Karapetsas et al., 2014].

Pressure. Higher gas pressure implies higher gas density and molecular attractive interactions at the interface. Hence, the gas-liquid interfacial tension decreases with increasing gas pressure, and remains fairly constant once the gas liquefies at the vapor-liquid boundary (Figure 2.1 (b)). For example, the interfacial tension for water-CO_2 at 25°C is [Massoudi and King, 1974; see Chalbaod et al., 2009 for brine-CO_2]:

$$\gamma\left[mN/m\right] = 71.98 - 0.7789\,u_{CO_2}/atm + 0.00543\,u_{CO_2}^2/\mathrm{atm}^2 - 0.000042\,u_{CO_2}^3/\mathrm{atm}^3 \qquad (2.1)$$

Salt. The gas-water interfacial tension increases with salt concentration because of increased attractive interactions among hydrated ions in the water solution. The asymptotic change in surface tension at low salt concentration c<1 M is a linear trend $\gamma=\alpha+\chi c$; for example, the rate of change is χ=1.55 (mN/m)/M for NaCl solution [Weissenborn and Pugh, 1996; see Chalbaud et al., 2009 for brine-CO_2].

Surfactants. "Surface active agents" have an amphipathic structure with both hydrophobic and hydrophilic ends so they tend to migrate towards interphases (Figure 2.1 (c)). Surfactants that remain in the bulk solution eventually form micelles when the concentration reaches the critical micelle concentration CMC. Surfactants at the interface align and repel each other decreasing the surface tension. Hence, the interfacial tension decreases with surfactant concentration until excess surfactants in the bulk solution form micelles beyond the CMC [Holmberg et al., 2003; Rosen, 2004; Israelachvili, 2011].

Excess charges. Water can gain excess charge by charge separation between water and the solid surface [Choi et al., 2013]. Excess charges repel each other and migrate towards the droplet outer surface where their repulsion causes a decrease in the surface tension proportional to the surface charge [experimental evidence in Santos et al., 2011].

Marangoni effect. Sudden changes in surface concentration or temperature cause transient gradients in the surface tension, and the interfacial membrane contracts towards the area with the higher surface tension.

Time-dependent changes. The interfacial tension adjusts as fluids dissolve into each other until they reach equilibrium. For example, the initial interfacial tension of water-air decreases by almost 20% in a water-benzene-air system as benzene dissolves in water.

2.2.2 Wettability and Contact Angle

Wettability is the relative affinity that interacting fluids exhibit towards a solid substrate. The contact angle θ the fluid interface defines against the solid surface characterizes wettability, and it captures the force-equilibrium among the interfacial tensions that arise between the fluids V and L and the solid S [Figure 2.2 (a)]:

$$\cos\theta = \frac{\gamma_{VS} - \gamma_{LS}}{\gamma_{LV}} \qquad \textit{Young's equation} \tag{2.2}$$

The fluid on the lower side of the LV-interface is more affine to the solid.

Spreading coefficient. Consider a three-fluid system, such as air-oil-water. An oil droplet may spread on water to form a thin oil slick on the ocean surface, or a thin oil film around water-wet pores as air invades the porous medium. The spreading coefficient

captures the balance between interfacial tensions in this three-fluid system (o=oil, w=water, and a=air – Figure 2.2 (b)):

$$C_S = \gamma_{aw} - (\gamma_{ow} + \gamma_{ao}) \tag{2.3}$$

Oil will spread as a thin film between air and water when C_S>0. If $C_S < 0$, the three phases reach equilibrium at a contact angle θ [Zhou and Blunt, 1997]. Oil production by gas-enhanced gravity drainage presumes oil spreading within the pores of water-wet reservoirs [Blunt et al., 1995].

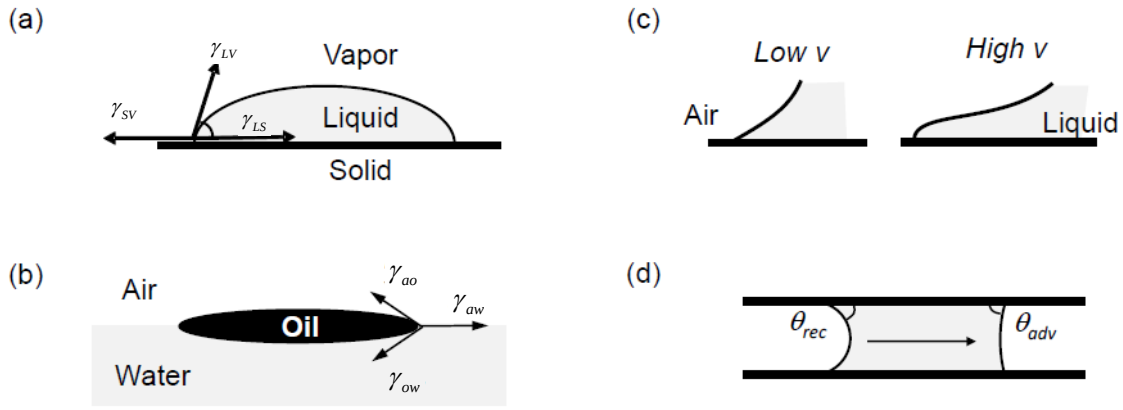

Figure 2.2. Contact angle. (a) Equilibrium between interfacial tensions in a two fluids on solid substrate. (b) Spreading in three-fluid system. (c) Dynamic effects. (d) Hysteresis.

Surface tensions - Pressure. Changes in interfacial tension discussed in the previous section affect the contact angle in agreement with Young's equation. This is readily seen in liquid-gas-mineral systems such as water-CO_2-mineral and water-CH_4-mineral where the gas-liquid interfacial tension γ_{LV} decreases with gas pressure [data in Espinoza and Santamarina, 2010].

Dynamic contact angle. The contact angle is velocity-dependent; in particular, the advancing contact angle increases as the velocity increases [Figure 2.2 (c) – data in Sobolev et al., 2000]. Molecular-scale explanations consider the kinetics of molecular attachment and detachment. Hydrodynamic explanations take into consideration viscous dissipation near the contact line and remnant films [Blake, 2006; Snoeijer and Andreotti, 2013]. A wetting transition takes place when the invading fluid advances at a high speed and a film of the defending fluid remains behind [Podgorski et al., 2001; Snoeijer and Andreotti, 2013; Hsu and Hilpert, 2015].

Contact angle hysteresis - Changes in wettability. Typically, the contact angle is different when the interface advances or recedes (Figure 2.2 (d)). Underlying processes can be both chemical (changes in the surface chemistry during invasion and preferential adsorption of species) and geometrical features that can "pin" the contact line at submicron scale surface roughness and heterogeneities [Butt et al., 2003; de Gennes et al., 2004; Quere, 2008]. Mineral surfaces tend to be water-wet relative to organic liquids and gases. However, wettability can change with the selective absorption of chemical compounds in oil and brines (e.g., surfactants, resins and asphaltenes). Temperature and pressure conditions (unclear trends - Buckley et al., 2001), time and kinetic rates and the saturation history affect trends [Kovscek et al., 1993; Powers and Tamblin, 1995; Powers et al., 1996; Buckley et al., 1998; Francisca and Santamarina, 2003; Drummond and Israelachvili, 2004; Abdallah et al., 2007].

2.2.3 *Capillarity*

The tensile membrane that separates two fluids can sustain a pressure difference. From force equilibrium, the pressure difference or capillary pressure Δp is proportional to the interfacial tension γ_{LV} and the contact angle θ (Young-Laplace equation):

$$\Delta p = p_V - p_L = \gamma_{LV}\left(\frac{1}{r_1}+\frac{1}{r_2}\right) \tag{2.4}$$

where the interface curvature has two principal radii r_1 and r_2.

2.2.4 *Interacting Menisci*

Interfaces in porous media are not isolated; in fact, all menisci are interconnected through the fluid phase. Analytical and experimental results support the following observations [Alvarellos, 2003]: (1) Contact angles θ_i at interacting menisci are not constant but vary between the upper and lower bound contact angles established at the verge of advancing and receding motions, $\theta_{rec} \le \theta_i \le \theta_{adv}$. (2) Menisci respond to external forces within this range of contact angles. (3) Menisci geometry throughout the medium minimize the total energy.

For example, consider a droplet of a wetting fluid in a capillary tube (Figure 2.3 (a)). If the tube lies flat, contact angles are the same at both ends; the value is within the range $\theta_{rec} \le \theta_i \le \theta_{adv}$ depending on the droplet formation history. As the tube is inclined, gravity adds the droplet self-weight, the contact angle at the lower end starts evolving towards θ_{adv} and towards the receding θ_{rec} at the upper end. The limiting values θ_{adv} and θ_{rec} determine the maximum biasing force the droplet can exert (a function of self-weight

and inclination). Clearly, the droplet in an inclined tube is inherently unstable in the absence of contact angle hysteresis $\theta_{adv}=\theta_{rec}$ [Alvarellos, 2003].

Interaction through the vapor pressure. Liquids are in equilibrium with their vapor at LV interfaces. The vapor pressure at equilibrium p_v is curvature r dependent [Kalikmanov, 2013]:

$$\ln\left(\frac{p_V}{p_{sat}}\right)=\frac{2T_S\Omega}{k_BTr} \qquad \textit{Laplace-Kelvin equation} \qquad (2.5)$$

where p_{sat} is the saturated vapor pressure for the bulk liquid, Ω is the liquid molecular volume, k_B=1.38 × 10^{-23} J/K is Boltzmann's constant, and T is temperature. Differences in equilibrium vapor pressure promote mass transport between pores of different sizes and wettability, as indicated in Figure 2.3 (b); this is a form of Ostwald ripening. Depending on pore size and geometry, water may fill small cavities and form plugs at pore throats leaving isolated inner and larger pores; this contributes to hysteresis during adsorption and desorption [Camuffo, 1984].

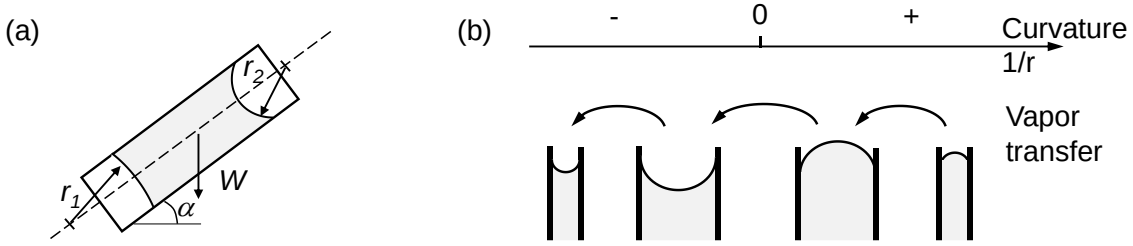

Figure 2.3. Interacting menisci. (a) Response to external bias (b) Interaction through vapor pressure.

2.3 Pore Geometry

Models based on cylindrical pore geometries capture the prevalent role of pore size on mixed fluids in porous media. However, these models fail to represent other important phenomena that result from the non-cylindrical longitudinal and transverse geometry of natural pores.

2.3.1 Longitudinal Pore Geometry (Details in Chapter 3)

Pervious porous media consist of concatenated pore throats-and-bodies (e.g., sediments and rocks) or lacunae-and-canaliculi (e.g., bones). Let's consider a sinusoidal pore throat geometry. Figure 2.4 (a) presents the change in capillary pressure computed using the Young-Laplace equation as the fluid interface transverses the pore throat. In all cases, capillary pressure scales with surface tension, however, it is the contact angle that plays a more critical role: the interface may jump from concave-to-convex for intermediate contact angles with an associated reversal in capillary pressure. In fact, a partially wetting fluid may have to be "pushed" to go beyond the pore throat. Note that pressure maxima or minima do not occur at the pore throat except when θ=0.

Pore Geometry and Surfactants. Transient changes in the surfactant surface density when the interface traverses the pore throat alter the interfacial response; then, the measured capillary pressures deviate from values predicted using the bulk surfactant concentration [Jang et al., 2016]. Similar transient changes underlie the role of surfactant self-regulation during pulmonary expansion and contraction [Clements et al., 1958].

2.3.2 Transverse Pore Geometry

Laplacian capillarity anticipates remnant wetting fluids in small pores, corners, crevices and edges after the pore has been invaded by a non-wetting fluid. Therefore, the wetting phase is prone to remain connected in porous media even at relatively high capillary pressures. Phase connectivity has important implications for fluid transport [Roof, 1970; Arriola et al., 1983; Ransohoff and Radke, 1988a; Dong and Chatzis, 1995; Bico and Quere, 2002]

Corners. Figure 2.4 (b) shows a wetting fluid resting along corners. The Mayer and Stowe-Princen MS-P solution predicts the pressure difference Δp between the non-wetting fluid and the remnant wetting fluid at corners in terms of the perimeter of the contact line between the nonwetting fluid and the solid l_s, the perimeter of the contact line between the non-wetting fluid and the wetting fluid l_γ, and the cross-section area of the non-wetting fluid A_{eff} [Mason and Morrow, 1991; Ma et al., 1996; Mason and Morrow, 1994; Lago and Araujo, 2001]:

$$\Delta p = \frac{\gamma_{LV}\left(l_s \cos\theta + l_\gamma\right)}{A_{eff}} \tag{2.6}$$

Edges. The fluid interface can be stable at various contact angles when the solid surface has high curvature at edges. This implies a range of possible capillary pressures for equilibrium when edges are present [Figure 2.4 (c); Morrow, 1970].

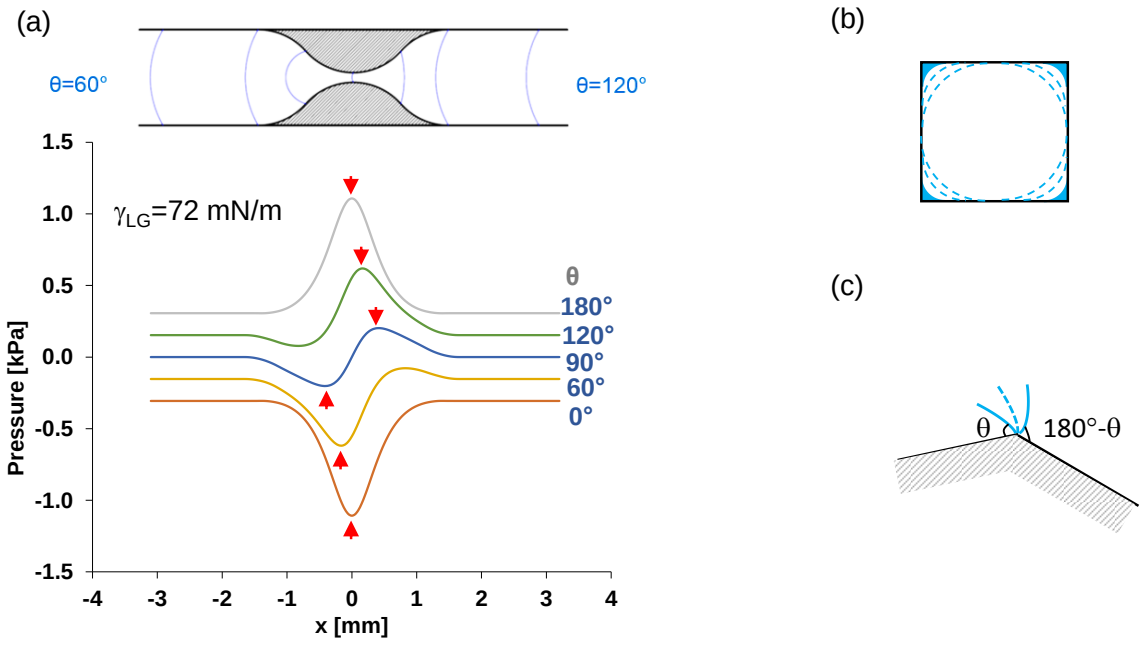

Figure 2.4. Pore geometry. (a) Longitudinal variation [Jang et al., 2016]. (b) Transverse variation. (c) Contact angle at edges.

2.4 Instabilities

2.4.1 Pore-scale Instabilities (Details in Chapter 4)

Pore geometry and capillary phenomena combine to give rise to various accelerations and instabilities as the fluid interface approaches or recedes away from a pore throat. These instabilities are associated with sudden changes in capillary pressure and often result in phase separation and entrainment [Figure 2.5 (a); Jang et al., 2016]:

- *Haines jump*. Spontaneous fluid redistribution after a sudden pressure change [Morrow, 1970; Mohanty et al., 1987; Gauglitz and Radke, 1989; Furuberg et al., 1996; Berg et al., 2013].
- *Snap-off/choke-off*. A wetting fluid plug forms at a pore throat and splits the traversing non-wetting fluid. Plugs may involve wetting fluids transported along corners and

crevices or left behind during sudden jumps [Roof, 1970; Wardlaw, 1982; Arriola et al., 1983; Yu and Wardlaw, 1986a, b; Ransohoff et al., 1987; Pena et al., 2009].

- *Lamellae and foam generation* due to repeated snap-offs [Ransohoff and Radke, 1988b; Rossen, 2003].

These instabilities contribute to fluid trapping during displacement, whereby a single displacement front becomes a multi-interface front, overall flow is hindered, and measured capillary pressures deviate from theoretically predicted values and become system-dependent [Lenormand et al., 1983].

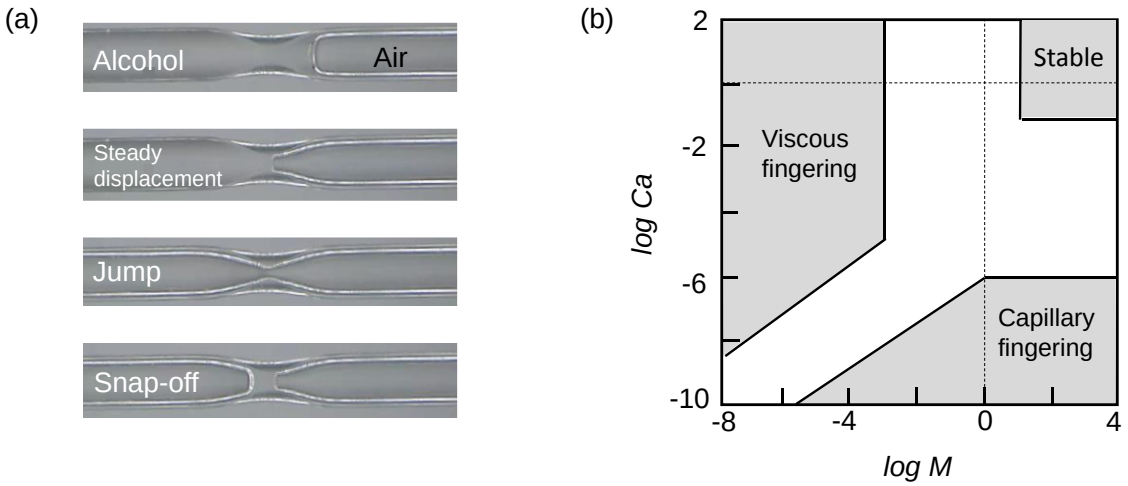

Figure 2.5. Instabilities. (a) Pore-scale: jumps and snap-offs (Details in Chapter 3). (b) Macro-scale: fingered invasion (Schematic – after Lenormand et al., 1988).

2.4.2 Macro-scale Instabilities

Consider an invading fluid advancing into a porous medium saturated with a defending fluid. The invasion pattern reflects wettability, mass densities, and viscosities. These parameters are captured in dimensionless ratios between capillary F_c, drag F_d and buoyant F_b forces:

Capillary Number: $Ca = \mu_{inv} v / \gamma$

Viscosity Ratio: $M = \mu_{inv} / \mu_{def}$

Figure 2.5 (b) illustrates different displacement regimes: stable displacement, viscous fingering and capillary fingering. Experimental and numerical studies show that the boundaries between the various invasion regimes are system-dependent [Lenormand et al., 1988; Zhang et al., 2011].

2.5 Pressure-Saturation Characteristic Curve

The capillary pressure-saturation relationship, also known as the soil-water characteristic curve or soil water retention curve, defines the relationship between capillary pressure and the degree of saturation. This relationship plays a central role in modeling unsaturated soil behavior. Pressure-saturation data contains information that relates to the pore size distribution, pore connectivity and spatial correlation. Consequently, the characteristic curve affects the evolution of relative permeabilities, resource recovery, mechanical stability and deformation [Brooks and Corey, 1964; van Genuchten, 1980; Fredlund, 2000].

The pressure-saturation characteristic curve rests between two bounds. The lower bound corresponds to the pressure required for the non-wetting fluid to invade all pores aligned in series according to size starting from the largest pore. The upper bound is defined by the pressure required to invade the smallest pore (Figure 2.6 (a)).

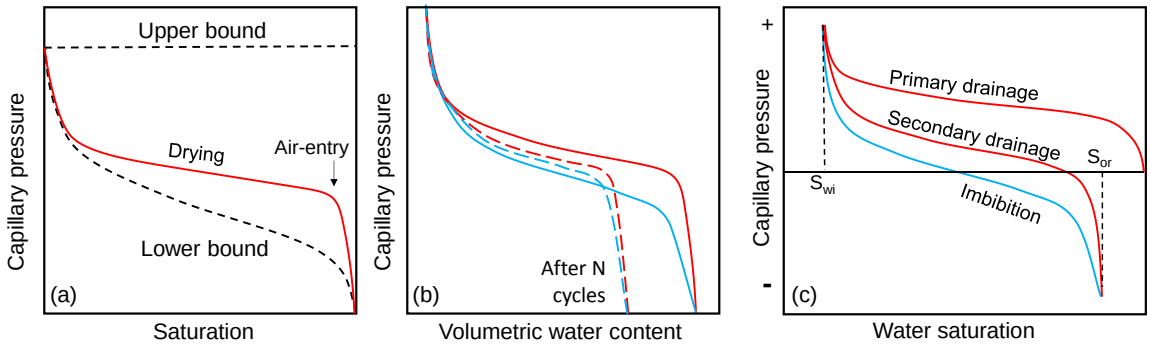

Figure 2.6. Pressure-saturation characteristic curve. (a) Typical trend and bounds. (b) Hysteretic behavior and asymptotic trend after wetting cycles and associated volume changes. (c) Change in wettability.

2.5.1 Spatial Distribution, Volumetric Strains and Hysteresis

Pore network topology, short-term instabilities and long-term fluid migration through the vapor phase lead to a non-homogenous distribution of defending and invading fluids.

Percolation. The moment when a fluid phase forms a continuous path between inlet and outlet defines the percolation saturation. Percolating paths are fractal and ensuing material properties are specimen-size dependent.

Spatial variability. The wetting fluid tends to remain in regions surrounded by small pores (e.g., water in silts next to sands), while hydrates nucleate preferentially within large pores (e.g., sand layers in thin-coarse stratigraphies). Spatial variability and correlation have a pronounced effect on the evolution of mixed-fluid conditions, hinder environmental remediation and leave behind either trapped or bypassed oil and gas during resource recovery [Le et al., 2012].

Patchiness. Often isolated, non-percolating "patches" rather than homogeneously distributed fluids should be expected between percolation thresholds and in the pendular regime. Patchy distribution results in transport and mechanical properties that are different to those when phases are homogeneously-randomly distributed [Dai et al., 2012; Dai and Santamarina, 2013].

Fines migration. Fines may migrate with the interface between immiscible fluids and accumulate at pore throats and at interparticle contacts (e.g., clay grains form stabilizing bridges between sandy grains in loess). Clogging of pore throats favor the formation of an internal vuggy structure during gas exsolution, and gas-driven fractures during desiccation [Jung et al., 2012].

Plastic strains and pore structure. Changes in suction *s* associated to changes in saturation *S* cause plastic volumetric strains ε_v and disturbs the pore structure, the degree of saturation and the pressure-saturation characteristic curve [Kodikara et al., 1999; Gallipoli et al., 2003; Wheeler et al., 2003; Khalili et al., 2008; Tarantino, 2009].

$$dS = \frac{\partial S}{\partial s} ds + \frac{\partial S}{\partial \varepsilon_V} d\varepsilon_V \tag{2.7}$$

Figure 2.6 (b) presents the characteristic curve for a constant porous structure and for the same medium when fabric changes take place.

Hysteresis. The characteristic curve shows hysteretic behavior during wetting and drying, in part due to contact angle hysteresis, the non-homogeneous spatial distribution of fluids, plastic strains and fines migration addressed above (Figure 2.6 (b)). Other pore-scale processes involved in hysteresis include: the "ink-bottle" effect when large pore

bodies are connected through small pore throats, capillary condensation, entrapped air, and changes in pore structure caused by the precipitation of insoluble phases.

2.5.2 Time: From Diffusion to Dynamics (Details in Chapter 7)

The standard capillary pressure-saturation relationship presumes thermodynamic equilibrium. However, measurements are often conducted in short-time laboratory scales. Gas diffusion plays a critical role on long-term pore filling and changes in saturation with time [Sun et al., 2017]. Furthermore, non-equilibrium conditions develop during advective regimes, and pressure-saturation trends become flow-rate dependent [Diamantopoulos et al., 2012; Hassanizadeh et al., 2002]. The saturation of the wetting fluid at a given capillary pressure increases with the velocity of the invading non-wetting fluid.

2.5.3 Changes in Wettability

The relative preference between fluids and a solid substrate may change over time. In fact, while most minerals are water wet, they may become oil-wet or mixed-wet during the life of the reservoir due to the adsorption or precipitation of organic molecules onto the mineral surface [Anderson, 1986; Buckley et al., 1998]. Therefore, the capillary pressure $\Delta p = p_{oil} - p_{water}$ is positive $\Delta p > 0$ during oil invasion (i.e., reservoir formation), it becomes negative $\Delta p < 0$ when the process is reversed (i.e., during oil production – Figure 2.6 (c)). Wettability can be characterized from spontaneous and forced water imbibition or drainage [Morrow, 1990; Abdallah et al., 2007].

2.6 Gas Invasion vs. Internal Gas Nucleation

Typically, the immiscible fluid invades from the boundary and remains a continuous phase. However, this is not always the case: gas can nucleate inside the porous medium and form isolated bubbles (e.g., bio-mediated gas nucleation, microbial decomposition of organic matter, depressurization and gas exsolution, hydrate dissociation). Similarly, isolated hydrate crystals nucleate inside sediments.

2.6.1 Gas Pressure

Consider gas either invading or nucleating inside a water-saturated sediment. In both cases: (1) the interfacial membrane wets grains and resists the advancing gas front, (2) grains are pulled back away from the advancing gas front, (3) the effective stress acting on grains that have been invaded by the gas phase is lower than the effective stress in the water-saturated grains, and (4) the capillary pressure $\Delta p = p_{gas} - p_{water} > 0$. However, while gas and liquid pressures are boundary-controlled during invasion, only the liquid pressure is boundary-controlled during internal gas nucleation (Figure 2.7).

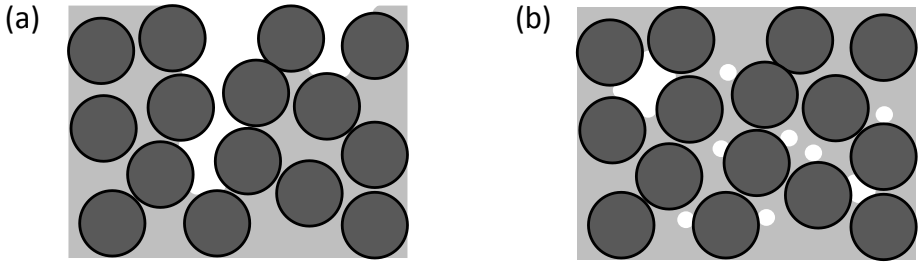

Figure 2.7. Unsaturation by (a) gas invasion and (b) internal gas nucleation.

Preferential nucleation takes place in larger pores. Bubble growth after nucleation is limited by the pore throats that surround a given bubble. Therefore, different bubbles

will have different transient gas pressures, contrary to the constant gas pressure in gas invasion. Eventually, bubbles become much larger than the grain size, encounter a similar statistical distribution of pore throats, and develop similar gas pressures even while they remain isolated [Jang and Santamarina, 2011, 2014].

The isolated gas phase may form (1) displacive gas bubbles without sediments inside (high air entry value sediment subjected to low effective stress), or (2) sediment-filled gas patches (either low gas entry value and/or high effective stress).

2.6.2 Physical Properties

Gas invasion and internal gas nucleation result in distinctly different mixed-fluid patterns within the porous medium. Ensuing differences in physical properties follow.

Pressure-saturation characteristic curve. Let's assume a single capillary pressure for all gas patches, and compare the ensuing capillary pressure vs. saturation curves obtained in gas nucleation and in gas invasion. Numerical results obtained using pore network modeling with constant pore structure show similar trends in both cases [Jang and Santamarina, 2014].

Relative permeabilities. The trends for relative gas and water permeabilities vs. saturation are also very similar, except for a lower gas permeability in gas nucleation than in invasion near the percolation threshold [Jang and Santamarina, 2014].

Bulk stiffness – P-wave velocity. The bulk stiffness of water-gas mixtures decreases rapidly as the gas content increases [Sills et al., 1991; analysis in Santamarina et

al., 2001]. In the case of gas nucleation, the analysis must consider the gas pressure in isolated bubbles or gas patches, and its effect on the gas bulk stiffness κ_b:

$$\kappa_b = \frac{2\gamma}{3r} \text{ (Bulk stiffness of gas bubbles)} \tag{2.8}$$

Therefore, the bulk stiffness of a fluid κ_f such as water κ_w in the presence of gas bubbles is

$$\kappa_f = \frac{1}{S\frac{1}{\kappa_w} + (1-S)\frac{3 \cdot r}{2 \cdot \gamma}} \tag{2.9}$$

where S is the water saturation. Changes in saturation are readily detected using P-wave velocity measurements [Rebata-Landa and Santamarina, 2012].

Consolidation. Displacive gas bubbles (i.e., no sediments inside) readily contract in response to changes in confinement and cause immediate volume compaction. Note: contraction is limited by stress arching around bubbles [Sills et al., 1991; Puzrin et al., 2011]. Later, gas dissolution into the liquid and pressure diffusion or consolidation contribute to time-dependent volume contraction.

Shear strength. The internal nucleation of gas bubbles weakens the shear strength of soils [Sills et al., 1991; Sills and Wheeler, 1992]. On the one hand, displacive gas bubbles have no shear strength. On the other hand, sediments trapped in gas patches experience a lower effective stress than the surrounding water-saturated sediment and contribute a proportionally lower shear strength.

2.7 Interparticle Force—Open Mode Discontinuities (Details in Chapter 8)

The forces between grains in a granular packing saturated by a single phase fluid system respond to effective stresses imposed at the boundaries. However, a new contribution to interparticle forces emerges when the granular medium is filled with a mixed fluid. (Olivier Coussy's valuable contributions to unsaturated poroelasticity and crystallization are documented in Coussy, 2010, Coussy and Monteiro, 2007, Coussy, 2007, Coussy and Brisard, 2009).

2.7.1 Capillary Forces

The interfacial membrane hangs on to grain surfaces, and transfers its interfacial tension to each grain. In turn, the grain transfers this new force F_{cap} to granular skeleton (Figure 2.8 (a)). Therefore, the distribution of interparticle forces in a mixed fluid system depends both on the externally applied stresses and the internal distribution of the phases. The asymptotic solution for the interparticle contact force due to capillarity F_{cap} is [see also Cho and Santamarina, 2001]

$$F_{cap} = 2\pi\, d\, \gamma \tag{2.10}$$

For comparison, the weight of the particle W scales with d^3 and skeletal forces N due to effective stress scale with d^2. Therefore, capillary forces gain relevance for small particles d subjected to low effective stress σ'.

Clearly, the distribution of interparticle forces will be quite different for gas invasion and gas nucleation even at the same degree of saturation. From this perspective,

effective stress concepts and constitutive models must be carefully constructed to address these distinct conditions.

2.7.2 Open Mode Discontinuities (Details in Chapter 8)

Capillary forces cause particle displacement and changes in the pore structure. The most common observation is the volume contraction associated to the increase in suction. Open mode discontinuities develop when capillary forces F_{cap} exceed skeletal forces N induced by the effective stress imposed at boundaries (Figure 2.8 (b)). As noted above, this should be expected in fine grained sediments with high air entry value and subjected to low effective stress, under both invasion and nucleation conditions.

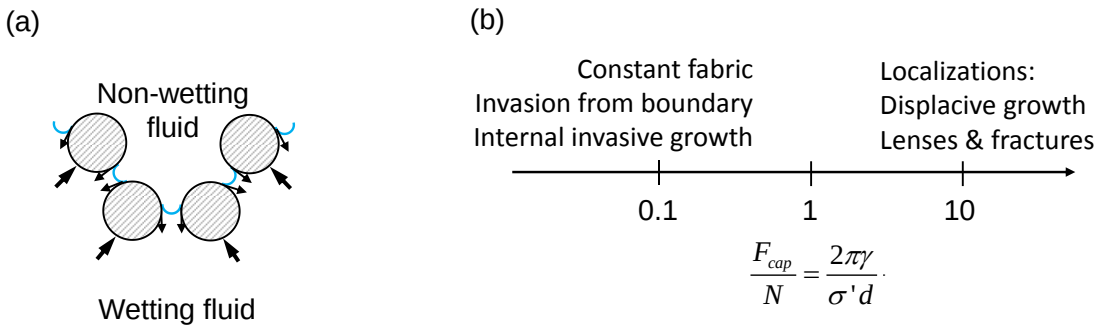

Figure 2.8. Capillary forces and hydro-mechanical coupling. (a) Intergranular capillary forces. (b) Open mode discontinuities in fine grained granular materials subjected to low effective stress.

Invasion: Desiccation Cracks. The decrease of water content causes the increase of capillary suction and consolidation of porous media. As the suction increases further, the air-water interface invades the largest pores and causes particle displacement away from the invasion point. As a result, the void ratio at the crack tip increases and the crack propagates. It should be noted that the effective stress is in compression everywhere during

the crack initiation and propagation [Shin and Santamarina, 2010; Shin and Santamarina, 2011a, b]. A similar situation takes place in other systems, such as at the contact between a water-saturated clay and CO_2 [Espinoza and Santamarina, 2012].

Internal nucleation: from displacive bubbles to fractures (or from nodules to lenses). Similarly, internal nucleation such as gas exsolution can displace grains, as noted above. Enlarging cavities evolve into opening-mode fractures that are aligned transversely to the minimum effective stress. The nucleation and growth of other immiscible phases follows similar patterns, starting as nodules and eventually forming lenses; examples include hydrate bearing clayey sediments, frozen ground, and mineral precipitates.

2.8 Conclusions

Mixed fluid conditions give rise to a wide range of phenomena in porous media. These phenomena and emergent processes have profound implications in soil-atmosphere interaction, energy geotechnology related to oil and gas recovery, CO_2 geological storage and environmental contamination/remediation.

Even the basic concepts of surface tension and contact angle require careful analyses. Surface tension depends on pressure (in gas-liquid systems), temperature, changes in solute concentration, and surfactant concentration. Contact angle responds to interfacial tensions, surface topography (it may exhibit a range of values at edges), invasion velocity, and chemical fluid-substrate interactions (it may change with time). Interfaces are not isolated, but they interact through the fluid pressure in response to external fields such as gravity.

The idealized cylindrical representation of pores fails to capture important capillarity effects. The converging-diverging geometry of pore throats causes jumps and snap-off instabilities. Surfactants may experience transient changes in surface density during dynamic events and the capillary response across a pore constriction will deviate from the signature anticipated for quasi-static conditions. Corners and edges favor the percolation of wetting liquids.

Ubiquitous pore-scale instabilities compound with macroscale instabilities associated to viscous and capillary effects to intensify fluid trapping. The spatial variability and correlation in the pore structure aggravates this situation. Consequently, instabilities and spatial variability diminish the recovery efficiency.

The saturation-pressure characteristic curve is saturation-history and flow-rate dependent, it is coupled with the mechanical response of the porous medium through changes in pore-structure, and it may change with time as a consequence of fluid-substrate reactions and long-term diffusion. Its hysteretic response gradually evolves towards a terminal condition when the medium is subjected to multiple wetting-drying cycles.

Time emerges as an important variable in mixed-fluid conditions. Common quasi-static analysis fail to capture the consequences of chemical reactions and rate processes, viscous effects, and long-term diffusive transport.

There are salient differences between unsaturation by internal gas nucleation and gas invasion, and the ensuing physical properties of the porous medium. Gas bubbles are isolated and may have different gas pressures, interparticle forces decrease and the porous medium tends to expand during internal gas nucleation. During gas invasion, the gas phase

is continuous and it has the same pressure, capillary forces add to interparticle forces and the porous medium tends to contract. Open mode discontinuities may develop in both cases when the capillary entry pressure is high relative to the effective stress: displacive bubbles grow to form internal fractures during internal gas nucleation, and desiccation cracks form during gas invasion.

CHAPTER 3. IMMISCIBLE DISPLACEMENT IN A SINGLE PORE—EFFECT OF CONVERGING-DIVERGING PORE GEOMERTY AND SURFACTANTS

3.1 Introduction

A gas-liquid or a liquid-liquid interface invades a pore when the pressure difference between the two fluids overcomes the capillary pressure. Capillarity controls the migration and distribution of non-aqueous contaminants in soils and fractured rocks, and subsequent remediation strategies for both LNAPLs and DNAPLs [Essaid et al. 1993; Glass et al., 2000; Mulligan et al., 2001; Saenton et al., 2002; Reddy and Saichek, 2003; Li et al., 2005; Daniel et al., 2015; Essaid et al. 2015], gas migration, air invasion and desiccation of near-surface soils [Gens, 2010; Likos and Lu, 2004; Lu and Likos, 2004; Shin and Santamarina, 2010], gas and oil recovery [Iglauer et al., 2010; Hirasaki et al., 2011; Johannessen and Spildo, 2013], and CO_2 injection and geological storage [Pruess and Garcia, 2002; Nordbotten et al., 2005; Kim and Santamarina, 2014].

The capillary pressure P_c [Pa] in a cylindrical pore of radius r [m] depends on the contact angle θ and the interfacial tension γ_{lg} [N/m] between the two fluids as predicted by Young-Laplace's equation $P_c=2\gamma_g\cdot\cos\theta\cdot r^{-1}$, where $\cos\theta=(\gamma_s-\gamma_{gs})/\gamma_{gl}$ relates the interfacial tensions that arise between the two fluids 'g and l' and the solid 's'. Surface tension and contact angle are affected by interfacial conditions, roughness, wettability, gas pressure, impurities, and surfactants [De Gennes, 1985; Sharma and Ross, 1991; Kwok and Neumann, 2000; Miwa et al., 2000; Siebold et al., 2000; Espinoza and Santamarina, 2010].

Furthermore, both surface tension and contact angle vary as the system changes from static to dynamic conditions (Static interfacial tension: Young, 1805; Good, 1966; Vargaftik et al., 1983. Dynamic interfacial tension: Caskey and Barlage, 1971; Bechtel et al., 2002. Static vs. dynamic wettability: Wenzel, 1936; Cassie and Baxter, 1944; Rose and Heins, 1962; Hoffman, 1975; De Gennes, 1985). In non-cylindrical tubes, capillary pressure and fluid invasion reflect the irregular cross-section of pores as well as their converging-diverging longitudinal geometry [Mason and Morrow 1994; Ransohoff and Radke, 1988a; Dong and Chatzis, 1995; Weislogel and Lichter, 1998; Bico and Quere, 2002; Song and Kovscek, 2015; Zhao et al., 2016].

Capillary forces, viscous forces and inertial forces combine to determine capillary rise [Thomson, 1886; Washburn, 1921; Siebold et al., 2000; Xue et al., 2006], displacement patterns in multiphase flow in porous media [Chatzis and Dullien, 1983; Stokes et al., 1986; Lenormand et al., 1988; Sandnes et al., 2011; Holtzman et al., 2012; Trojer et al., 2015], and various pore-scale phenomena and instabilities such as Haines jumps, snap-offs, lamella and foam generation.

Surfactants hinder the development of capillary pressure and facilitate mixed-phase fluid flow in porous media. Surfactants tend to migrate towards gas-liquid ‘gl’ interfaces because of their amphipathic structure with hydrophobic and hydrophilic ends (Figure 3.1 (a)). Surface tension decreases with increased surfactant concentration on the interface until the bulk solution reaches the critical micelle concentration CMC, and it remains constant thereafter as the excess surfactant in the bulk solution forms micelles – Figure 3.1 (b) [Defay and Prigogine, 1949; Miller et al., 1994; Holmberg et al., 2003; Rosen, 2004; Israelachvili, 2011]. The surfactant density on the interface homogenizes rapidly, driven

by the surface tension gradient created by heterogeneous concentrations, i.e., Marangoni effect [Scriven and Sternling, 1960; Schramm and Wassmuth, 1994; Nikolov et al., 2002; Tadmor, 2009; Still et al., 2012]. In addition to the adsorption onto gas-liquid 'gl' interfaces, surfactants adsorb onto liquid-solid 'ls' and gas-solid 'gs' interfaces as well; therefore, the effect of surfactants on cos θ is not limited to the inverse of γ_{gl} (Chen and Mohanty, 2013). Adsorption at interfaces and micelle formation affect the efficiency of surfactants in engineered applications that range from the remediation of NPAL contaminated sites to enhanced oil recovery.

Surfactant adsorption and interfacial concentration are time-dependent and may evolve in response to changes in pore geometry (Figure 3.1 (c)). The pulmonary surfactant is an example of a bio-engineered system that exploits this effect: surfactant concentration and surface tension vary as alveoli expand and contract facilitating breathing [Clements et al., 1958; Ghadiali and Gaver, 2000; Gerber et al., 2006; Nakahara et al., 2010]. The relevance of this geometry-dependent rate effect in porous media such as sediments remains unknown.

This chapter reports pressure signatures gathered as fluid interfaces traverse a constriction in a cylindrical capillary tube during advancing and receding tests. The study explores the effect of surfactant concentration, infers transient changes in surfactant concentration at the interface, and identifies pore-scale instabilities.

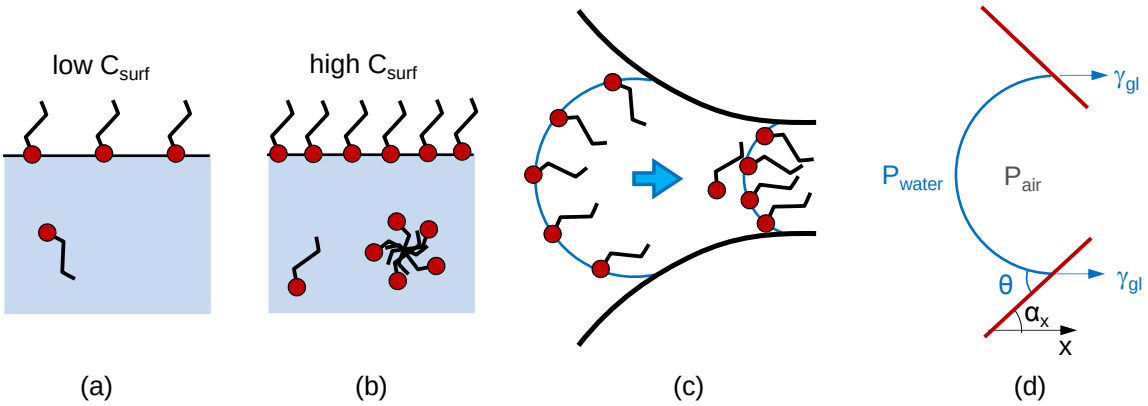

Figure 3.1. Surfactant interactions at the molecular scale. (a) Preferential adsorption at interfaces. (b) Micelle formation in the bulk solution. (c) Hypothesized transient change in surfactant surface density as the interface traverses the pore constriction. (d) Interface between two fluids at a non-cylindrical pore geometry.

3.2 Methods

Three fluids were tested in this study: deionized water, ethanol, and aqueous surfactant solutions prepared with sodium dodecyl sulfate (SDS). The deionized water is milli-Q water. Ethanol is from VWR International, and sodium dodecyl sulfate is from Fisher Scientific. SDS solutions reach the critical micelle concentration at CMC≈2.4mg/g, in agreement with surface tension values in Table 3.1.

Pore-scale tests were conducted using 75mm long borosilicate capillary tubes with internal diameter ID=0.97mm. A constriction was formed by localized heating and rotation to reach a minimum diameter at the pore throat (constriction length ~3mm; ID=0.33 mm – Figure 3.2). The nominal pore throat size ID≈0.3 mm reflects the trade-off between detailed visualization and pressure signature amplitude, and it is an upper bound for fluid flow passages in sandy sediments and sandstones (Fredrickson et al., 1997; Bloomfield et al., 2001; Bennion and Bachu 2006; Minagawa et al., 2008). In the dimensionless space of

governing parameters, conditions tested in this study apply to those described in Table 3.2 which are within the range of many real field situations, from NAPL remediation to resource recovery.

The constricted capillary tube was connected to a micro-control 5mL syringe through a stainless steel tube. A pressure transducer (OMEGA, PX209) mounted next to the inlet was used to monitor the liquid pressure. A stereo microscope (ZEISS, Stemi 2000-CS) above the capillary tube recorded the evolving interface. The general test configuration is sketched in Figure 3.2.

Table 3.1. Experimental study: Fluids

Liquid	Concentration of Surfactant in Water [mg/g]	γ_{gl} [mN/m]	Contact Angle – SDS [°] *	
		SDS♥	Advancing	Receding
Water	n/a	72	72	51
aqueous surfactant solution	0.025	72	73	48
	0.05	71	73	35
	0.1	70	71	31
	0.25	65	70	28
	0.5	57	69	28
	1.0	46	53	25
	2.5	37	28	25
	5.0	37	26	25
	10.0	37	26	25
	25.0	37	25	24
alcohol	n/a	24	33	30

Note: the critical micelle concentration of Sodium dodecyl sulfate SDS is CMC=2.4mg/g at 25°C.

♥ From Prosser and Franses (2001) – see also Mysels (1986)

∗ Measured for water and SDS solutions using images before the necking. Flow rate of 40µl/hr and a front speed of 15µ/s.

Table 3.2. Experimental study: Flow rate and dimensionless ratios Re and Ca calculated for water

Flow Rate [μL/hr]	Velocity [μ/s]	Reynolds Number Re*	Capillary Number Ca†
20	7.5	8×10^{-3}	0.94×10^{-7}
40	15	16×10^{-3}	1.88×10^{-7}
80	30	32×10^{-3}	3.76×10^{-7}
160	60	64×10^{-3}	7.52×10^{-7}

Note: *The Reynolds number *Re* compares inertial and viscous forces $Re = 2\rho vr/\mu$

†The capillary number *Ca* compares viscous and capillary forces $Ca = \mu v/\gamma_{lg}$

Parameters: fluid velocity v [m/s], pore radius r=0.485 mm, fluid density ρ=1000 kg/m^3, fluid viscosity μ=0.9x10^{-3} Pa·s, liquid-gas surface tension γ_{lg}=0.072N/m

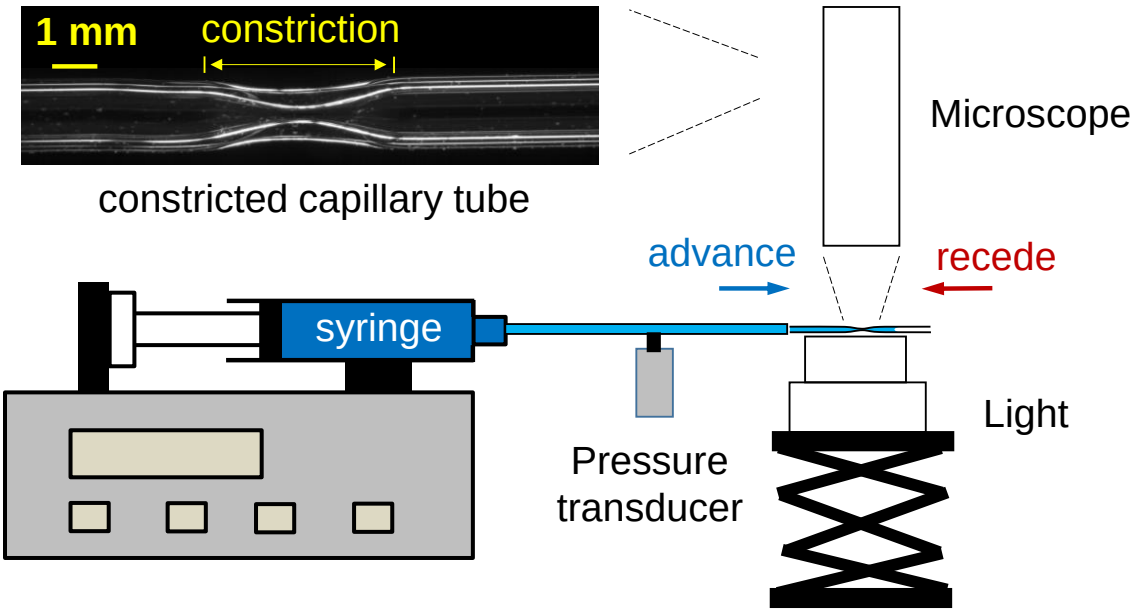

Figure 3.2. Experimental configuration used to study capillary effects in a constricted capillary tube (micro-photograph shown in the inset). Injection flow rates vary from q=20 to 160μL/hr. See flow conditions in Table 3.2.

The syringe pump maintained the preselected flow rate constant during both advancing and receding tests. Imposed flow rates are summarized in Table 3.2. Propagation velocities and the values of Reynolds number *Re* and capillary number *Ca* for water are included in the table; flow conditions remain in the same Reynolds and capillary number *Re*-*Ca* regime for all tests conducted in this study (see *Re* and *Ca* values in Table 3.2). Tests were conducted with deionized water first, then alcohol, and finally with surfactant solutions run from the lowest to the highest concentration. Each test consisted of multiple receding-advancing cycles at incrementally higher flow rates.

3.3 Results

Pressure-time P-t signatures and concurrent images are recorded for all fluids and injection rates as the liquid-gas interface traverses the tube constriction. The measured pressure is the pressure difference between the liquid and the air, i.e., the negative value of the capillary pressure. Figure 3.3 (a) and 3.3 (b) present typical gathered pressure signatures and selected snapshots for an advancing test and a receding test, respectively. During the advance of a water-air interface, the interface accelerates before reaching the pore throat, moves slowly at the pore throat, and bursts suddenly passing the throat. During the receding test for ethanol, the interface advances slowly towards the pore throat and jumps suddenly after it passes the narrowest point. A residual film of ethanol forms a liquid plug immediately after the jump. The liquid experiences repetitive snap-offs and the formation of plugs that block air invasion at the pore throat. These liquid plugs regenerate very fast, producing oscillatory pressure cycles with a frequency that is proportional to the imposed flow rate, this means that plug formation is faster than the pressure build-up (for

the range of flow rates tested in this study). The accelerations and jumps of the interface are accompanied by sudden pressure changes in pressure signatures.

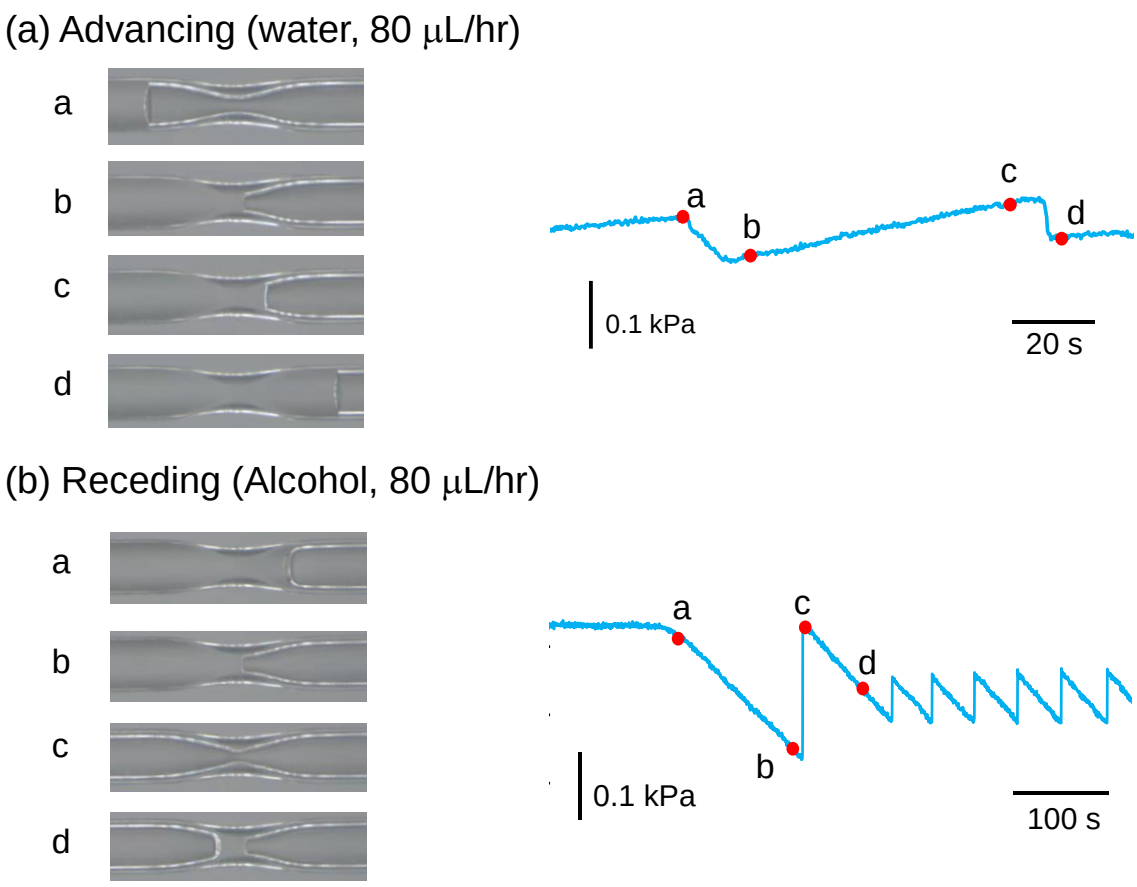

Figure 3.3. Characteristic pressure signature P-t and selected snapshots. Case: (a) water during an advancing test at a flow rate of 80 μL/hr; (b) ethanol during a receding test at a flow rate of 80 μL/hr.

Figure 3.4 shows a collection of pressure signatures measured for deionized water, SDS solutions, and ethanol. Since the effect of flow rate is negligible (within the tested range), most pressure signatures are shown at q=80 μL/hr. The advancing pressure signature changes gradually from water-like to ethanol-like as the surfactant concentration increases. The peak pressure in receding curves also decreases as the surfactant

concentration increases. Snap-offs are observed in ethanol and SDS solutions with surfactant concentration > 2.5 mg/g.

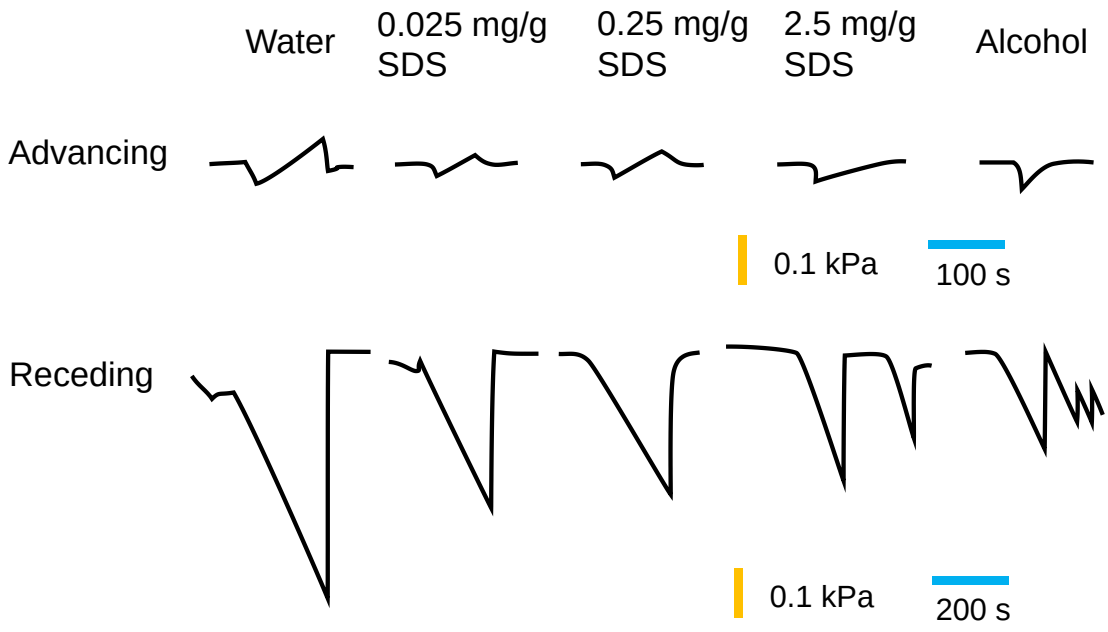

Figure 3.4. Pressure-time P-t signatures recorded as the liquid-gas interface traverses the pore constriction. These pressure-time signatures were obtained with deionized water, SDS solutions and alcohol during advancing A and receding R tests. Signatures are shown for a flow rate of 80 μL/hr.

All test results reported here and complementary static-dynamic tests indicate that the contact angle in advancing θ_{ad} and receding tests θ_{rec} bound the static contact angle θ_{st}, in other words $\theta_{ad} > \theta_{st} > \theta_{rec}$. Advancing and receding contact angles measured in the capillary tube away from the necking are summarized in Table 3.1; contact angles are similar $\theta_{ad} \sim \theta_{rec}$ when the surfactant concentration approaches and exceeds the critical micelle concentration CMC.

3.4 Analyses and Discussion

We measured simultaneously the fluid pressure and interface configurations as an interface passes through a pore throat. Water, ethanol, and SDS solutions were tested. Measured pressure signatures and recorded interface configurations provide rich information about effects of pore geometry and surfactants-pore geometry interactions on two-phase displacement.

3.4.1 Capillary Pressure in Converging-diverging pores

The geometry of the pore affects the generation of capillary pressure [Purcell, 1950; Mason and Morrow, 1991; Urso et al., 1999]. Let's adopt a pore geometry defined by a double cosine function inspired in the experimentally tested tubes (photograph in Figure 3.2). Constant curvature interfaces along this pore constriction are sketched for various contact angles in Figure 3.5. Notice the concave-to-convex transitions for intermediate contact angles.

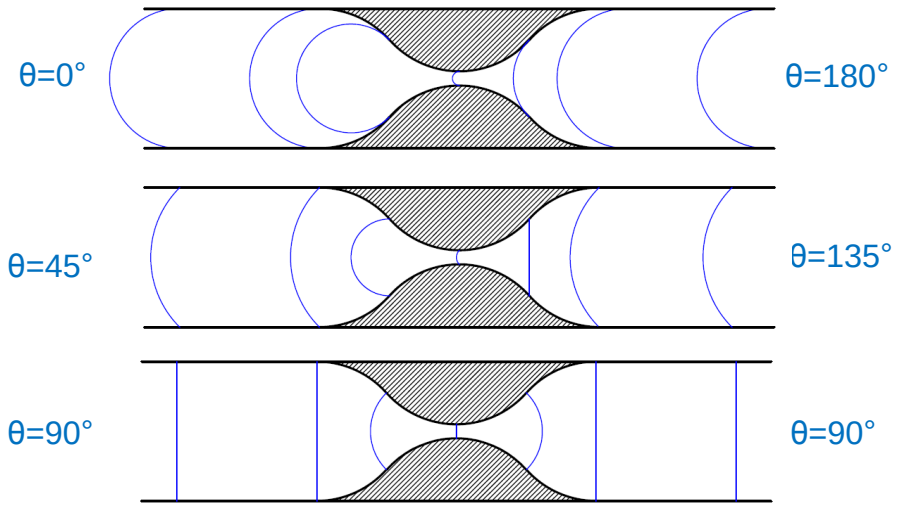

Figure 3.5. Constant curvature interfaces along a capillary tube with a pore constriction.

The local angle α_x between the tube surface at position-x and the flow direction is introduced into the equilibrium equation (refer to Figure 3.1 (d)) to obtain the modified Laplace equation for the capillary pressure at position-x:

$$P_{c,x} = \frac{2\gamma_{gl}\cos(\theta - \alpha_x)}{r_x} \tag{3.1}$$

This equation predicts that the air-liquid interface changes from concave to convex when the argument (θ-α_x)>90. The pressure vs. position P-x signatures computed using Eq. 3.1 are plotted in Figure 3.6 for the same geometry analyzed in Figure 3.5. When fluids are perfectly wetting θ=0, signatures remain alike and the capillary pressure scales linearly with surface tension (Figure 3.6 (a)). In contrast, there are marked changes in P-x signatures with contact angle, as shown in Figure 3.6 (b) for the case of an air-water system (γ_{gl}=72mN/m): the capillary pressure changes from negative-to-positive across the pore throat when the contact angle $\theta \rightarrow 90^o$. The position of pressure maxima depends on the pore geometry α_x and contact angle θ: the maximum pressure develops at the pore throat when $\theta=0^o$ only. Notice that capillary resistance can develop at a pore constriction even when fluids are considered "wetting".

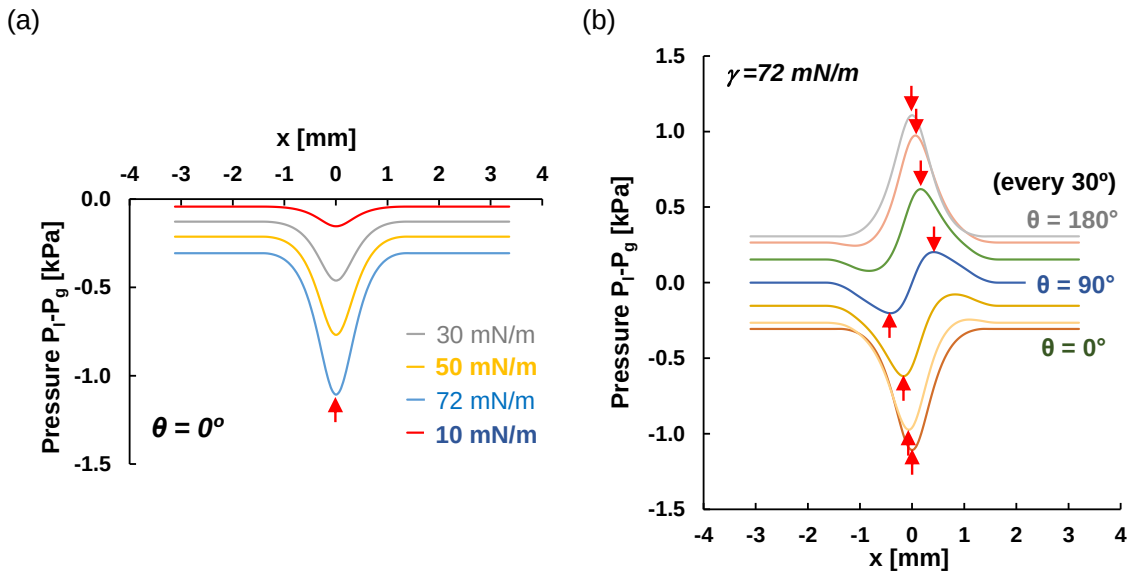

Figure 3.6. Analytically computed liquid pressure-vs.-position P-x signatures as a function of (a) surface tension γ_g and (b) contact angle θ. The assumed constriction geometry is a double cosine function. Capillary pressure maxima (shown with red arrows) take place at the pore throat when θ=0º only.

3.4.2 Theoretical vs. Experimental Signatures—Instabilities

Trends in measured pressure-time P-t signatures exhibit patterns similar to the analytical P-x signatures when the contact angle $\theta \rightarrow 90º$ during advancing tests and is $\theta \rightarrow 0º$ during receding tests (Figures 3.4 and 3.6). Such a marked change in contact angle is in agreement with the much larger capillary maxima observed in receding tests compared to advancing tests (all fluids and flow rates – Measured values in Table 3.1).

In contrast to analytical signals, measured signatures reveal sudden pressure changes that last less than the 250ms sampling interval (Figure 3.4 – Note: the transit time across the pore constriction lasts up to 20 min). Sudden changes in advancing and receding tests include (Figure 3.7):

- Advancing tests: Acceleration before the pore throat. The wetting interface accelerates towards the pore throat driven by increasing capillarity in the narrowing pore ($\theta \rightarrow 90^{o}$, i.e., positive feedback with the pore geometry). The maximum capillary pressure mobilized at the pore throat depends on the system stiffness.
- Advancing tests: Jumps after the pore throat. The advancing fluid $\theta \rightarrow 90^{o}$ must be pushed against the capillary resistance until the peak is reached, and then the front accelerates ahead. This "stick-slip" response appears as positive peaks in experimental P-t signatures (Figure 3.4) and corresponds to positive humps in analytical P-x signals (Figure 3.6).
- Receding tests: Jumps at the pore throat. The contact angle tends to $\theta \rightarrow 0^{o}$ and the peak suction is reached at the pore throat; once again, a "stick-slip" instability follows as the resistance decreases beyond the pore throat.

Jumps in advancing and receding tests are analogous to stick-slip behavior in post-peak-softening frictional systems when a soft spring pulls the mass. Similarly, the acceleration towards the pore throat observed in advancing tests is also possible when the capillary-driven fluid mass is restrained by a "soft spring". We conclude that accelerations and jumps take place in all porous media filled with mixed fluids because interfaces can readily adjust at the multiple pore throats that confine a globule; in other words, a jump or acceleration near a pore throat takes place at the expense of fluctuations at all other interfaces.

Stiffness-dependent capillary pressure generation during accelerating wetting fronts and jumps lead to P-t signatures that deviate considerably from theoretically predicted signals. However, measured pressure P-values that are unaffected by these instabilities plot over the analytical pressure-position P-x signatures (Figure 3.8 - middle

row) when the corresponding x-position for each data point is obtained from the concurrent video recording. A further investigation on mechanisms of these instabilities will be presented in Chapter 4.

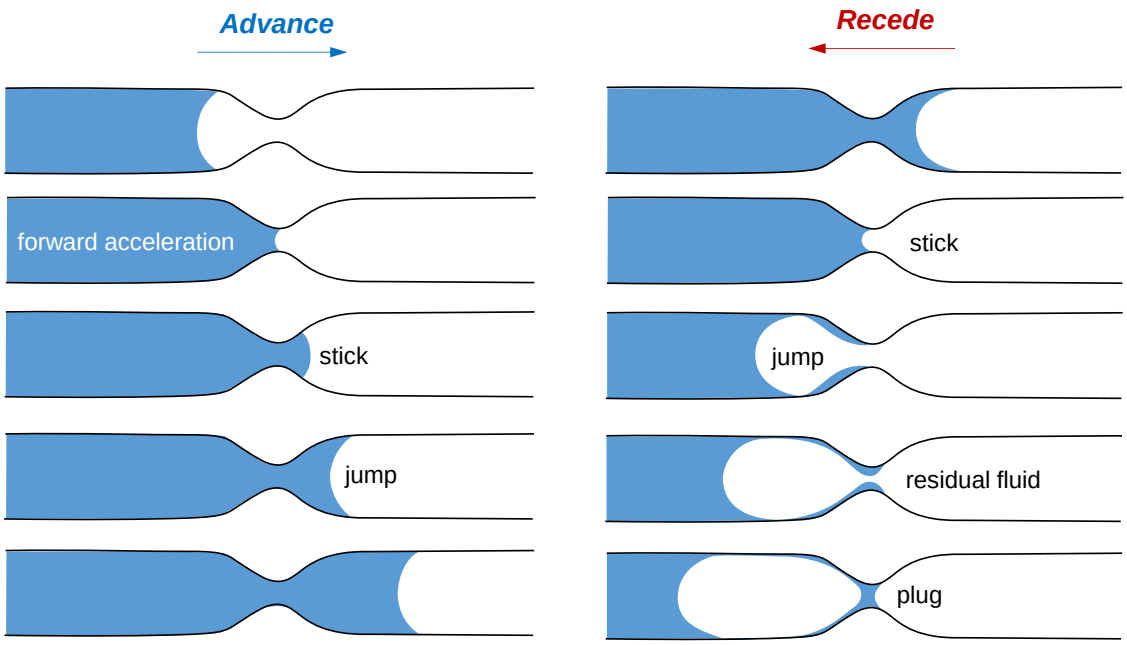

Figure 3.7. Capillary instabilities during the advancing and receding of wetting fronts across a pore constriction. Liquid plugs often reform during receding tests.

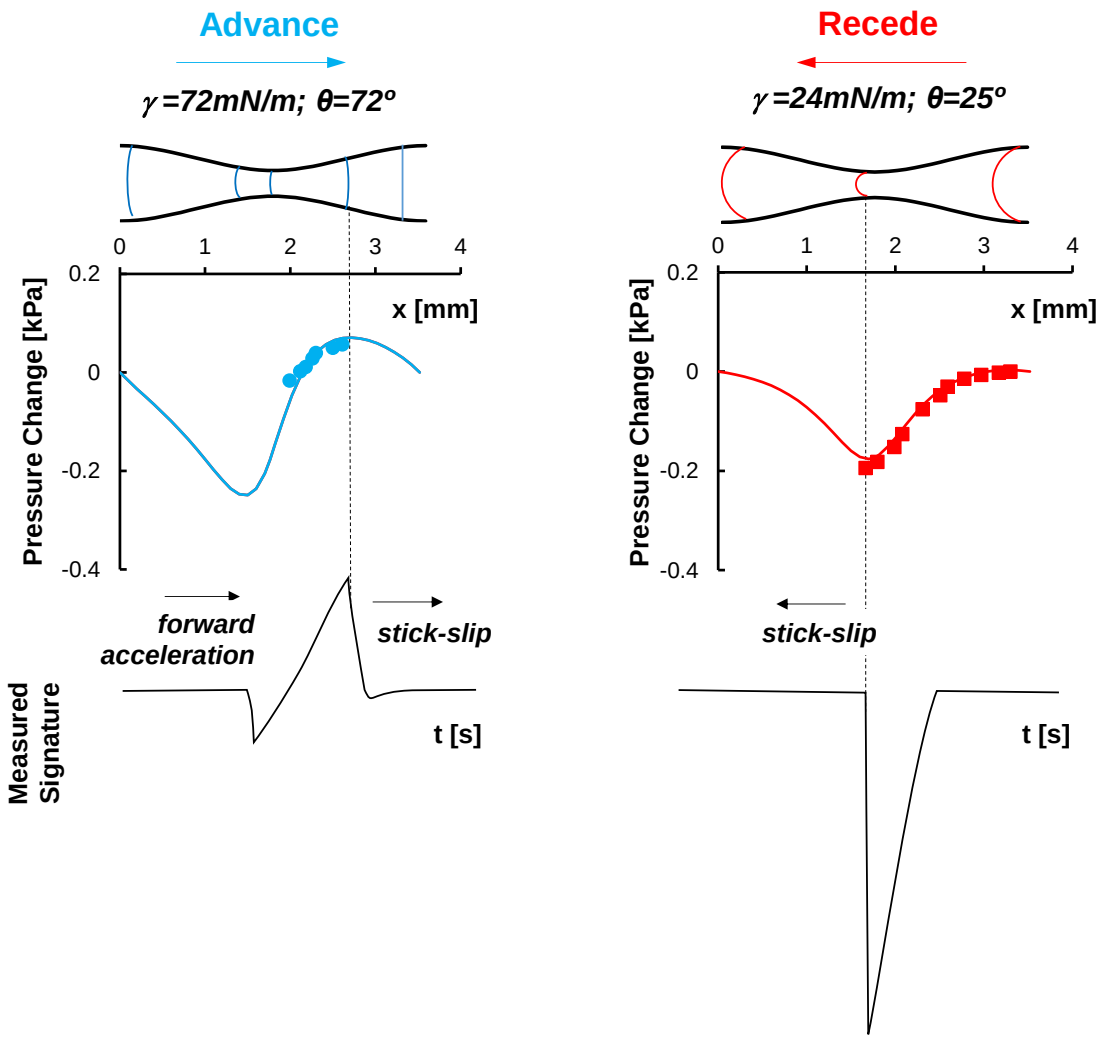

Figure 3.8. Predicted vs. measured pressure signatures during advancing and receding wetting fronts across a pore constriction. Middle row: theoretical pressure-position P-x signatures; the x-position of data points shown on these plots is obtained from the concurrent video recordings. Lower row: measured pressure-time P-t signatures. Note: P-x and P-t signatures are aligned at the stick-slip instability. Left: advancing water (80μL/hr). Right: receding alcohol (80μL/hr).

3.4.3 The Effect of Surfactants on Capillary Pressure across Pore Throats

Let's select pressures P_a and P_b shown for advancing and receding tests in Figure 3.9 to avoid instability-controlled biases on measured pressures. The pressure difference $\delta P=P_a-P_b$ is the change in capillary pressure to cross the pore throat. Figure 3.9 summarizes

δP data in advancing and receding tests for all flow rates. The continuous lines are computed using the constriction geometry, together with contact angle and surface tension values listed in Table 3.2.

The marked differences in capillary pressure difference δP between values in the upper and lower plots are primarily due to differences in contact angle during advancing ($\theta \rightarrow 90°$: maximum capillary resistance past the pore throat) and receding ($\theta \rightarrow 0°$: maximum suction at the pore throat).

On the other hand, the magnitude of $\delta P = P_a - P_b$ varies with surfactant concentration in both advancing (upper plot) and receding wetting fronts (lower plot). In both cases, the measured changes in capillary pressure across the constriction δP are lower than the analytically computed values for solutions with surfactant concentrations in the range of ~0.01mg/g-to-2.4mg/g, where the upper bound is the critical micelle concentration CMC. We anticipate transient surfactant accumulation at the interface, similar to the mechanism captured in Figure 3.1. Differences above the CMC during receding tests may be associated to dynamic stiffening of the receding interface in the presence of surfactants [Ghadiali and Gaver, 2000 and 2008].

Overall, data in Figure 3.9 hint to delayed molecular responses and dynamic interactions that alter surfactant packing at the interface, adsorption-desorption, and non-equilibrium critical micelle CMC concentration [Huang et al., 1989; Schulz and Warr, 2002; Zhang and Somasundaran, 2006; Ghumare, 2012].

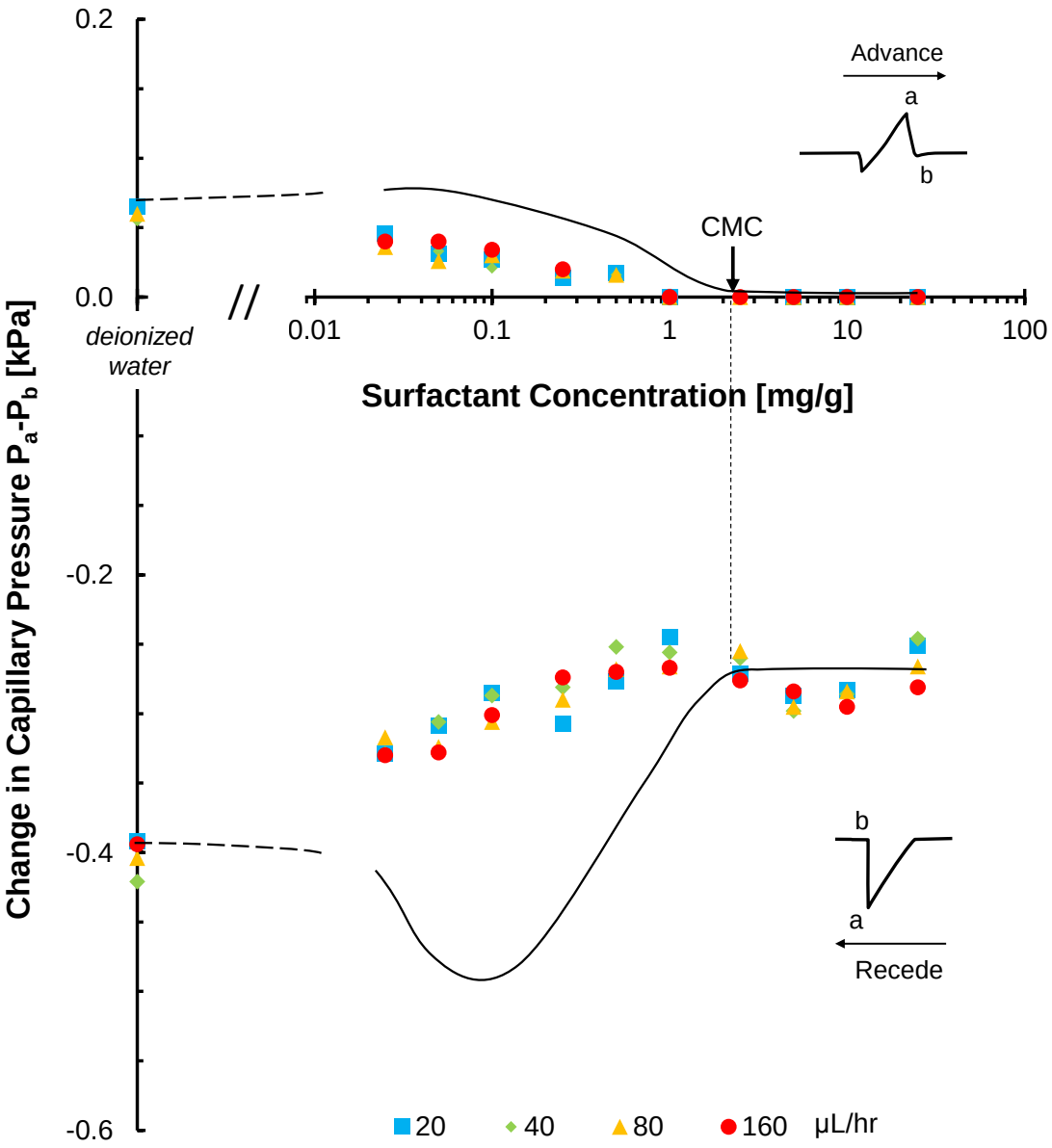

Figure 3.9. Measured changes in capillary pressure δP_c at the pore constriction during advancing and receding tests with SDS solutions. Selected a-and-b pressures avoid biases discussed in the text. Values of δP for deionized water appear on the Y-axis. The continuous lines are computed using the constriction geometry, the contact angle measured for each solution in the capillary tube before the necking, and surface tension values listed in Table 3.1.

3.4.4 Recurrent Plug Formation

Snap-offs and subsequent plug formation has been reported as choke-off instabilities (Mohanty et al., 1987), analyzed in relation to film flow (Lowry and Miller, 1995), and relates to film rapture and residual water left behind (observed by Hsu and Hilpert, 2016). Our results show that wetting liquids tend to form plugs at pore constrictions during receding tests immediately after the stick-slip jump (Figure 3.3): the sudden increase in interface velocity during Haines jumps causes the rupture of wetting films, surface tension forces the residual wetting liquid to migrate towards the pore-throat where it contracts to form the plug (sketched in Figure 3.7).

Plug formation is preferentially observed in fluids with low surface tension (e.g., solutions with surfactant near the CMC, and alcohol – Figure 3.4). Complementary tests - not shown here- confirm the formation of plugs in water-wet capillaries during the invasion of oil, and the increased tendency to plug reformation in narrower pore constrictions. Successive pressure spikes in Figure 3.4 show that these plugs can break and reform multiple times.

Plugs split the non-wetting fluid into isolated globules and add resistance against fluid flow. Consequently, plugs hinder the extraction on non-wetting fluids from the subsurface, for example during remediation efforts or resource recovery.

3.5 Conclusions

Capillarity controls the distribution and transport of immiscible fluids in soils and fractured rocks, thus, it plays a central role in the evolution of subsurface contamination and remediation, resource recovery and carbon geological storage.

The measurement of capillary pressure across a pore constriction with concurrent video recording is an information-rich test. The capillary pressure is a function of contact angle, surface tension and the evolving pore geometry as the fluid interface traverses the pore constriction in advancing and receding tests.

Four distinct instabilities were observed in these experiments: forward acceleration driven by positive feedback from the narrowing pore geometry, stick-slip jump during advancing and receding tests, and snap-offs followed by plug formation in receding wetting fronts. These pore scale phenomena alter the measured pressure-time signatures.

Contact angle and instabilities are responsible for pronounced differences between pressure signatures recorded during advancing and receding tests, and underlie hysteretic saturation in porous media.

Menisci at pore throats confine fluid globules within porous media. These interfaces can readily adjust, therefore, instabilities at a pore throat take place at the expense of fluctuations at all other bounding interfaces.

For a given transport direction, the amplitude of pressure signatures scales with interfacial tension. However, an interface traversing a pore constriction experiences transient non-equilibrium conditions when aqueous surfactant solutions are involved. The

measured capillary pressures cannot be readily anticipated from static-bulk fluid measurements as the transient surface tension can be significantly lower than in static tests. There is some evidence of interface stiffening in high surfactant concentration solutions during receding fronts.

Plugs form when residual annular wetting films/droplets left behind after a jump contract back towards the pore throat. Plug formation is more common when the surface tension is low and pore throats are narrow. Liquid plugs can break and reform multiple times as flow continues. Plugs split the non-wetting fluid into isolated globules and add resistance against fluid flow.

CHAPTER 4. HAINES JUMPS: PORE-SCALE MECHANISMS

4.1 Introduction

Capillary phenomena define the characteristics of multiphase flow in porous media. One particularly interesting and relevant set of phenomena is known as Haines jumps. These instabilities, first reported by Haines (1930), describe sudden jumps of fluid menisci accompanied by fluid redistribution and a transient pressure drop during immiscible displacement such as drying in porous media. For example, consider air-driven displacement of the water phase in a saturated porous medium (Figure 4.1 (a)-1). The curvature of menisci increases as menisci move into pore constrictions (Figure 4.1 (a)-2). Capillary pressure increases according to the Young-Laplace equation:

$$P_n - P_w = \gamma J = \gamma \left(\frac{1}{r_1} + \frac{1}{r_2} \right) \tag{2.4}$$

where γ is the surface/interfacial tension, and J is the curvature of menisci defined by the principal radii: $J=1/r_1+1/r_2$. One meniscus then passes an "unstable point" as the pore constriction widens and abruptly expands into the pore space beyond (Figure 4.1 (a)-3). This occurs with a sudden drop in capillary pressure (Figure 4.1 (b)). This pore-scale phenomenon can result in different displacement patterns in porous media [Holtzman and Segre, 2015; Zhao et al., 2016; Singh et al., 2017] and hysteretic saturation behavior at the macro scale [Schluter et al., 2016].

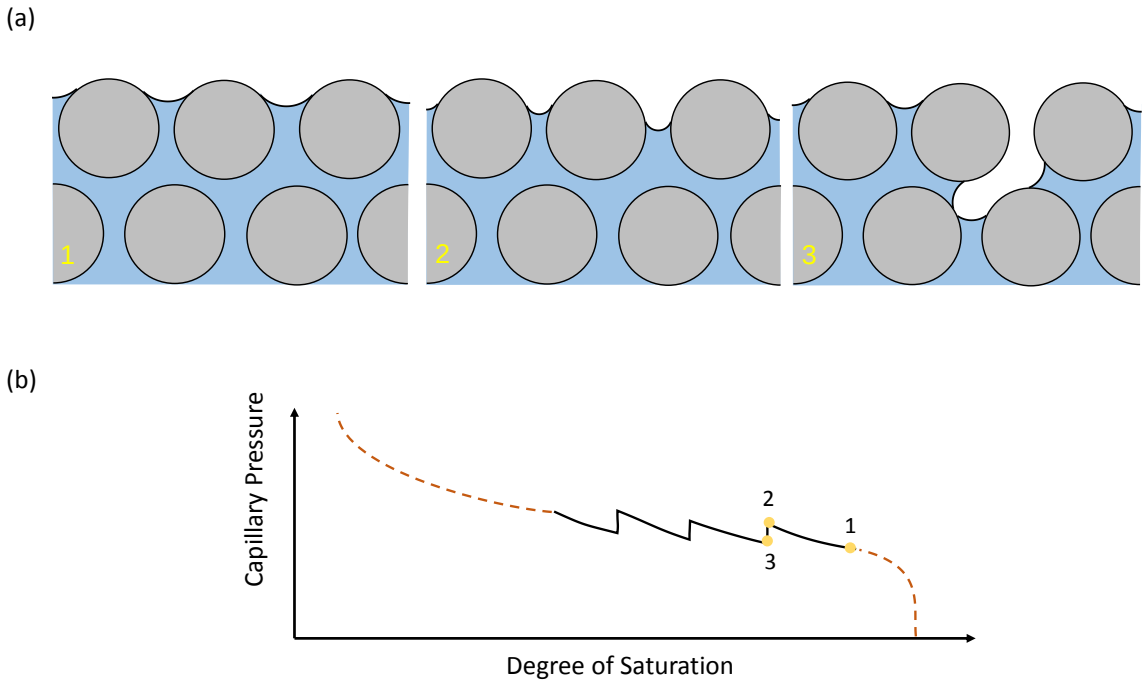

Figure 4.1. Haines jumps during drying in porous media and a detailed schematic of the capillary pressure-saturation curve (after Haines 1930).

Although the phenomenon was discovered nearly 90 years ago, the mechanism of this instability is still not well understood. Early studies used descriptive language such as "unstable point" and "unstable interface" without a specified criterion [Haines, 1930; Morrow, 1970]. A widely adopted criterion was proposed by Melrose (1970, 1974), which suggested that the configuration is stable when:

$$\frac{dJ}{dV_w} < 0 \tag{4.1}$$

where V_w is the volume of the wetting phase (Figure 4.2(a)) [Giordano and Slattery, 1982; Payatakes, 1982; Mohanty et al., 1987]. However, this criterion contradicts with experimental observations of liquid penetration into periodically constricted capillaries [Sharma and Rose, 1991; Liou et al., 2009] and experiments with carefully volume-

controlled displacement [Jang et al., 2016]. Furthermore, recent studies suggest that the Haines jump at a single meniscus affects capillary conditions at all nearby menisci [Armstrong and Berg, 2013; Moebius and Or, 2012].

This chapter documents a detailed analytical and experimental study of Haines jumps in porous media and the effect of interacting menisci. We propose three mechanisms of Haines jumps which can occur in the laboratory or natural conditions. Proposed mechanisms are tested by measuring and analyzing pressure signatures and interface movements during displacement in capillary pore models with specially designed microfluidic chips. The approach used in this study allows the evaluation of relevant parameters involved in Haines jumps. Results hint to the manipulation of this instability.

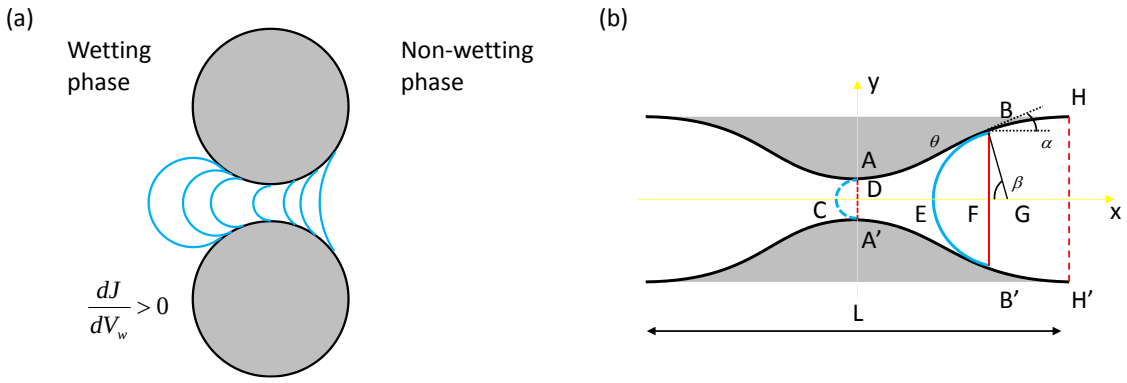

Figure 4.2. Haines jumps in (a) a toroid ring pore (after Melrose 1974) and (b) a sinusoidal pore model.

4.2 Theoretical Framework

Let us consider the displacement of a wetting fluid (e.g. water) by a non-wetting fluid (e.g. air) in a sinusoidal pore model as shown in Figure 4.2 (b). The displacement could be

quasi-static by infinitesimal removal of the wetting phase. This analysis does not consider effects of viscosity and gravity as both the capillary number and Bond number are small.

The pore model shown in Figure 4.2 (b) is not isolated in the system. We hypothesize that a Haines jump is a consequence of system interactions. The pore fluid may be connected with entrapped gas bubbles (Figure 4.3 (a)), fluid in plastic tubings in the lab (Figure 4.4 (a)), and fluid in other connected pores (Figure 4.5 (a)). The continuous wetting phase tends to maintain a constant pressure, especially when the viscosity and gravity are negligible. Therefore, if we infinitesimally remove the wetting phase from the pore model, we expect a pressure change that follows the curvature of the meniscus. As a result, the other part of the system adjusts to this pressure change by redistributing fluid to the pore until a stable interfacial configuration is reached.

The approach used in this study computes the pressure-volume relationship for the pore model and other parts of the system. Characteristics of these curves enable us to identify instabilities. Let's define the pore geometry first and follow with a detailed analyses of different mechanisms.

4.2.1 Geometry of the Sinusoidal Pore Model

The sinusoidal pore model has a length of L, an opening diameter HH' = $2r_1$, and a constriction diameter AA' = $2r_2$. In the coordinate system defined in Figure 4.2 (b), the upper and lower boundaries of the pore model can be expressed as:

$$y_1 = \frac{r_1 + r_2}{2} - \frac{r_1 - r_2}{2}\cos\left(2\pi\frac{x}{L}\right) \tag{4.2}$$

$$y_2 = -\frac{r_1 + r_2}{2} + \frac{r_1 - r_2}{2}\cos\left(2\pi\frac{x}{L}\right) \tag{4.3}$$

The diameter BB' at any position x can be calculated:

$$d(x) = y_1 - y_2 = (r_1 + r_2) - (r_1 - r_2)\cos\left(2\pi\frac{x}{L}\right) \tag{4.4}$$

To compute the pressure-volume relationship, it is convenient to define a reference state where the volume of the wetting fluid V_T is zero. This state is set when the meniscus is at ACA' (i.e. the centre of the constriction). The volume of the wetting fluid can be computed:

$$V_T(x) = V_{ABB'A'} - V_{BEB'} + V_{ACA'} \tag{4.5}$$

The capillary pressure can be computed once we obtain the radius $R(x)$ = BG of the curvature:

$$R(x) = \frac{d(x)}{2}\sqrt{1 + \tan^2(\theta + \alpha)} \tag{4.6}$$

If we assume the pressure in the non-wetting phase is constant, then the pressure in the wetting fluid relative to the pressure in the non-wetting phase is:

$$P(x) = P_w - P_n = -\frac{2\gamma}{R(x)} \tag{4.7}$$

4.2.2 Mechanism 1: Entrapped Gas Bubble

Entrapped gas bubbles inside the porous media or the injection system can interact with fluids in the pore model by expanding or shrinking in response to the pressure change (Figure 4.3 (a)). Assume the volume of the gas bubble is V_0 at the reference state (meniscus at ACA' in Figure 4.2 (b)), with an atmospheric pressure of P_0 and wetting fluid pressure of P_r. Any pressure change of the wetting fluid due to movement of the meniscus will cause a volume change of the gas bubble, which can be computed by the ideal gas law:

$$V_e(x) = \left(\frac{P_0 + P_r}{P_0 + P(x)} - 1 \right) V_0 \tag{4.8}$$

The consequence of this volume change is the redistribution of the wetting fluid in the system. Therefore, the amount of fluid needed V_A to add into the system to move the meniscus to a position x is the sum of the volume change inside the pore model and the volume change in the gas cavity:

$$V_A = V_T - V_e \tag{4.9}$$

There is a qualitative change in the properties of the V_A-P relationship with the increase in the volume of the entrapped gas bubble. Figure 4.3 (b) shows an example which demonstrates the effect of entrapped gas bubbles. The example computes the volume-pressure response when a wetting fluid (e.g. water) is displaced by a non-wetting fluid (e.g. air) in a pore model with L=4 mm, r_1=0.5 mm, and r_2=0.2 mm. The solid and dashed lines represent V_A-P and V_e-P relationships, respectively. For the case where the volume of the gas bubble is zero, V_e is zero for all P. Therefore $P(V_T)$ and $P(V_A)$ collapse into one curve.

The pressure in the wetting fluid firstly decreases as the meniscus moves towards the constriction. It reaches a minimum at the reference state (in case of θ=0°). Then it increases as the meniscus moves away from the constriction. There is a one to one correspondence between V_A and P.

However, V_e increases as the volume of the gas bubble increases. As a result, $P(V_A)$ distorts from $P(V_T)$, with the reference state anchors. Although the $P(V_A)$ curve for V_{gas}=0.05 mL is still injective, the $P(V_A)$ curve for V_{gas}=0.1 mL becomes multivalued, i.e. a V_A can be associated with multiple P (Figure 4.3 (b)). Since V_A decreases monotonously, it is impossible that the pressure changes continuously. By contrast, it jumps to a higher pressure. The position of the meniscus also jumps simultaneously to a new equilibrium position. This equilibrium position can be computed from the pressure value. Note that this mechanism has been proposed to explain drop formation instabilities [Liggieri et al., 1990].

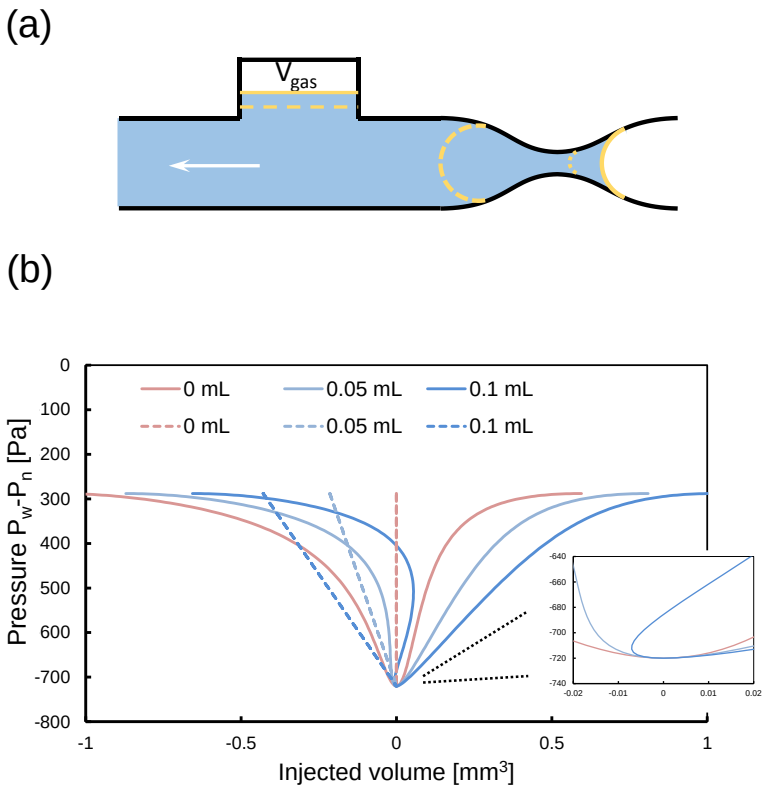

Figure 4.3. Mechanism 1: entrapped gas bubble. (a) A schematic diagram. (b) Pressure-volume curves. Case parameters: surface tension γ=0.072 N/m, contact angle θ=0°, atmospheric pressure P_0=101 kPa, capillary opening radius r_1=0.5 mm, pore constriction radius r_2=0.2 mm, pore constriction length L=4 mm.

4.2.3 Mechanism 2: Deformable Solid Matrix

The interaction between the fluid and the injection system (mainly the tubing in this case) also results in quantum jumps of the meniscus when it passes through a pore constriction due to the elasticity of the tubing. In laboratory experiments, micromodels are usually connected to pumps, flow meters, pressure sensors, and other flow components by tubings. Assume the tube has a length of L_{tube}, an inner diameter a, and outer diameter b. Mechanical properties of the tube are the Young's modulus E, Poisson ratio ν, and shear

modulus G. The radial displacement at $r=a$ caused by a change in fluid pressure P can be calculated based on the cavity expansion solution [Yu, 2013]:

$$u = \frac{P}{2G\left(\frac{1}{a^2} - \frac{1}{b^2}\right)}\left(\frac{1-2\nu}{b^2}a + \frac{1}{a}\right) \tag{4.10}$$

Thus the change in the volume of the tube is:

$$V_{tube} = 2\pi a \cdot u \cdot L_{tube} \tag{4.11}$$

We assume the volume change of the tube at the reference state is V_0, with fluid pressure P_r and obtain:

$$V_e = V_0 - V_{tube} \tag{4.12}$$

Finally we can calculate the V_A-P relationship by following the same procedure outlined in section 4.2.2.

We observe a result similar to the case of the entrapped gas bubble. There is a quantum change with the increase in tubing elasticity. Most plastic tubing materials used in the laboratory have a Young's modulus which ranges from 2 MPa to 200 MPa, and a Poisson ratio of around 0.45 (see Table 4.1). Figure 4.4 (b) shows the volume-pressure relationships for the same pore model connected with a 20cm tube. When the meniscus moves towards the pore constriction, the pressure decreases and the tube shrinks. After the meniscus reaches the reference point and starts to move away from the pore constriction, the pressure increases and the tube expands. V_e increases with increasing tubing elasticity and distortions of the $P(V_A)$ curve. Again, the enlarged figure around the reference point

clearly shows that the $P(V_A)$ curve for E=2.5 MPa becomes multi-valued. Therefore we can anticipate a jump in the pressure curve as well as the meniscus position since V_A can only decrease monotonously.

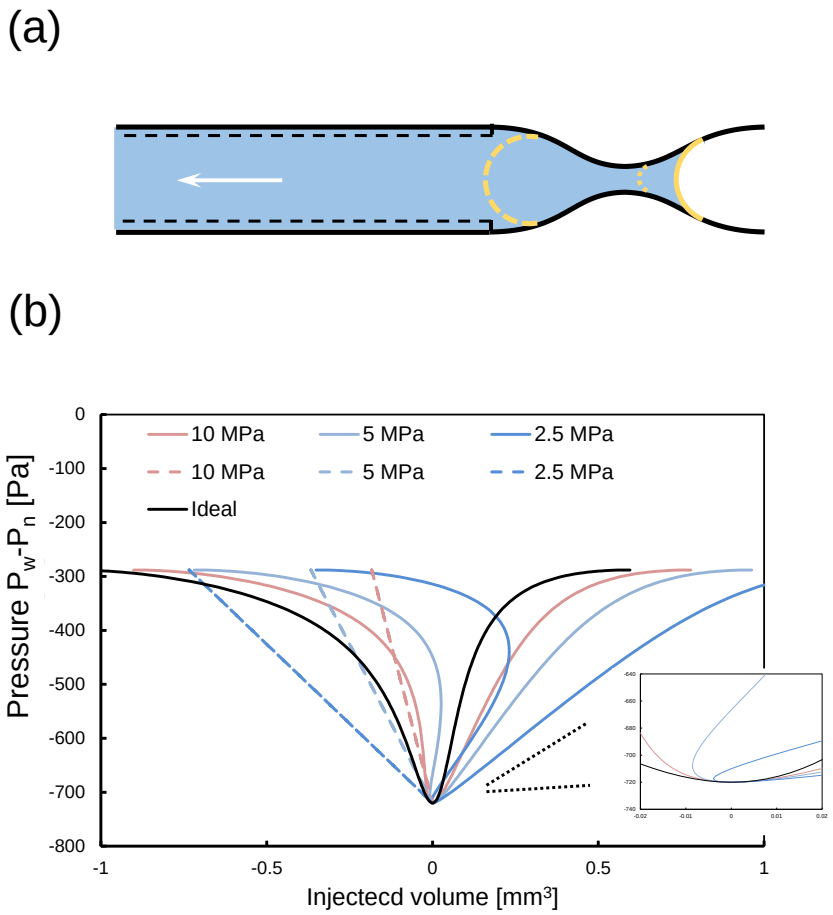

Figure 4.4. Mechanism 2: deformable solid matrix. (a) A schematic diagram. (b) The pressure-volume curves. Case parameters: surface tension γ=0.072 N/m, contact angle θ=0°, tube length L_{tube}=0.2 m, capillary opening radius r_1=0.5 mm, pore constriction radius r_2=0.2 mm pore constriction length L=4mm.

4.2.4 Mechanism 3: Interacting Menisci

While interactions with injection systems may mostly occur in the laboratory, we can analyse multi-pore systems like natural porous media by using a similar approach. As

illustrated in Figure 4.5 (a), the menisci at different pores tend to maintain the same curvature. Once the meniscus reaches the widest pore constriction, it moves further left and its curvature starts to decrease. Meanwhile, the menisci in other pores moves right to maintain the same curvature with the meniscus in the wider pores. For any pore model i, there is a relationship between P and V_T:

$$V_T^i = f^i(P) \text{ , i=a, b, c, } \ldots \tag{4.13}$$

Assume pore a is the widest pore, we can obtain the V_A-P relationship:

$$V_A = V_T - V_e = V_T^a - \left(-V_T^b - V_T^c - \ldots\right) \tag{4.14}$$

Let us consider that the meniscus in pore a is connected with menisci in other n pores. Pore a has a pore constriction r_2=0.2 mm which is slightly larger than other pores (r=0.18 mm). All pores have an opening of r_1=0.5 mm. We expect the V_A-P shifts toward the right with the reference state anchors with increasing numbers of connected pores. Figure 4.5 (b) presents the computed V_A-P relationships. Although P changes monotonously with V_A for n=1 and 2, a jump in pressure and also in the meniscus position occurs for n=3. This indicates that with an increased number of connected pores, more menisci interact with the meniscus in the widest pores, which produce an effect similar to an increase of entrapped bubble volume or system elasticity.

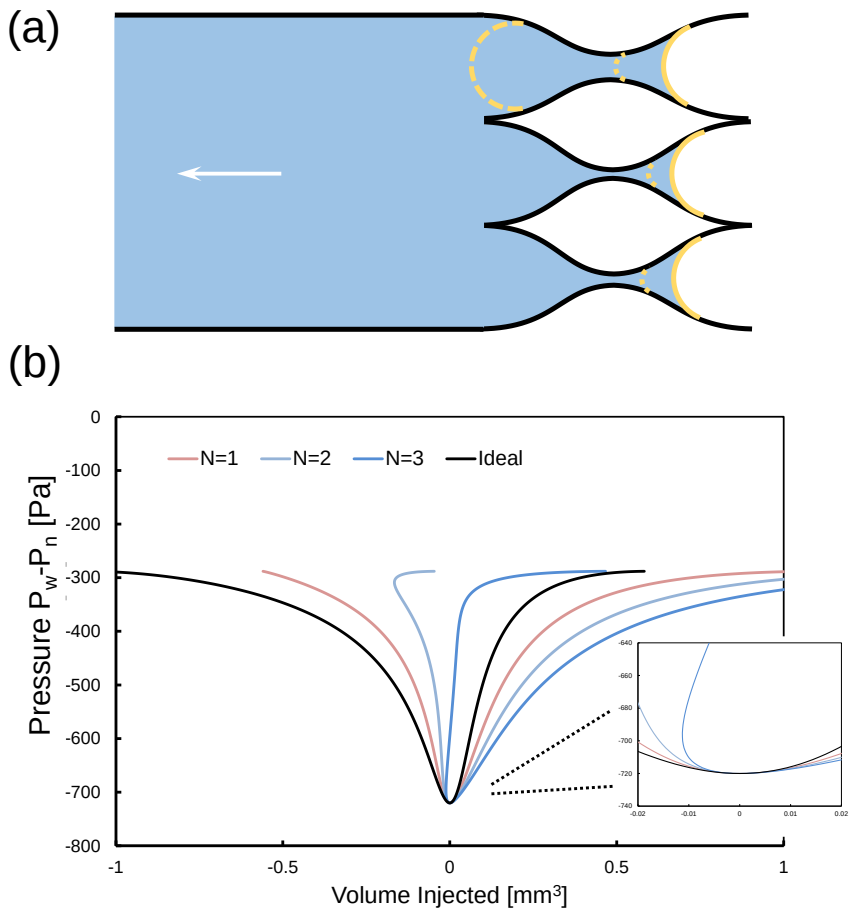

Figure 4.5. Mechanism 3: interacting menisci. (a) A schematic diagram. (b) The pressure-volume curve. Case parameters: surface tension γ=0.072 N/m, contact angle θ=0°, capillary opening radius r_1=0.5 mm, radius of wider pore constriction r_2=0.2 mm, radius of narrower pore constriction r_3=0.18 mm, pore constriction length L=4 mm.

4.3 Experimental Study

To verify the proposed mechanisms, we record the fluid pressure change and evolution of the interface configuration during immiscible displacements in pore models. Pore models are made of either borosilicate glass capillary tubes or PDMS (Polydimethylsiloxane). The observed phenomena are compared with model predictions.

4.3.1 Experimental Setup

The experimental setup is similar to the setup described in Chapter 3. The glass capillary tube with ID=0.97 mm has a constriction to simulate the pore throat (ID=0.32 mm, L=3.6 mm). The microfluidic channel is made of PDMS. The depth of the channel is 0.1 mm. It has three connected pores which all have an opening width W=0.5 mm. One of the pore throats is slightly larger than the other two (i.e. W_a=0.12 mm, W_b=W_c=0.1 mm).

To test the mechanism of entrapped gas bubble, the capillary tube connects to a syringe with a short Polyurethane (PU) tube which minimizes the effect of the elasticity of the injection system. A pressure transducer mounted next to the inlet measures the pressure change.

A soft Tygon tube connects the capillary tube to the syringe to verify the mechanism of deformable solid matrix. Changes of the length of the Tygon tube produce different displacement results.

4.3.2 Results

Entrapped Gas Bubble. Figure 4.6 shows the pressure signature for a receding test (red dots) and an advancing test (blue dots) for the displacement between ethanol and air with q=80 μL/hr. The solid line is the prediction based on the model presented in section 4.2.2. The model accurately predicts the position and amplitude of the jump in both receding and advancing tests. It also explains the differences between receding and advancing tests.

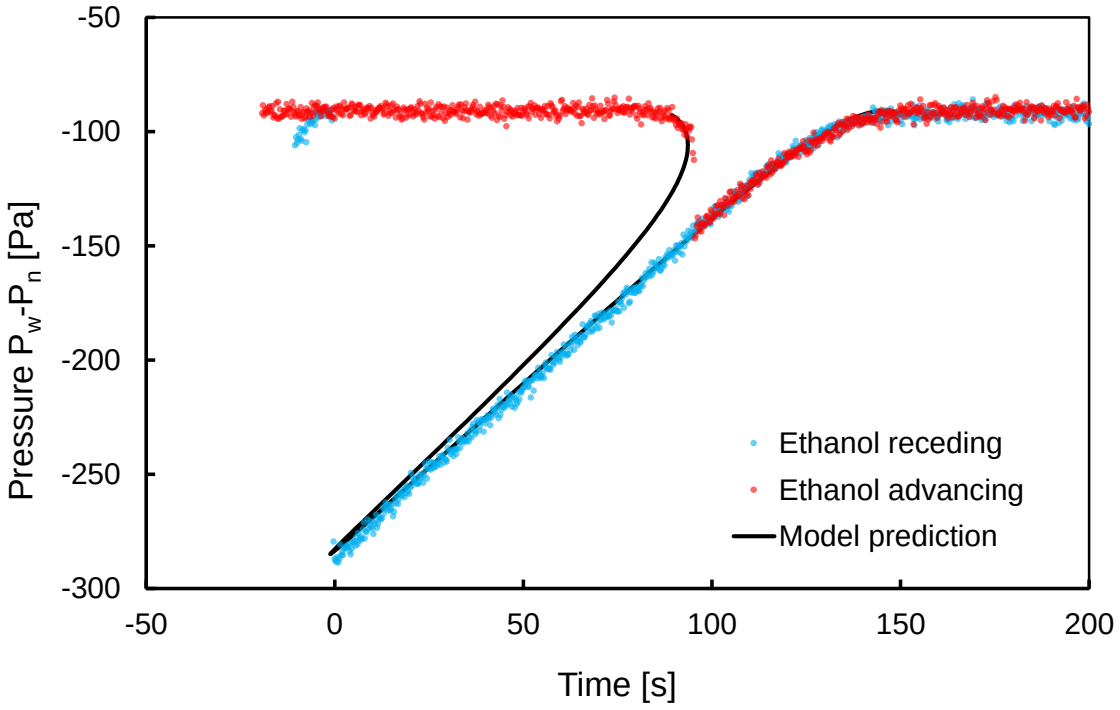

Figure 4.6. Haines jumps caused by interactions between menisci and entrapped gas bubbles. Model parameters: surface tension γ =0.024 N/m (Ethanol-air), contact angle θ=22°, atmospheric pressure P_0=101 kPa, volume of the entrapped gas bubble V_0=1.48 mL, capillary opening radius r_1=0.48 mm, pore constriction radius r_2=0.16 mm, pore constriction length L=3.6 mm.

Stiffness of the injection system. Figure 4.7 shows the position of the meniscus as a function of time in receding tests for the displacement between water and air with q=100 μL/hr. The length of the Tygon tubing is 16 cm and 34.4 cm in the short tube experiment and the long tube experiment, respectively. The model described in 4.2.3 matches the experimental observation.

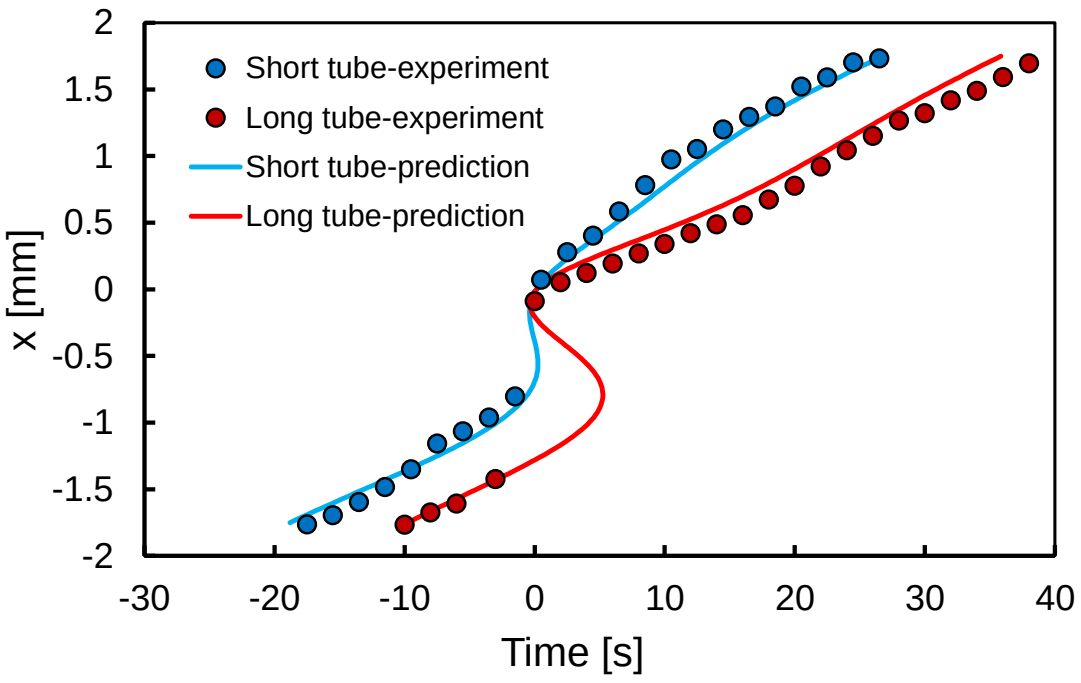

Figure 4.7. Haines jumps caused by interactions between menisci and the plastic tubing. Model parameters: surface tension γ=0.072 N/m (Water-air), contact angle θ=27°, elastic modulus of Tygon tube E=5.8 MPa, short tube length L_{tube}=16.0 cm, long tube length L_{tube}= 34.4 cm. capillary opening radius r_1=0.48 mm, pore constriction radius r_2=0.16 mm, pore constriction length L=3.6 mm.

Interacting Menisci. Figure 4.8 displays the movement of the ethanol-air menisci when they pass through the pore throats in a PDMS microfluidic chip. All menisci move backward at the beginning. Menisci in pores with narrower pore throats stop receding before they reaches the pore throats, while the meniscus in the pore with the largest pore throat keeps receding. A Haines jump occurs in the pore which has the largest pore throat when the meniscus passes the narrowest point. At the same time, the menisci in other pores move forward. The results agree well with the mechanism in section 4.2.4 which describes the behaviour of interacting menisci.

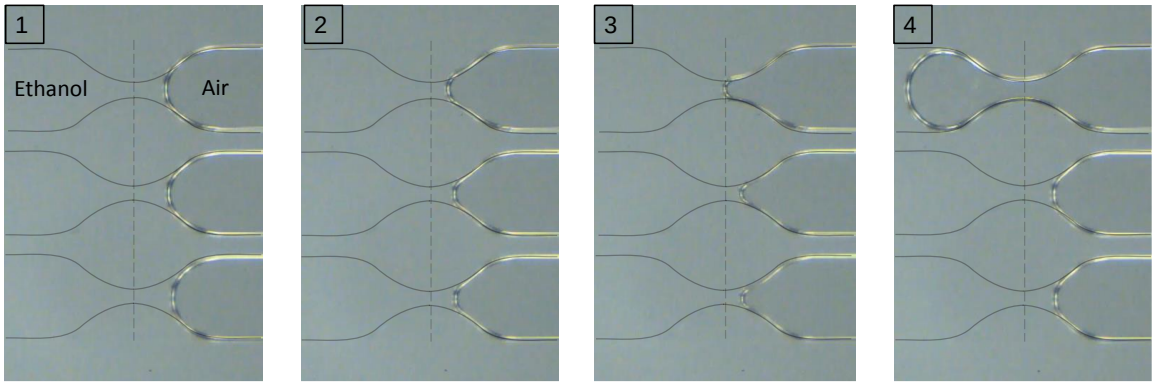

Figure 4.8. Haines jumps caused by interacting menisci.

4.4 Discussion

In previous sections we proposed three mechanisms of Haines jumps based on a system-interaction approach. The mechanisms are tested experimentally in a capillary pore model and also in microfluidics. An advantage of our approach is that it allows us evaluate various factors which can affect the Haines jump. These evaluations and analyses provide guidance for laboratory studies as well as insights into the manipulation of Haines jumps in natural porous media.

4.4.1 Generalization

Figure 4.9 summarizes and generalizes the proposed mechanisms. The pore model has an ideal fluid volume-pressure curve when the fluid is infinitesimally removed from the pore. The remaining parts of the system also has one. The real V_A-P curve for the system is a combination of the V-P curves for the pore model and the remaining system. The combination is fulfilled by fluid redistribution in the pore model and the remaining system to maintain pressure equilibrium. Finally, a Haines jump is a system response to the monotonous change in pore fluid volume.

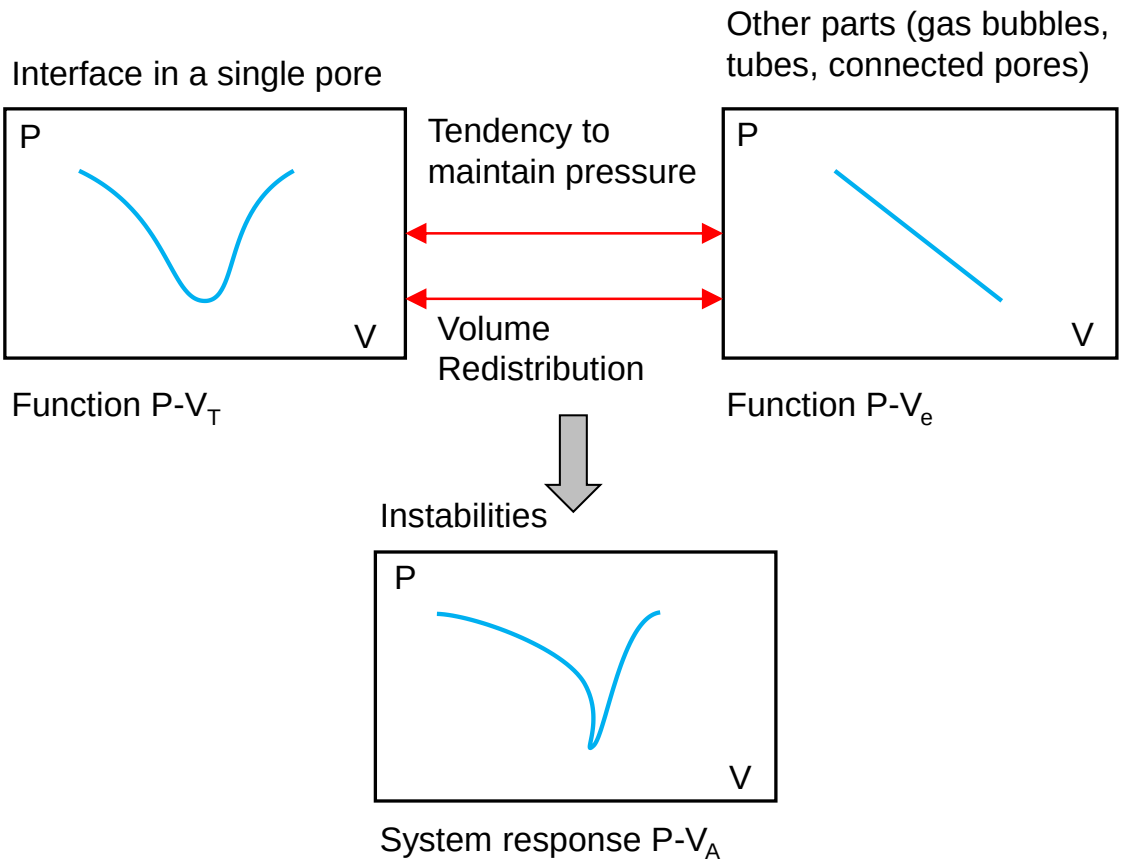

Figure 4.9. The generalization of proposed mechanisms.

4.4.2 Effect of Pore Geometry and Series Pores

When there is an entrapped gas bubble or tubing elasticity, we can infer that the narrower the pore constriction, the larger the volume change of the bubble or the tube as a result of a larger pressure change. A higher tendency of a Haines jump is expected to occur with smaller r_2 to r_1 ratio. This is shown in Figure 4.10 (b), in which the pore model has a fixed r_1=0.5 mm and varied r_2 of 0.1, 0.15, and 0.2 mm. Although Haines jumps happen in narrower pores, the phenomena do not occur in wider pores.

In a series of pores, it is also possible that the meniscus jumps through one pore throat. In the pore model shown in Figure 4.10 (a), the radii of pore constrictions 1, 2, and 3 are 0.1, 0.2, and 0.15 mm, respectively. The radius of the opening is 0.5 mm. Figure 4.10 (c) plots the computed volume-pressure curve for different volumes of the entrapped gas bubble. When V_{gas}=0, the displacement is smooth. At V_{gas}=0.1 mL, the meniscus jumps at pores 1, 2, and 3. However, the meniscus jumps at pore 1, bypasses pore 2, and settles at pore 3 when V_{gas}=0.3 mL. This implies that a jump can drain the fluid in a large pore and break any fluid connections.

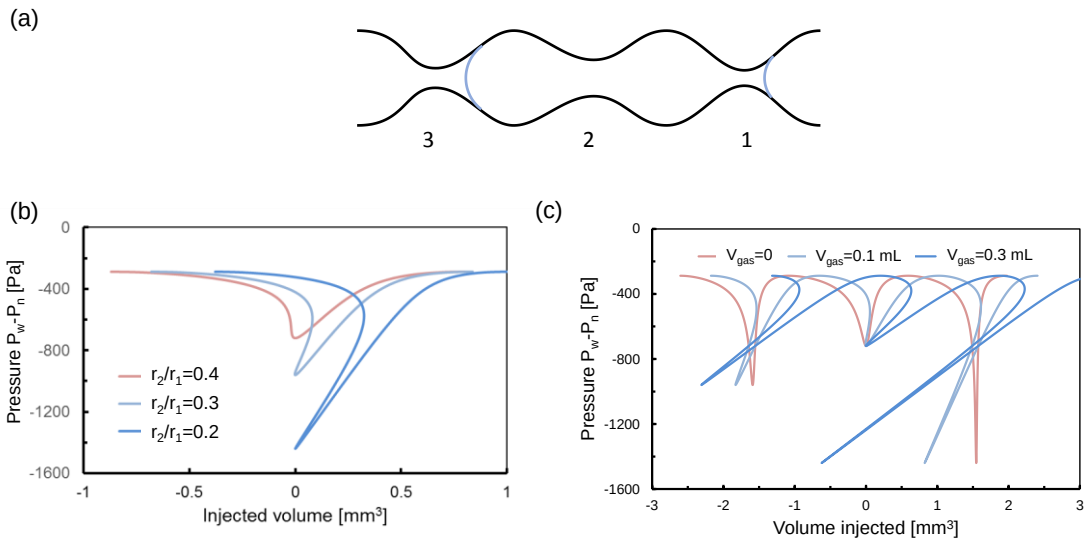

Figure 4.10. The effect of pore geometry on Haines jumps. (a) Pores with different pore throat sizes. (b) Pressure-volume curves for different pore throat size to pore opening ratios. (c) Pressure-volume curves for a series of pores. Case parameters: surface tension γ=0.072 N/m, contact angle θ=0°, atmospheric pressure P_0=101 kPa, capillary opening radius r_1=0.5 mm, radius of pore constriction #1 r_2=0.1 mm, radius of pore constriction #2 r_2=0.2 mm, radius of pore constriction #3 r_2=0.15 mm, pore constriction length L=4 mm.

4.4.3 Effect of Surface Tension and Contact Angle

Surface tension affects the amplitude of the pressure change in pore fluid, thus affecting the response of the entrapped gas bubble or the tubing system. In our experiments, Haines jumps happen when air displaces water ($\gamma_{air\text{-}water}$=0.072 N/m). It does not occur when air displaces alcohol ($\gamma_{air\text{-}alcohol}$=0.024 N/m). A lower surface tension creates smaller changes in pressure, and thus the response of the system is also weaker.

However, the contact angle plays a more profound role, as it affects not only the amplitude of the pressure change, but also the shape of the V_T-P curve [Jang et al., 2016; Masson and Morrow, 1994]. The maximum curvature does not occur at the reference state when the contact angle is not zero. It occurs after the meniscus passes the constriction. In addition, the pressure may have a maximum value before the meniscus reaches the constriction. Figure 4.11 (a) shows the effect of the contact angle on the V_A-P curve. While Haines jumps occur for θ=0°, 30°, and 60°, it does not for θ=90°. Note that the position and the amplitude when the Haines jump occurs also changes with the contact angle. Another interesting result is that we can observe two instabilities in the pore model when the entrapped gas bubble volume is large enough (Figure 4.11 (b)). This is consistent with observations in Jang et al. (2016).

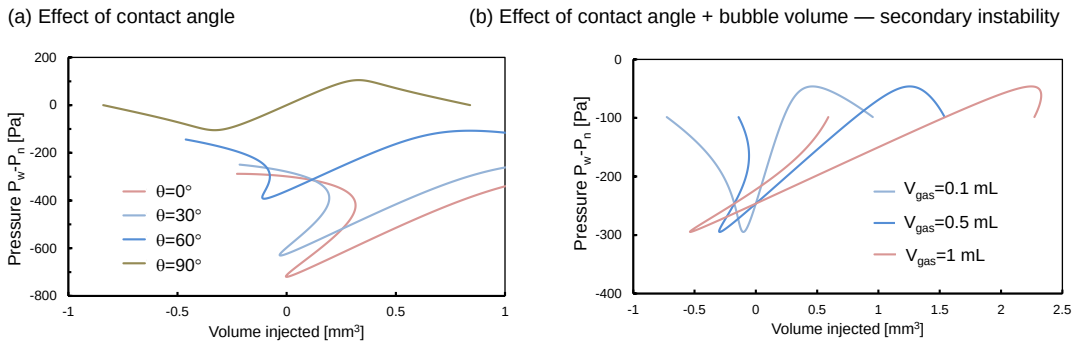

Figure 4.11. The effect of the contact angle on Haines jumps. (a) Pressure-volume curves at different contact angles. (b) Pressure-volume curves with the increase in bubble volume showing the occurrence of the secondary instability. Case parameters: surface tension γ =0.072 N/m, atmospheric pressure P_0=101 kPa, capillary opening radius r_1=0.5 mm, pore constriction radius r_2=0.2 mm, pore constriction length L=4 mm.

4.4.4 Porous Media

The above analyses mainly apply to Haines jumps caused by entrapped gas bubbles or tubing elasticity. Menisci interactions in porous media are governed by interconnected menisci, rather than the size of entrapped gas bubbles or the elasticity of the tubing. However, pore geometry and contact angle still play a crucial role in determining the occurrence of Haines jumps. The pore constriction to the opening ratio, rather than the size of the pore constriction, affects the occurrence of the Haines jump. Surface tension has no effect (Note that our analysis only considers low capillary number conditions).

4.4.5 Manipulation

Haines jumps affect global displacement patterns in porous media. Haines jumps increase the interfacial instability, promote viscous fingering, and hence cause increasing trapping [Holtzman and Segre, 2015; Zhao et al., 2016; Singh et al., 2017]. We may enhance displacement/recovery by controlling the occurrence of Haines jumps. Analyses

in this chapter showed that the pore geometry and contact angle affect Haines jumps in porous media. While we are not able to alter the pore geometry in natural porous media, we can alter the wettability by using surfactants or nanoparticles. Higher displacement efficiency can be achieved with intermediate wetting conditions when Haines jumps are minimized. This has been demonstrated experimentally and numerically in Trojer et al. (2015) and Zhao et al. (2016).

Another potential approach to minimize Haines jumps is to alter the mechanical properties of the interface. Although most fluid-fluid interfaces are governed by the Young-Laplace equation, interfaces coated with particles have a unique solid-like behaviour. In particular, the interface entirely covered by particles becomes a thin elastic shell with zero interfacial tension, while it recovers as a fluid-fluid interface when it spreads out [Sun et al., 2018]. When a particle-coated interface moves towards a pore constriction, the interfacial area decreases and particles compact; when a particle-coated interface moves away from a pore constriction, the interfacial area increases and the interface becomes fluid-like. The changing in mechanical properties of the interface can change the V-P curve of the system, and therefore probably hinders Haines jumps. Additional studies are needed to understand the effect of particle-coated interfaces on multiphase-flow in porous media.

4.4.6 Guide for laboratory study with microfluidics

Laboratory studies with microfluidics should carefully consider the effects of entrapped gas bubbles and tubing elasticity. This is especially relevant when capillary phenomena dominates the microfluidics, because the interaction between the fluid menisci and the gas bubble or the tubing may have a significant consequence on the flow behaviour.

The size of the pore constriction in microfluidics can be as narrow as 10 μm. Therefore, capillary effect can be significant. Moreover, the material of the micro-chip such as PDMS has a low elasticity. It might be necessary to remove all entrapped gas bubbles and even dissolved gases, and to use hard tubing if a smooth displacement is desired. These results conclude that a careful explanation of microfluidic results should consider the interaction between fluid menisci, entrapped gas bubbles, and tubing elasticity.

Table 4.1. Elasticity of commonly used tubing.

Category	Material	Durometer	Elastic Modulus [MPa]
Soft	PVC	50A, 65A,70A	3.3, 5.8, 7.3
	Tygon	40A, 55A, 65A, 75A	2.2, 3.9, 5.8, 9.4
Firm	PVC	85A	17.5
	PE	90A, 45D	27.7, 46.5
	EVA	95A	58.3
Hard	Nylon	50D, 55D	62.5, 84.9
	Teflon	55D, 60D	84.9, 117.2
	PP, PE, and PU	65D	165.8

Note: Durometer data are from mcmaster.com. Young's modulus are computed by following the method in Mix and Giacomin (2011).

4.5 Conclusions

We hypothesized and verified that Haines jumps respond to system interactions in which fluid redistributes to maintain the pressure equilibrium during the displacement. The three interactions identified and tested in the chapter can happen in both laboratory experiments and natural systems: interactions with the entrapped gas bubble, with the deformable solid matrix, and among interconnected menisci. These interactions were theoretically analyzed and experimentally validated using capillary pore models and microfluidic chips.

Our approach enabled us to analyze the various factors that affect Haines jumps, e.g. pore geometry, contact angle, and surface tension. Haines jumps are more likely to occur with smaller pore constrictions, smaller contact angles, higher interfacial tensions when there is entrapped gas bubble or in a deformable solid matrix. The pore connectivity, pore constriction to pore opening ratio, and the contact angle play a defining role in porous media.

Analytical and experimental results provide insights into the manipulation of Haines jumps and guidance for laboratory studies. The system response can be controlled by changing the contact angle or interfacial tension (e.g. with the use of surfactants or nanoparticles). Laboratory studies with capillary pore models and microfluidic chips should be designed, run, and analyzed taking into consideration of interactions of the fluid with entrapped gas bubbles and the solid matrix elasticity.

CHAPTER 5. THE MECHANICAL RESPONSE OF NANOPARTICLE-COATED INTERFACES

This chapter was written together with fellow student Qi Liu (submitted for publication).

5.1 Introduction

The assembly of a monolayer of particles at liquid/liquid or liquid/gas interfaces has attracted great attention in recent years due to its distinctive properties and number of potential applications. These assembled layers have been described as particle rafts [Cicuta and Vella, 2009], granular rafts [Jambon-Puillet, 2016], and particle-laden interfaces [Razavi et al., 2015]. They form particle-coated droplets [Deshmukh et al., 2015], particle-covered bubbles [Abkarian et al., 2007], armored droplets [Sicard and Striolo, 2017], and liquid marbles [Aussillous and Quere, 2001]. The particle-coated interface stabilizes emulsions and foams (Pickering emulsions and foams; see Binks 2002 and Chevalier and Bolzinger 2013), and may enhance oil recovery [Luo et al., 2016] and drug delivery [Frelichowska et al., 2009].

The deformation of the particle-coated interface is intriguing. The particle-coated interface undergoes a transition from liquid-like to shell-like behavior as the particle coverage increases when the size of the interface decreases [Datta et al., 2010]. Further compression leads to a collapse of the interface due to buckling instabilities or particle expulsion [Razavi et al., 2015]. Previous experiments studied the deformation of the particle-coated interface primarily with a Langmuir trough setup and analyzed the surface pressure $\Pi=\gamma_0-\gamma$ curve [Santini et al., 2011; Deak et al., 2007; Horozov et al., 2006]. The

particle-coated interface has been modeled as an elastic sheet [Vella et al., 2004; Pocivavsek et al., 2008; Cicuta et al., 2003]. A few studies also investigated the deformation of bubbles or droplets coated with particles [Asekomhe et al., 2005; Monteux et al., 2007; Datta et al., 2010].

However, it has been suggested that measurements with the Langmuir trough and Wilhelmy plate are distorted, and that the surface pressure is not uniform throughout the trough due to the granular character of the particle-coated interface [Cicuta and Vella, 2009; Pocivavsek et al., 2008; Aumaitre et al., 2011]. Moreover, experimental conditions in the trough differ from most applications where the interface is curved (e.g. small droplets, bubbles, and pore constrictions). Furthermore, elastic models ignore the granular nature of the particle shell and the complexity of particle-interface interactions [Leaby et al., 2010; Dasgupta et al., 2017; Bresme and Oettel, 2007; Jambon-Puillet et al., 2017].

This study uses a different approach to investigate the mechanical properties of silica nanoparticle-coated interfaces. We simultaneously measure fluid pressure responses and morphology changes of a water or oil droplet covered with nanoparticles during droplet shrinkage and expansion. This chapter starts with a review of film formation followed by the experimental study.

5.2 Film Formation

The hydrophobicity of particles determines their affinity to the water-oil interface. Let's consider the interfacial energy change caused by the transfer of a particle from the water phase to the oil-water interface (Figure 5.1 (a)). The total interfacial energy E_A of a solid particle of radius a and contact angle θ is:

$$E_A = \gamma_{ws} \cdot 4\pi a^2 + \gamma_{ow} \cdot \pi a^2 \sin^2 \theta \quad (5.1)$$

The total interfacial energy E_B of a solid particle at the interface with the contact angle θ is:

$$E_B = \gamma_{os} \cdot 2\pi a^2 (1 - \cos\theta) + \gamma_{ws} \cdot 2\pi a^2 (1 + \cos\theta) \quad (5.2)$$

Young's equation relates γ_{ow}, γ_{os}, and γ_{ws} as $\gamma_{ow}\cos\theta = \gamma_{os} - \gamma_{ws}$. Then the free energy change $\Delta E = E_B - E_A$. Finally, we are able to express ΔE_p as follows:

$$\Delta E = -\pi a^2 \gamma_{ow} (1 - \cos\theta)^2 \quad (5.3)$$

Figure 5.1 (b) shows the influences of contact angles on the interfacial energy change. Completely hydrophobic (θ=180°) or hydrophilic (θ=0°) particles are immersed in oil or water. Particles which are partially hydrophobic attach to the interface.

Hydrophilic silica nanoparticles do not show any significant adsorption to the water/oil interface. Surfactants modify the wettability of nanoparticles due to the adsorption of surfactant molecules onto the particle surface, a process which is surfactant concentration-dependent. Figure 5.2 (a) shows the interaction mechanisms between negatively charged silica nanoparticles and cationic surfactant hexadecyl-trimethyl-ammonium bromide (CTAB). CTAB interacts with silica nanoparticles through electrostatic forces until the CTAB saturates the nanoparticle surface (hemimicelle). Hydrophobic interactions between carbon chains lead to the adsorption of additional CTAB molecules and the formation of ad-micelles at high CTAB concentrations. As a result of this process, the wettability of the particle changes from hydrophilic to hydrophobic with

the increase in the CTAB concentration and becomes hydrophilic again at very high CTAB concentrations [Maestro et al., 2012].

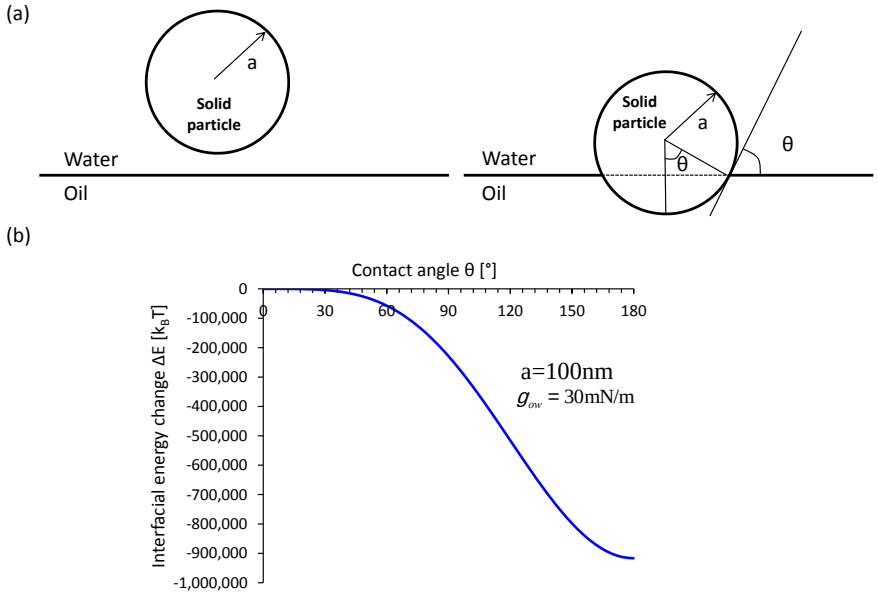

Figure 5.1. Interfacial energy change. (a) Transfer of a spherical particle from water to the water-oil interface. (b) The influence of the contact angle on the interfacial energy change. Note: the radius a=100nm, water oil interfacial tension γ_{ow}=30mN/m.

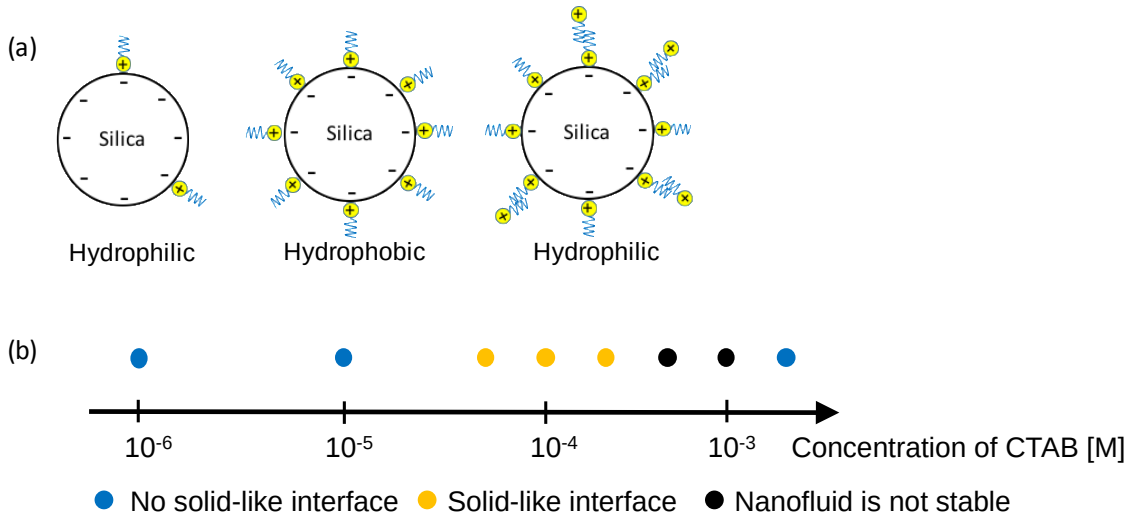

Figure 5.2. Film formation. (a) Particle-surfactant interactions. (b) The formation of the shell-like interface.

5.3 Experimental Study: Materials and Procedures

We carefully expand and shrink a nanoparticle-coated water/oil droplet to understand the mechanical response of the particle-coated interface during deformation. Details of the experimental setup and materials follow.

5.3.1 Materials

Experiments use silica nanoparticles (fumed silica from Sigma-Aldrich) with a hydraulic diameter of 100 nm measured by the dynamic light scattering method (Zetasizer Nano ZS, Malvern Instruments). CTAB tunes the wettability of the silica nanoparticle to promote its adsorption onto the interface. The CTAB has a purity>99% (Sigma-Aldrich).

Nanofluids are prepared by mixing nanoparticles with the CTAB solution and then sonicated for 40mins. The solution includes NaCl and NaOH to promote the adsorption of surfactants and increase the nanofluid stability. All solutions have a salt concentration C_{NaCl}=1mM and pH=10 (Ravera et al., 2006). Nanofluids used in this study have 0.5% nanoparticles by weight and different concentrations of CTAB (10^{-6}-2×10^{-3} M).

Mineral oil (Mineral Oil Light, from Sigma-Aldrich) has a density of 877 kg/m^3 and an interfacial tension of 34.2 mN/m measured by the pendent drop method (Attension Theta optical tensiometer, Biollin Scientific).

Borosilicate glass capillaries (from Drummond Scientific Company) have ID=0.56 mm and OD=0.79 mm. We use FDTS-coated capillaries for nanofluid in oil experiments and normal capillaries for oil in nanofluid experiments to ensure a stable and smooth droplet expansion and shrinkage.

5.3.2 Experimental Setup

Figure 5.3 shows the experimental setup which consists of a syringe pump, pressure transducer, and a glass capillary immersed in a reservoir. The experiment starts by filling the reservoir with either mineral oil or the nanofluid. A syringe pump delivers other fluids to the capillary tip. A droplet with the desired volume is created at a constant flow rate. The droplet is kept at rest for a certain time t_{ad} to allow nanoparticles to adsorb to the interface. Then we reduce the volume of the droplet by withdrawing the fluid with a flow rate q=0.2ml/hr. This slow rate ensures that the nanofilm is in a quasi-static condition throughout the withdrawal operation. After the entire droplet is withdrawn into the capillary, we may inject more fluids to expand the nanofilm. A microscope (ZEISS, Stemi 2000-CS) records the deformation of the droplet during expansion or shrinkage. A pressure transducer (OMEGA, PX40) measures the fluid pressure. The droplet may undergo several expansion and shrinkage cycles.

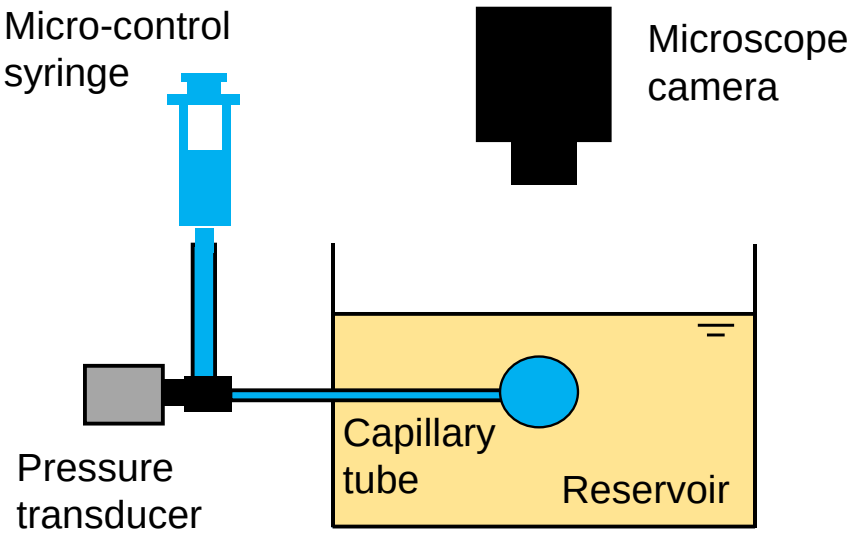

Figure 5.3. Experimental Setup.

5.4 Experimental Results

We conduct film formation experiments under CTAB concentrations which range from 10^{-6} M to 2×10^{-3} M. The interface behaves as a liquid-liquid interface when the concentration of CTAB is low (less than 10^{-5} M). The shell-like interfaces exist when the concentration of CTAB is between 10^{-5} and 2×10^{-4} M (Figure 5.2 (b)). All other experiments use a CTAB concentration of 8×10^{-5} M, as particles show strongest adsorption at this level. The study encompasses more than thirty droplet shrinkage and expansion tests, with both nanofluid droplet in oil and oil droplet in nanofluid settings. The adsorption time t_{ad} ranges from 5 min to 120 min. The test results are highly repeatable for the same experimental conditions. Although the droplet does not deform identically in each test, the response shows similar features which relate to the mechanical properties of the particle-coated interface. Sections 5.4.1 to 5.4.3 present typical examples.

5.4.1 Shrinkage of a Nanofluid drop in Oil

The shrinkage of a nanofluid drop in oil is tested with different adsorption times t_{ad} = 5, 10, 30 and 120 mins. Figure 5.4 presents the fluid pressure response and drop morphologies for t_{ad} = 10 mins. We identify four stages that characterize the interface deformation based on the evolution of the pressure and drop morphology.

Stage 1 (Point 1-2): the drop remains spherical and the pressure remains almost constant. This behavior is the same as the shrinkage of a water drop in oil, which indicates that the water-oil interfacial tension still governs the interface. The surface coverage of particles increases due to the reduction of the total interface area.

Stage 2 (Point 2-3): the drop is still spherical; however, the pressure starts to decrease. This observation suggests that the surface coverage of particles reaches a significant value and a non-trivial pressure is required to overcome the particle-particle interactions [Luu et al., 2013]. Therefore the overall interfacial tension decreases, which consequently lowers the pressure.

Stage 3 (Point 3-5): the interface begins to wrinkle when the pressure falls close to 0 Pa. The pressure remains constant as the interface buckles. The low pressure indicates the vanishing of the overall interfacial tension and suggests a compressive stress in the particle ensemble. The surface coverage of particles reaches the maximum level. A solid-like membrane is clearly visible. Both crumpling and mirror buckling are observed in different experiments.

Stage 4 (post point 5): a further decrease in pressure is required to withdraw the film into the capillary. There are occasional film break-offs.

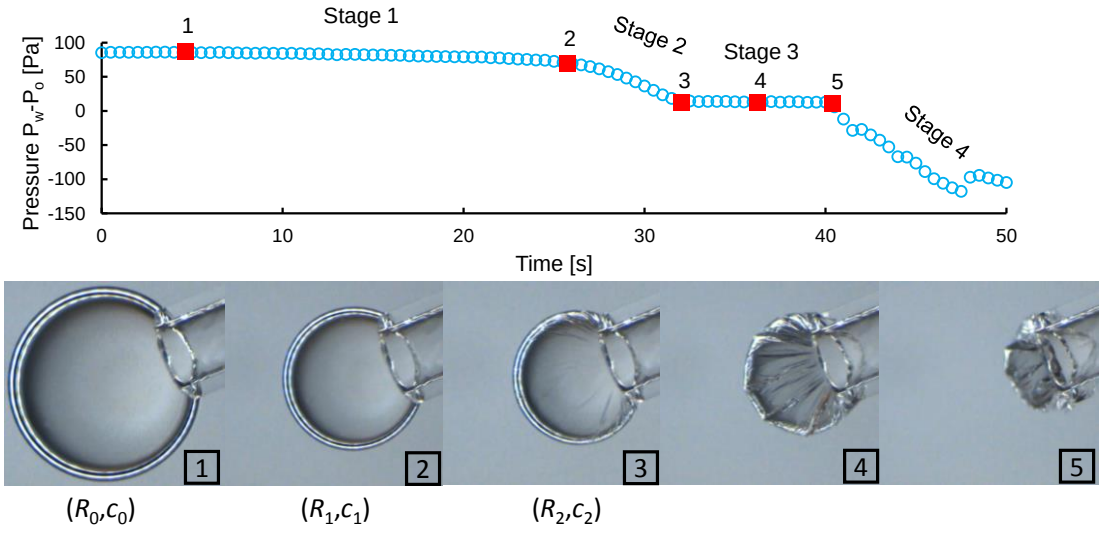

Figure 5.4. Shrinkage of a nanofluid drop in oil.

5.4.2 Shrinkage of an oil drop in nanofluid

To test the opposite condition, we reduce the volume of a mineral oil drop in a nanofluid reservoir. Figure 5.5 shows the experimental results after t_{ad} =10mins. The mechanical behavior is strikingly different from the nanofluid drop-in-oil case.

Stage 1 (before point 1): the drop keeps the spherical shape, and the pressure remains constant which is similar to the nanofluid drop-in-oil case.

Stage 2 (point 1-4): at the beginning, the pressure decreases while the top of the oil drop (the side farthest from the capillary) remains at a relatively constant curvature. As the pressure drops to 0 Pa (point 2 in Figure 5.5), several wrinkles appear at the bottom of the oil drop (the side closest to the capillary). Eventually, the drop deforms from a sphere to a semi-sphere (point 3). The pressure decreases below zero, which indicates an overall negative interfacial tension and a substantial compressive stress inside the particle ensemble. A further decrease in pressure causes localized wrinkles of the particle-coated interface which initiates from the bottom of the sphere and develops to the top (point 4). The particle ensemble sustains a pressure difference larger than 200 Pa (the pressure difference between points 1 and 4).

Stage 3 (point 4-5): finally, the drop becomes unstable and the film suddenly breaks off. A fresh water-oil interface forms and the pressure increases (point 5). A comparison of drop shapes between points 5 and 4 also shows a relaxation of the localized wrinkles after the failure. The broken film remains outside of the capillary thereafter.

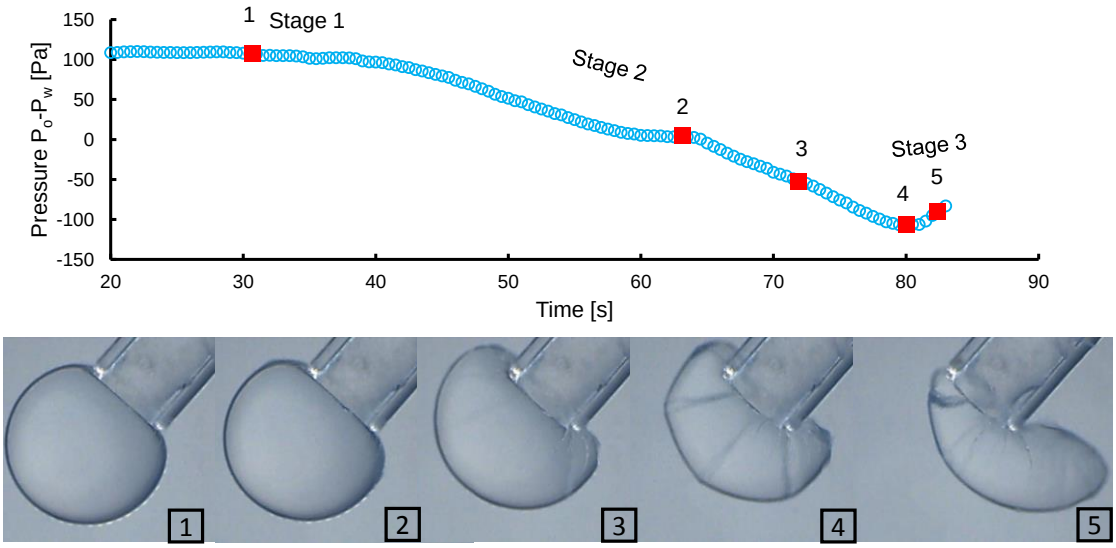

Figure 5.5. Shrinkage of an oil drop in the nanofluid.

5.4.3 Expansion of Particle-coated Interface

We perform expansion tests by increasing the volume of the drop after drop withdrawal tests. Figure 5.6 displays the result for a nanofluid drop in the oil reservoir. The interface is initially inside the capillary tube. At first, the pressure is slightly above zero (point 1). The folded film expands and forms a relatively smooth interface as the volume of the drop increases (point 1 to 2). Meanwhile, the pressure also increases. However, the pressure does not reach the maximum when the curvature of the interface is at its largest value. This deviates from the prediction of the Young-Laplace equation with the interface remaining solid-like. Suddenly the folded film turns out, which creates a hump at the interface (point 3). The hump gradually flattens and the interface becomes spherical (points 3-5). The particle-coated interface ruptures during this process. Pieces of particle aggregations are clearly seen floating on the interface. The pressure reaches the maximum

level at point 5 and then starts to decrease. This suggests that the interface becomes more fluid-like.

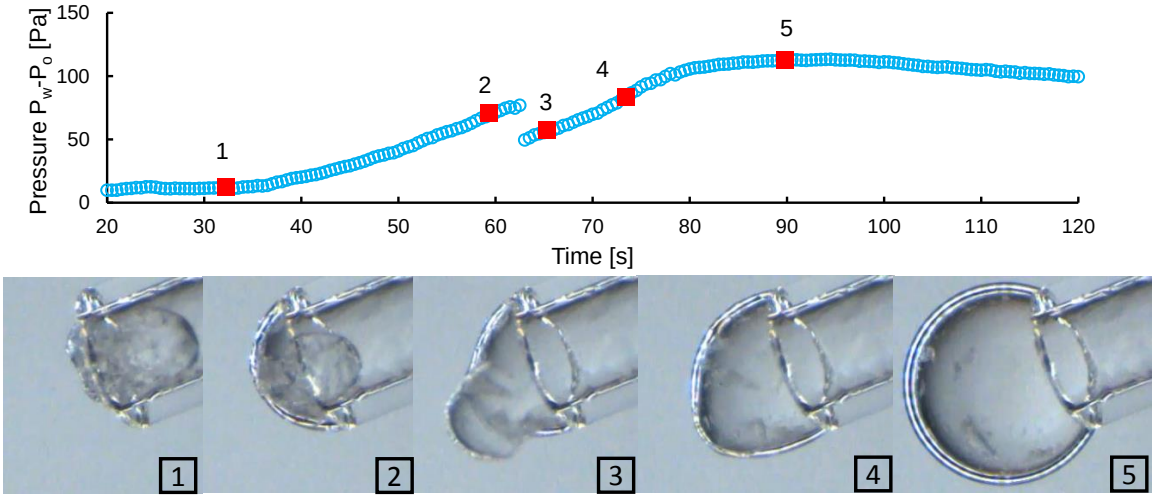

Figure 5.6. Expansion of a nanofluid drop in oil.

5.5 Analyses and Discussion

Particle-coated interfaces shift from fluid-like to solid-like during shrinkage. Although this mechanical response has been studied by the Langmuir trough method and modeled as an elastic film, the effect of the granular character and the interface curvature remains unclear. Our results showed distinct stages of drop deformation. We demonstrated a marked difference in the mechanical response between the nanofluid drop-in oil and oil drop-in-nanofluid cases. In this section, we analyze results and consider the granular character and particle-interface interactions.

5.5.1 Packing and Time Effect

The mechanical response of the particle-coated interface is determined by the particle packing, i.e. the arrangement pattern of particles on the interface. The particle

packing becomes denser because the surface area of the particle-coated interface decreases and the surface coverage of particles increases. This process resembles the consolidation of granular materials in 2D, where particles are packed and undergo an in-plane rearrangement (see examples in Monteux et al., 2007). The consolidation results in increased inter-particle stresses. The packing gradually reaches the densest state, and further shrinkage results in the collapse of the interface [Bordacs et al., 2006; Deshmuikh et al., 2015].

Let's define the state of a particle-coated interface as (R, c), where R is the drop radius and $c=A_{particle}/A_{interface}$ is the surface coverage of particles. Three key states mark the transition of the behavior of the particle-coated interface, which can be identified from the pressure signature and morphology evolution. Particles are randomly distributed on the interface (point 1 in Figure 5.4) at the initial state (R_0, c_0). A clear decrease in pressure (point 2 in Figure 5.4) marks a loose packing state (R_1, c_1), which indicates particles are subject to compression. Finally, the interface reaches a dense packing state (R_2, c_2), which is the densest packing the system can achieve and indicates the onset of buckling (point 3 in Figure 5.4). Figure 5.7 illustrates the entire process.

The surface coverage can be inferred from the relationship between the radius and surface coverage, which is:

$$\frac{R_a}{R_b}=\sqrt{\frac{c_b}{c_a}} \tag{5.4}$$

So the initial surface coverage c_0 can be expressed as:

$$c_0 = c\frac{R^2}{R_0^2} \tag{5.5}$$

We assume a square packing c_1 = 78.5% for a loose packing state, and a triangular packing c_2 = 90.7% for a dense packing state. Note that inter-particle interactions and collapse can occur at a surface coverage smaller than the ideal values assumed here [Berhanu and Kudrolli, 2010].

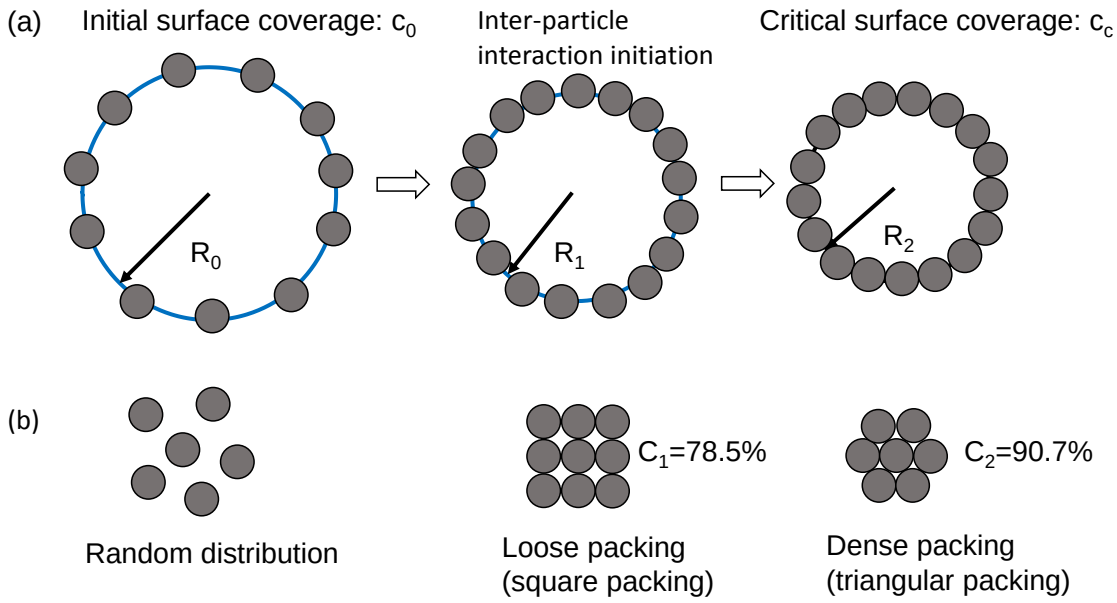

Figure 5.7. The evolution of surface coverage and particle packing during the compression of a particle-coated interface.

We measure the R_0, R_1, and R_2 with adsorption time t_{ad}=5, 10, 30, and 120 mins to understand the kinetics of particle adsorption. Figure 5.8 shows the evolution of R_2/R_0, R_1/R_0, and R_2/R_1 with adsorption time. The R_2/R_1 is around 0.9 and is independent of the adsorption time, which is consistent with the model prediction:

$$\frac{R_2}{R_1} = \sqrt{\frac{c_1}{c_2}} = 0.93 \tag{5.6}$$

Both R_1/R_0 and R_2/R_0 increase with adsorption time, which indicates an increase of the initial surface coverage with adsorption time. Figure 5.8 plots the initial surface coverage calculated from R_2/R_0 and the surface coverage c_2 based on Eq. 5.5.

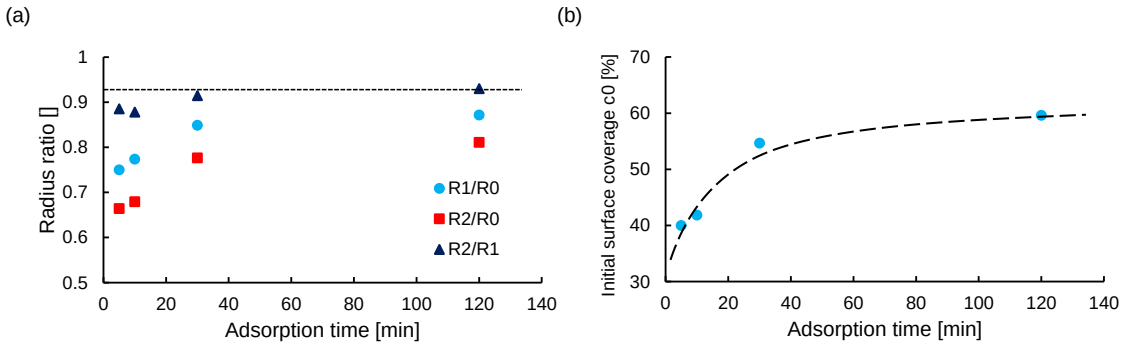

Figure 5.8. Time effects. (a) Relationships between R_1/R_0, R_2/R_0, and R_2/R_1 and adsorption time. (b) Surface coverage as a function of adsorption time.

The diffusion with a Stokes-Einstein diffusion coefficient cannot describe the adsorption process. The diffusion-controlled adsorption at the early stage changes to an interaction-controlled assembly as the surface coverage of nanoparticles increases [Ferdous et al., 2011]. The presence of an energy barrier to adsorption provides an effective diffusion coefficient orders of magnitude smaller than the Stokes-Einstein diffusion coefficient [Kutuzov et al., 2007; Ward and Tordai, 1946]. The results agree with previous studies which use the pendant drop method [Maestro et al., 2014; Du et al., 2010; Kutuzov et al., 2007; Ferdous et al., 2011], interfacial rheology [Yazhgur et al., 2013] and TEM images [Boker et al., 2007].

5.5.2 Asymmetric Behaviour

Discrete particles can form stable arch structures and withstand a substantial load. The ratio of the arch length to the particle size can rarely exceed 8 for spherical particles

[Valdes and Santamarina, 2008; Garcimartin et al., 2010]. The stability of the granular arch depends on the particle shape and inter-particle friction [Lozano et al., 2012]. When a particle chain is under normal compression, an out-of-plane deformation of particles can cause a rolling or sliding failure of the chain as shown in Figure 5.9 (c).

However, the ratio of the diameter of the capillary tube to the nanoparticle size exceeds 5000 in our experiments. Therefore, other mechanisms must contribute to the stability of the particle chain. Large pressure differences and the effect of interfacial tension indicate that the particle shells are able to withstand a large normal force. Furthermore, the particle-coated interface shows an asymmetric behavior where the pressure difference is larger in the oil drop-in-nanofluid case than that in the nanofluid drop-in-oil case. We consider the inter-particle contact, wettability and the capillary interaction between particles and the interface in the following analyses.

A single particle at the fluid-fluid interface experiences a capillary force normal to the interface when it is out of the equilibrium position. Consider a spherical particle with a radius *R* at the water-oil interface and a polar angle ϕ (Figure 5.9 (a)). To move the particle to a specific polar angle, the force needs to balance the vertical component of the capillary force [Rapacchietta and Neumann, 1977], which is:

$$F = 2\pi RT \sin(\theta - \phi)\sin(\phi) \tag{5.7}$$

where γ is the water-oil interfacial tension, and θ is the contact angle. Figure 5.9 (b) shows the force required to move the particle to a specific polar angle. First the force increases with the polar angle, then it drops after it reaches a maximum value.

The capillary force caused by the out-of-plane deformation not only maintains the equilibrium of a single particle, but also stabilizes particle chains. Consider a chain of particles under normal compression. Let's assume that the water-oil interface is flat between particles given the fact that the radius of interface curvature (in the order of 1 mm) is much larger when compared to the size of the particle (100 nm). The relative position of a particle at the interface depends on the contact angle θ. This configuration of the liquid interface with particles has been seen in optical microscopy images [Bordacs et al., 2006], freeze-fracture SEM images [Subramaniam et al., 2006] and cyro-SEM images [Deshmukh et al., 2015]. We assume an out-of-plane perturbation of the particle (defect of the chain) with an angle α (Figures 5.9 (d) and 5.9 (e)). The movement of the particle into one fluid and out of its equilibrium position causes a counter-force induced by capillarity.

The capillary force in the presence of the water-oil interface stabilizes the chain of particles. This stabilization mechanism is curvature-dependent. The rolling friction between particles can also help to stabilize the chain. It depends on the particle size and is in the order of 10^{-10} N for 100 nm particles [Heim and Blum, 1999; Dominik and Tielens, 1995]. We can compute the normal force in the equilibrium condition based on the force balance (Figures 5.9 (d) and 5.9 (e)):

$$F_N = \frac{F}{2\sin\frac{\alpha}{2}} + \frac{f_{rolling}}{\sin\alpha} \tag{5.8}$$

The computed maximum normal force with an out-of-plane angle α is shown in Figure 5.9 (f). The effect of rolling friction vanishes as the angle α increases. If the particle chain deforms towards the oil, the normal force required to further bend the chain decreases

as α increases. In other words, continuous failure will happen once the normal force reaches the maximum force in the initial equilibrium condition. However, if it deforms towards the water, the force required to bend the chain increases with α until a maximum value is reached. Therefore the particle chain is a self-stabilizing system and can undertake more loading.

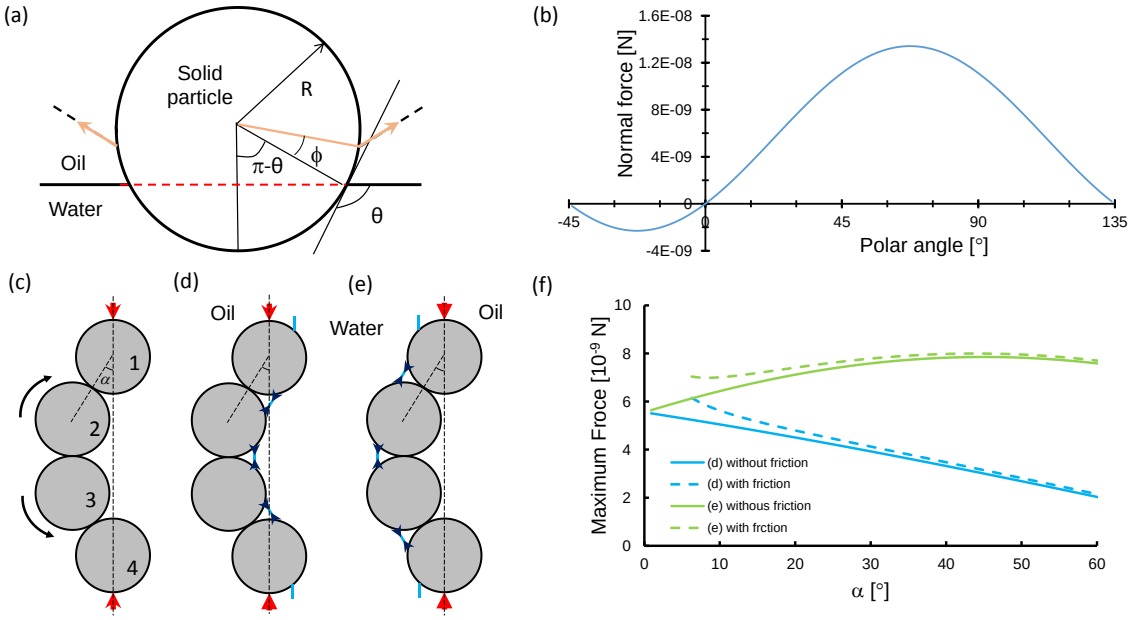

Figure 5.9. Asymmetric behavior. (a) A single particle at the fluid-fluid interface. (b) Capillary force and polar angle. (c)-(e) The deformation of a particle chain with or without particle-interface interactions. (f) The maximum force the particle chain can withstand without deformation. Case parameters: interfacial tension γ =0.05 N/m, particle radius R=50 nm, contact angle θ=135°, rolling friction f=10^{-10} N.

The computed normal force is in line with our experimental measurements. First, the asymmetric behavior matches the model prediction that the oil drop-in-nanofluid case can withstand a higher pressure difference. In addition, the inter-particle contact force F_N can be evaluated from the experimentally measured pressure difference Δp:

$$\Delta p \cdot \pi r^2 + 2\pi r \cdot \gamma = N \cdot F_N \tag{5.9}$$

where N is the number of particles in one circumference, and $N=\pi r/R$. Therefore:

$$F_N = \left(\Delta p \cdot r + 2\gamma\right) \cdot R \tag{5.10}$$

F_N=1.2×10^{-8} N when the pressure difference is 100 Pa. This value coincides with our analytical model, although our model is 1D and the experimental condition is 2D.

Although the proposed model does not consider other possible particle-interface interaction mechanisms (e.g., adhesion forces, pinning of interfaces, and contact angle hysteresis, see Bresme and Oettel, 2007; Guo et al., 2004. And dipolar electric fields, see Nikolaides et al., 2002), our analyses highlight that particle-interface interactions affect the global mechanical behavior and cause the asymmetric behavior. This finding is consistent with other studies. Datta et al. (2010) suggested that the buckling and crumpling of nanoparticle-coated droplets are supported by both localized stresses in particle rafts and capillary forces. Studies of capillary wave propagation along the particle-coated interface suggest the bending stiffness of the interface is controlled by the particle size, surface tension and contact angle [Planchette e al., 2011]. In a recent molecular dynamics simulation [Sicard and Striolo, 2017], the role of the fluid-fluid interface to the buckling of particle-stabilized droplets is clearly shown. In addition, the formation of particle-stabilized emulsions from oil in water to water in oil depends on the wettability of the particle [Binks and Murakami, 2006; Kralchevsky et al., 2005], which may relate to the asymmetric behavior described here. Note that a similar asymmetric behavior has been

observed in membrane bending by protein-protein crowding [Stachowiak et al. 2012, J. Derganc et al. 2013].

5.5.3 Buckling patterns

The buckling patterns of thin elastic films strongly depend on the boundary conditions [Niezgodzinski and Swiniarski, 2010], initial size and surface coverage, deformation rates [Vliegenthart and Gompper, 2011], and the Föppl–von Kármán (FvK) number which describes the ratio of stretching energy to bending energy.

Two distinct patterns were observed among all experiments: buckling and crumpling. Here we refer to buckling as a mirror-like deformation with countable depressions and crumpling as deformations with numerous wrinkles. A hydrophilic glass capillary results in buckling and a hydrophilic FDTS coated glass capillary always leads to crumpling patterns (Figure 5.10 (a)). The wettability of capillary tubes modifies the boundary conditions with changes to the interaction between the particle-coated film and the boundary. The hydrophobic interaction [Meyer, Rosenberg and Israelachvili, 2006] between the FDTS and the CTAB-modified silica particles may generate a non-slip boundary condition. The slip boundary condition exists in the case of hydrophilic glass capillaries.

Furthermore, we are able to manipulate the number of depressions during buckling with the control of the initial surface converge of particles. Figure 5.10 (b) presents buckling patterns with a different number of depressions ($N>4$, $N=3$, and $N=2$). From left to right, the initial surface coverage of particles increases. All buckling patterns are symmetric. A large initial surface coverage results in a small number of depressions.

Further studies are required to fully understand the relationship between the mechanical properties of the nanoparticle-coated interface and buckling patterns.

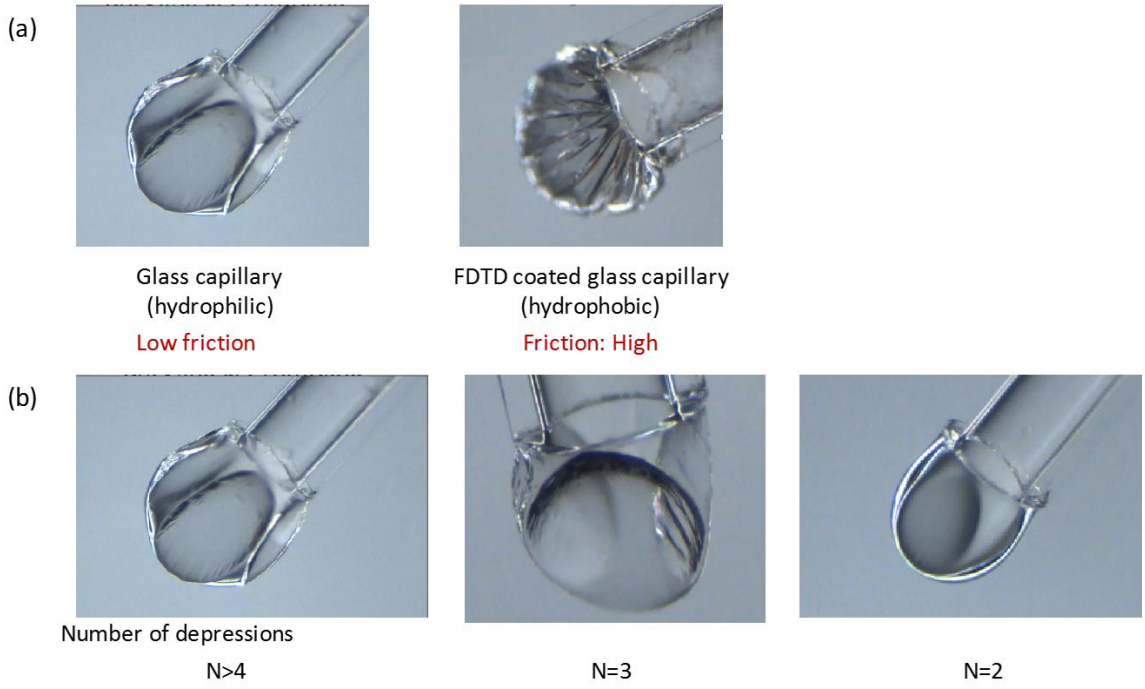

Figure 5.10. Buckling and crumpling patterns. (a) The influence of boundary conditions. (b) The influence of the initial surface coverage: the initial surface coverage increases from left to right.

5.6 Effects on Immiscible Displacement

Nanofluids and nanoparticle-stabilized emulsions have been applied in laboratory studies of enhanced oil recovery [Zhang et al., 2010; Luo et al., 2016]. However, the underlying mechanisms remain unclear. There are wettability alterations and a decrease in interfacial tension [Al-Anssari et al., 2016; Moghaddam et al., 2016], but few studies have considered the transport of particle-coated interfaces or droplets in porous media [Gai et al., 2017; Mei et al., 2016]. Note that in oil systems, asphaltenes, biofilms, and fine particles can also adsorb to the oil-water interface and form a composite with similar properties of

particle-coated interfaces [Gao et al., 2009; Kim et al., 2013; Ruhs et al., 2013; Kang et al., 2008].

Since pores in sediments have converging-diverging cross-sections, interfaces expand or shrink during traveling through porous media. Localized instabilities such as Haines jumps and snap-offs occur during fluid displacement due to the interaction of interfaces with the non-uniform pore geometry [Jang et al., 2016]. These microscale instabilities affect macroscale displacement patterns [Holtzman and Segre, 2015]. In addition, Saffman-Taylor fingering occurs in Hele-Shaw cell studies when a low viscosity fluid displaces a high viscosity fluid, thus resulting in a large portion of residual liquid [Saffman and Taylor, 1958]. These instabilities hinder resource recovery.

The particle-coated interface can alter both multiphase flow through a converging-diverging pore and the fingering pattern in a fracture [Sun and Liu, unpublished]. The shrinkage of the particle-coated interface lowers interfacial tension and even collapses when passing through the pore throat. This completely altered the pressure signature and instability behavior (Figure 5.11 (a)). The asymmetrical behavior is also observed when the interface passes through the pore throat which suggests that the interfacial behavior depends on the curvature of the interface and also the wettability of the particle. Fractal-like fingering patterns are observed when nanofluids displace oil in a Hele-Shaw cell with Plexiglas plates, which is different to the Saffman-Taylor instabilities when water displaces oil (Figure 5.11 (b)). A better understanding of the effects of particle-coated interfaces on multiphase flow in porous media will assist the development of potential applications for oil/gas recovery, CO_2 geological storage, and ground contamination remediation.

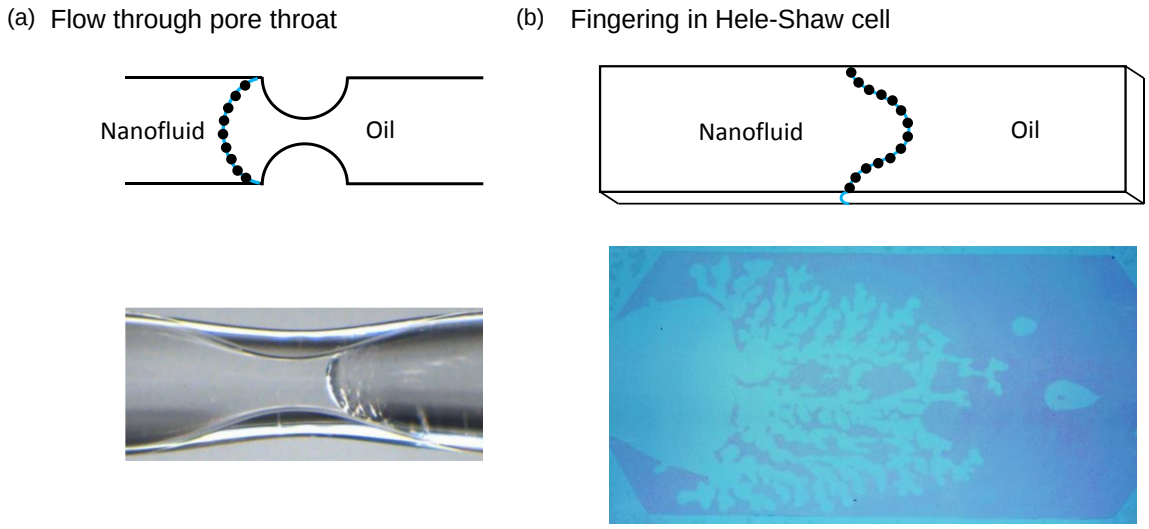

Figure 5.11. Effects of particle-coated interfaces on flow phenomena. (a) The nanoparticle-coated interface traverses a pore throat. (b) Abnormal fractal fingering: nanofluid (0.5% Silica nanoparticle, 8×10^{-5}M CTAB) displaces mineral oil.

5.7 Conclusions

This chapter documented the study of silica nanoparticle-coated interfaces. The experimental approach analyzed the pressure signature and morphology of an oil or water drop covered with nanoparticles during shrinkage and expansion. Salient results follow.

The interface undergoes a transition from fluid-like to solid-like as the volume of the droplet reduces. Analyses suggest that nanoparticles evolve from loose packing to dense packing with increases in surface coverage. Further compression of the closely packed particles results in the buckling of the particle-coated interface.

The adsorption kinetics of nanoparticles at the interface is studied by comparing the mechanical response of droplets with different adsorption times. Our results are consistent with previous studies and confirm a diffusive, time-dependent rate of coverage.

The particle-coated interface exhibits an asymmetric, curvature-dependent mechanical behavior: the response of a nanofluid drop in oil and an oil drop in nanofluid show salient differences during shrinkage. For an oil drop in nanofluid, the particle-coated interface withstands a significant pressure difference before collapse. However, the nanofluid drop in oil buckles at a negligible pressure difference. Analyses of the stability of particle chains demonstrate that the particle-interface interaction provides an additional supporting force that prevents the particle chain failure and is responsible for this asymmetric behavior.

Our work emphasizes the granular character of the particle-coated interface, the effects of particle-particle/interface interactions on the global behavior, and its inherent asymmetric behavior. Findings in this study are relevant to practices related to Pickering emulsions and studies on particle-coated interface transport in porous media.

CHAPTER 6. INVASION PATTERNS INDUCED BY NANOPARTICLE-COATED INTERFACES

6.1 Introduction

Instabilities can develop when a low-viscosity fluid displaces a more viscous fluid. Hele-Shaw cell results clearly demonstrate viscous fingering or Saffman-Taylor instability [Hill et al., 1952; Saffman and Taylor, 1958]. Fingering limits hydrocarbon recovery efficiency and volume occupancy in geological CO_2 storage [Muggeridge et al., 2013; Espinoza and Santamarina, 2010].

Fingering phenomena between Newtonian fluids has been extensively studied in Hele-Shaw cells [Homsy, 1987]. Surface tension stabilizes the interface at short wavelengths; and the capillary number defines the width of stable fingers [Mclean and Saffman, 1981; Bensimon et al., 1986; Tabeling et al., 1987]. Non-uniform surface tension leads to fingers of varying widths [Bonn et al., 1995; Dorsey and Martin, 1987; McCloud and Maher, 1995; Zocchi et al., 1987]. The fingering pattern also differs in non-Newtonian fluids (e.g. shear-thinning, shear-thickening, and frictional fluids) [Lindner et al., 2000; Sandnes et al., 2011; Kondic et al., 1998].

Particles may assemble and form a monolayer at the interface between immiscible fluids. Then, the interfacial behavior can transform from fluid-like to shell-like [Datta et al., 2010]. The concept of particle-coated interfaces has been applied to stabilize emulsions and for drug delivery [Binks, 2002; Chevalier and Bolzinger, 2013; Frelichowska et al., 2009], and could be applied to enhanced oil recovery or geological CO_2 storage whereby

nanoparticles can improve the displacement efficiency [DiCario et al., 2011; Worthen et al., 2014; Luo et al., 2016]. In addition, asphaltenes, biofilms, and clay particles can also adsorb to the oil-water interface [Gao et al., 2009; Kim et al., 2013; Ruhs et al., 2013; Kang et al., 2008]. Therefore, it is important to understand the effects of particle-coated interfaces on both capillary phenomena and instabilities during fluid displacement.

Few studies have investigated this problem. Podgorski et al. (2007) showed various fingering instabilities when a gel-like material forms at the interface between two solutions. These instabilities were attributed to the viscoelastic rheology of the gel. The formation and destabilization of particle bands on the fluid-fluid interface when the particle size is comparable to the gap thickness can cause inversed fingering [Kim et al., 2017; Tang et al., 2000]. Instabilities take place when the moving interface collects particles [Bihi et al., 2016] which alters the mechanical behavior of the interface [Monteux et al., 2007; Ravera et al., 2008].

This study investigates the effects of nanoparticle-coated interfaces on fluid displacements in a radial Hele-Shaw cell. First, we run experiments in microfluidic channels and glass capillaries to understand how the particle-coated interface affects flow. Then we use mineral oil to displace a nanofluid with silica nanoparticles and observe abnormal fingering patterns. The physical model developed to analyze the experimental results considers nanoparticle adsorption and the mechanical properties of the nanoparticle-coated interface.

6.2 Materials

The nanofluid is similar to the fluid described in Chapter 5. Nanofluids are prepared by mixing 0.5% silica nanoparticles with 8×10^{-5} M hexadecyl-trimethyl-ammonium bromide (CTAB) solution and then sonicated for 40mins. Nanofluids have a pH=10 by adding NaOH solution. Silica nanoparticles (fumed silica from Sigma-Aldrich) have a hydraulic diameter of 100 nm measured with the dynamic light scattering method (Zetasizer Nano ZS, Malvern Instruments). The cationic surfactant CTAB (Sigma-Aldrich) has a purity higher than 99%. The mineral oil used in this study is the same as the oil used in Chapter 5.

The behaviour of the nanoparticle-coated interface was investigated in Chapter 5. Figure 6.1 shows the change in the mechanical response of the interface as it changes from fluid-like to shell-like when coated entirely with particles.

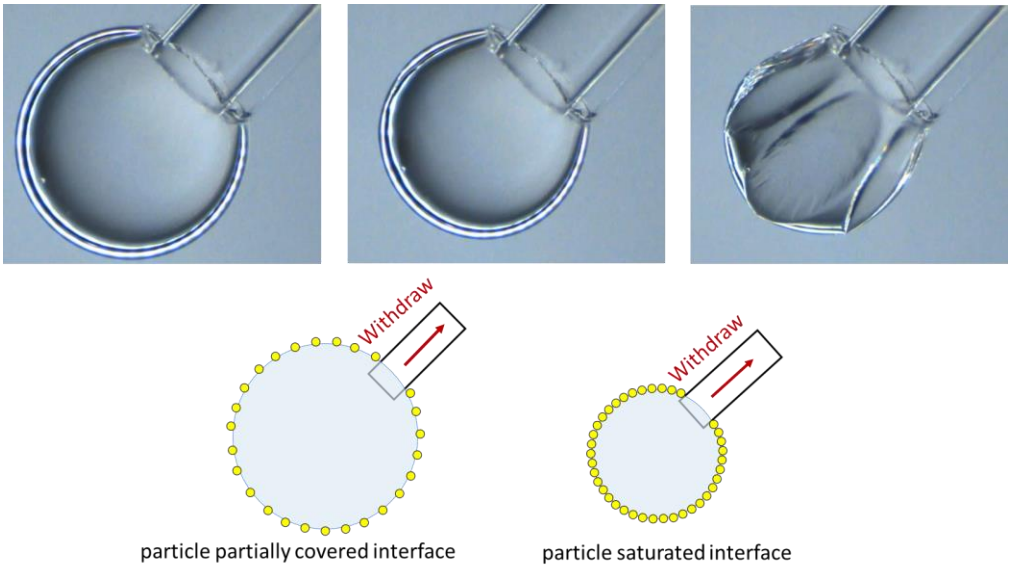

Figure 6.1. The shell-like behavior of silica nanoparticle-coated interfaces.

6.3 Experimental Study

Before studying the displacement of a nanofluid and a mineral oil in a radial Hele-Shaw cell, we first investigate the displacement in a microfluidic channel and a capillary tube to understand the behavior of the particle-coated interface when it flows in pore spaces.

6.3.1 Displacements in a Microfluidic Channel and a Capillary Tube

6.3.1.1 Experimental Setup and Procedure

The microfluidic chip is made of PDMS, which is oil-wet. The channel is 25 mm long. The cross-section of the channel is a rounded rectangle (height×width: 0.1 mm × 0.5 mm).

The borosilicate glass capillary tube is 75 mm long and has a circular cross-section with an internal diameter ID=0.97mm. A constriction located in the middle of the capillary has a pore throat diameter ID=0.3mm.

Figure 6.2 (a) shows the experimental setup. The microfluidic channel or the capillary tube is filled with the nanofluid and connected to a nanofluid reservoir. The other end of the channel or the tube is connected with a pressure transducer (OMEGA, PX40) and a syringe. We use a syringe pump (Braintree Scientific, Inc., BS-8000) to inject the mineral oil at a constant flow rate. The pressure transducer records pressure change in oil during the displacement. A stereo microscope (ZEISS, Stemi 2000-CS) records the interface evolution. The capillary number in all tests are low and is in the order of 10^{-6}.

Note that in order to maintain a similar interfacial configuration, i.e. a wetting phase displaces a non-wetting phase, we use oil to displace the nanofluid in the microfluidic channel which is oil-wet. By contrast, the nanofluid displaces oil in the glass capillary which is water-wet.

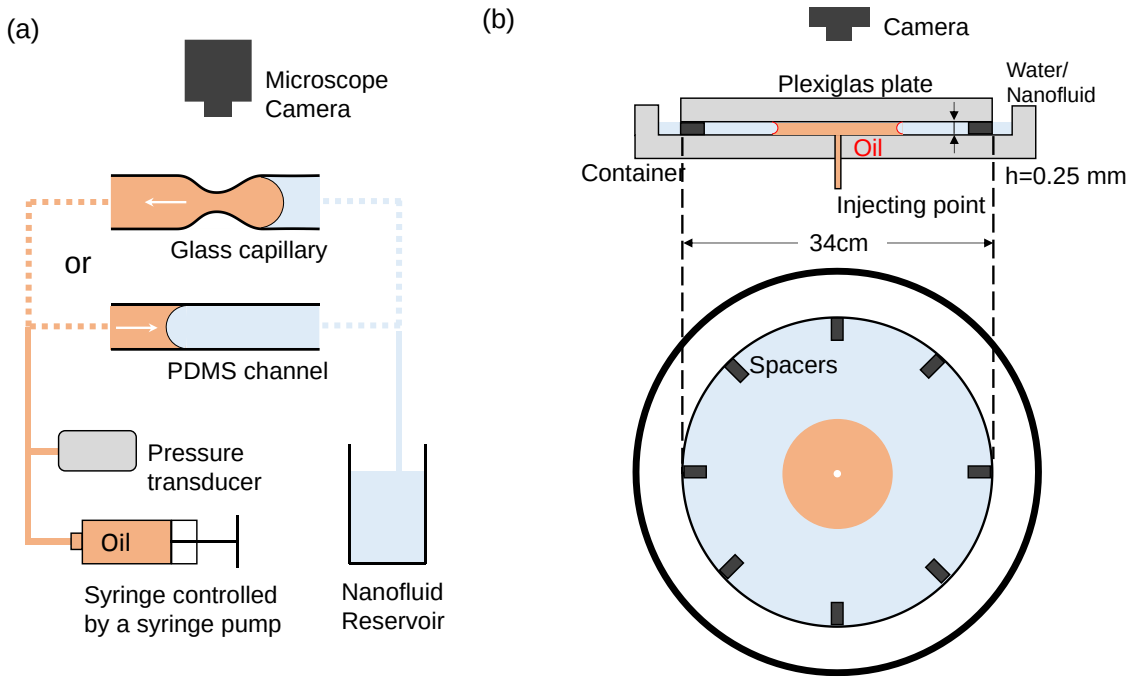

Figure 6.2. Experimental setups. (a) Flow in a glass capillary or microfluidic channel. (b) Flow in a radial Hele-Shaw cell.

6.3.1.2 Results

Figure 6.3 displays the evolution of the interface during displacement in the microfluidic channel. The interface behaviour deviates from the Young-Laplace description. By attaching to the channel surface, the interface forms a structure which resists flow. Finally the interface breaks off with part of it pinning to the surface. This suggests that not only the interface, but also the interaction between the interface and the solid surface contributes to the flow resistance.

Figure 6.4 shows both the pressure signature and the interface evolution when the interface passes through the pore constriction. There are three phases in this process. Before the interface is entirely coated with particles, the interface is fluid-like; therefore the pressure in the oil increases when the radius of curvature of the interface decreases (*Phase 1*). In *Phase 2*, the pressure decreases which indicates that the interface behaviour deviates from the Young-Laplace prediction and suggests the formation of a shell-like film. At the same time we observe wrinkles and crumples on the interface, along with a further drop in pressure. This is because the particle-coated interface acts as a solid shell against the capillary wall, which resists the flow. After passing the narrowest point, the interface expands and the pressure recovers (*Phase 3*).

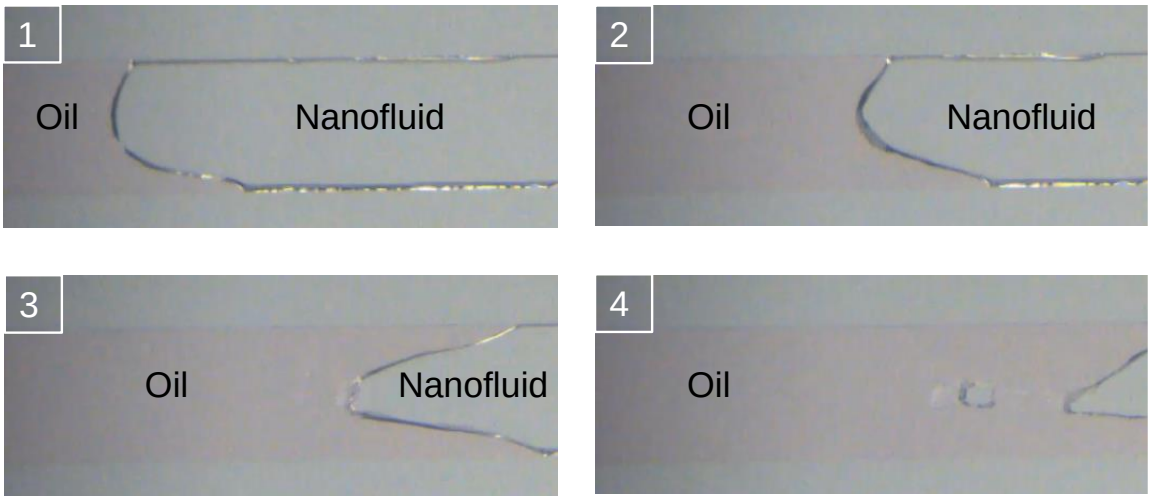

Figure 6.3. Disturbed interface as it advances in a microfluidic channel.

Results from both experiments suggest that the particle-coated interface can resist flow by attaching to the channel surface or forming an arch structure. Therefore a higher pressure in the displacing phase is required to deform and advance the particle-coated interface. Once the particle-coated interface breaks, flow becomes easier.

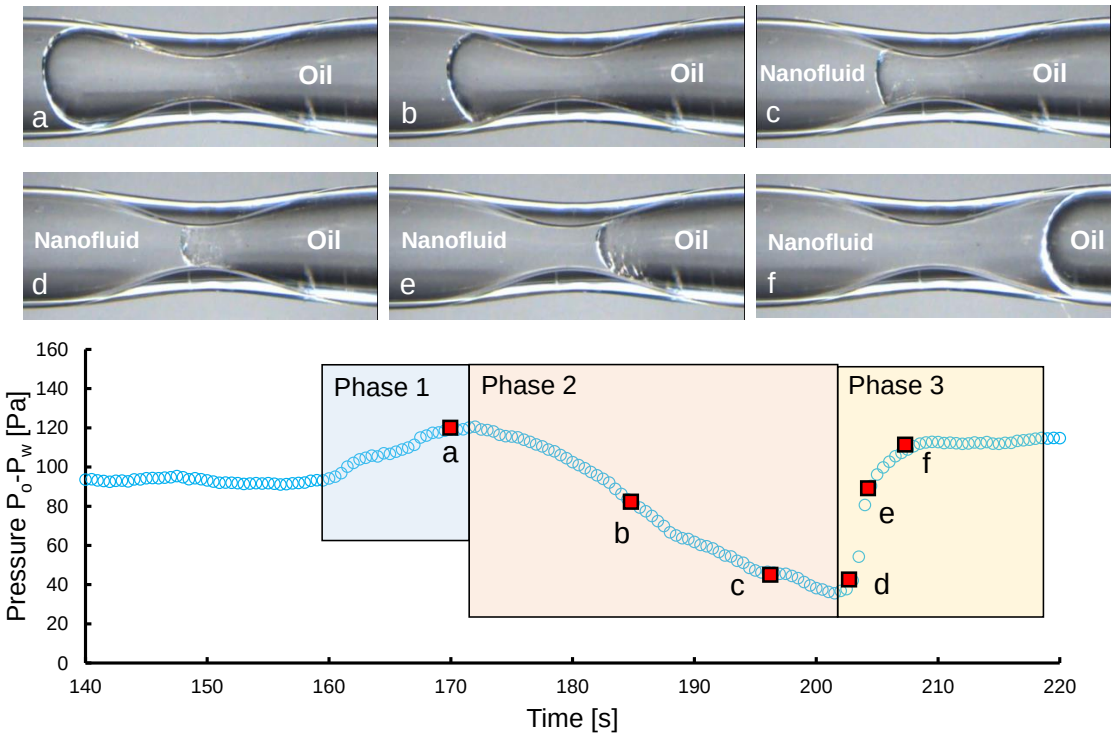

Figure 6.4. Interface transits a pore constriction in a borosilicate glass capillary tube.

6.3.2 Displacements in a Radial Hele-Shaw Cell

6.3.2.1 Experimental Setup

Figure 6.2 (b) shows the experimental setup. The radial Hele-Shaw cell comprises two circular Plexiglas glass plates (10 mm thick) of radius 170 mm and 200 mm, respectively. The bottom plate is part of a container filled with the nanofluid. Rigid plastic spacers separate the two plates, thus creating a thin cell with a thickness h=0.25 mm. Note that the thickness of the cell is more than 2500 times larger than the size of the nanoparticle, therefore it is not possible to form any particle arches or bands.

The plates are cleaned with a commercial detergent, isopropanol alcohol, and distilled water before each test. A syringe pump injects the mineral oil into the cell at a

constant flow rate. Tested flow rates range from 0.5 mL/hr to 8 mL/hr. A camera (Sony, α5000) over the radial Hele-Shaw cell records the displacement.

6.3.2.2 Results

We test the displacement between the oil and water before investigating the displacement between the oil and nanofluid. When oil displaces water, there is no instability, and the interface propagates as smooth circles (Figure 6.5 (a)). This agrees with the theory that the displacement front is stable as a more viscous fluid pushes a less viscous fluid.

However, instabilities develop when oil displaces the nanofluid. Figure 6.5 (b) shows an example in which the flow rate starts at 10 mL/hr and slows down to 2 mL/hr. In the beginning, the interface propagates as circles. The propagation speed of the interface slows down as the circle expands. Suddenly, oil flows out from several spots on the boundary and develops "local" stable displacements. The flow in these bulges is much faster than elsewhere. These bulges grow and render a mushroom-like invasion topology. As these mushrooms becomes larger, they merge together, thus forming a circular front and leaving nanofluid trapped surrounding the stems of mushrooms.

Additional tests use flow rates which ranges from 0.5 mL/hr to 8 mL/hr. Figure 6.6 (a)-(c) shows the evolution of the displacement front for cases with flow rates q=0.5 mL/hr, 2 mL/hr, and 8 mL/hr, respectively. In all cases, the interface develops mushroom-like instabilities, which is consistent with observations previously described. Remarkably, the lower the flow rate, the smaller the radius at which mushroom-like invasion topology emerges.

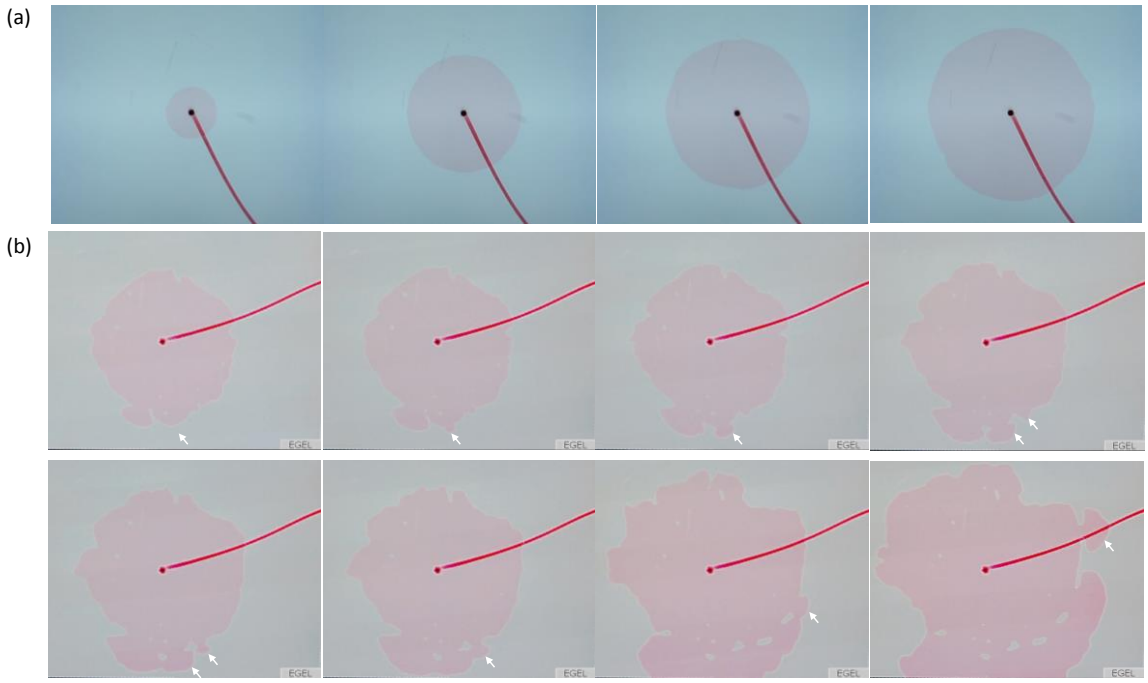

Figure 6.5. Radial fluid invasion in a Hele-Shaw cell. (a) Stable displacement between oil and water. (b) Mushroom-like invasion topology when oil displaces the nanofluid.

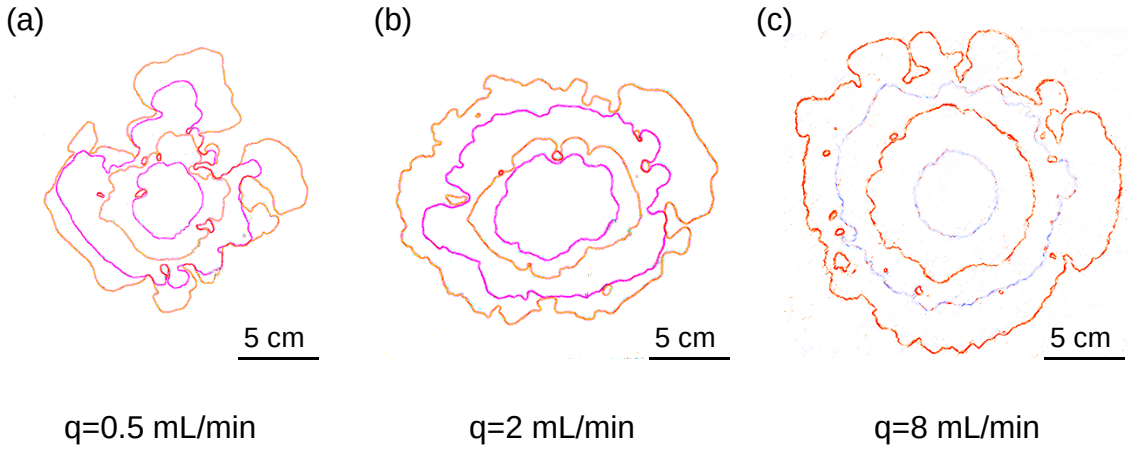

Figure 6.6. Displacement patterns at different flow rates when oil displaces the nanofluid in a radial Hele-Shaw cell.

6.4 Discussion

The displacement is stable when a more viscous Newtonian fluid displaces a less viscous Newtonian fluid; however, we observe mushroom-like invasion topology when the oil displaces the naonfluid. We anticipate the formation of a particle-coated interface as the interface propagates. The break of this interface requires higher pressure and creates the mushroom-like invasion topology.

There are two competing processes which alter the surface coverage of nanoparticles on the interface. First, the increase in the area of the interface tends to lower the surface coverage (Figure 6.7 (a)). Let us assume oil is injected at a constant flow rate q. In the beginning, oil expands as circles. The area of the interface increases with time:

$$S = 2(\pi h)^{1/2} q^{1/2} t^{1/2} \tag{6.1}$$

Second, particles adsorb to the interface, which increases the surface coverage (Figure 6.7 (b)). For simplicity, we adopt a diffusion-controlled adsorption kinetics until the surface concentration C reaches a critical value C_c at t_c [Kutuzov et al., 2007]:

$$C(t) = kt^{1/2} \tag{6.2}$$

where k relates to the diffusion coefficient of nanoparticles. Therefore the increase of number of particles on the interface can be expressed as:

$$dN = S \cdot dC + C \cdot dS = 2k(\pi h)^{1/2} q^{1/2} dt \tag{6.3}$$

Thus the particle concentration on the surface is:

$$C = \frac{N}{S} = kt^{1/2} \tag{6.4}$$

This equation suggests that the particle concentration on the surface increases with time. At the beginning, the particle concentration is low, so the interface behaves as fluid-like. The displacement is stable and the surface is smooth and circular (Figure 6.7 (c)). Both the radius of the interface and the surface coverage of nanoparticles increase with time. When the surface coverage reaches the critical value C_c at t_c, the interface no longer behaves fluid-like. Instead, it resists flow as shown in experiments in the microfluidic channel and in the capillary tube. Once the shell-like interface breaks, oil flows out as a temporary and local stable invasion. Overall, the invasion gains a mushroom-like topology.

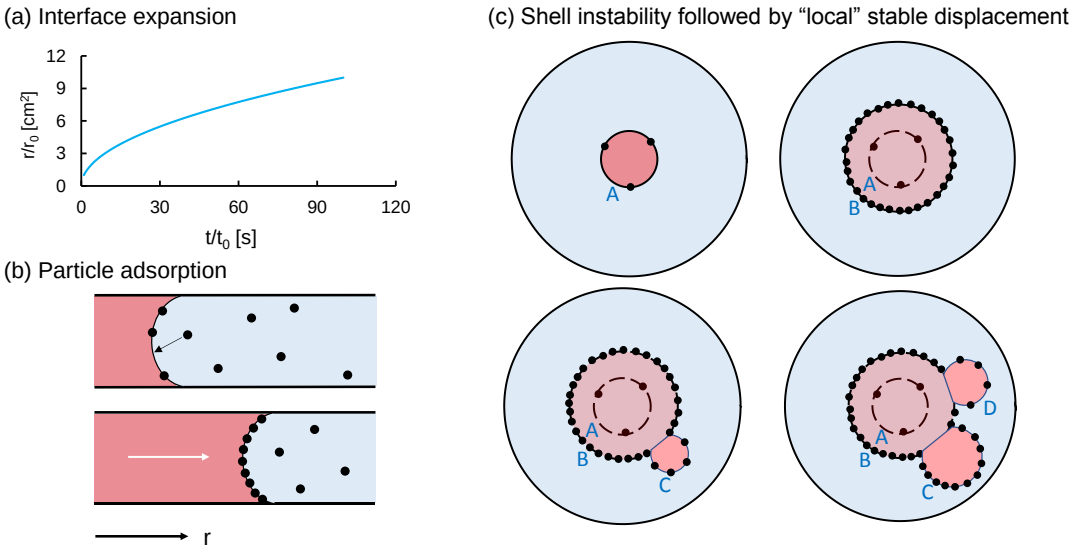

Figure 6.7. Proposed physical model. (a) The radius of the interface increases with $t^{1/2}$. (b) Particle adsorption on the interface. (c) The formation of mushroom-like invasion topology.

We can obtain a relationship between the flow rate and the critical radius where the mushroom-like invasion topology occurs:

$$r_c = \left(\frac{t_c}{\pi h}\right)^{1/2} q^{1/2} \tag{6.5}$$

This relationship suggests that the higher the flow rate, the larger the critical radius. Figure 6.8 plots the measured critical radius as a function of the flow rate. Experimental data confirms the model prediction.

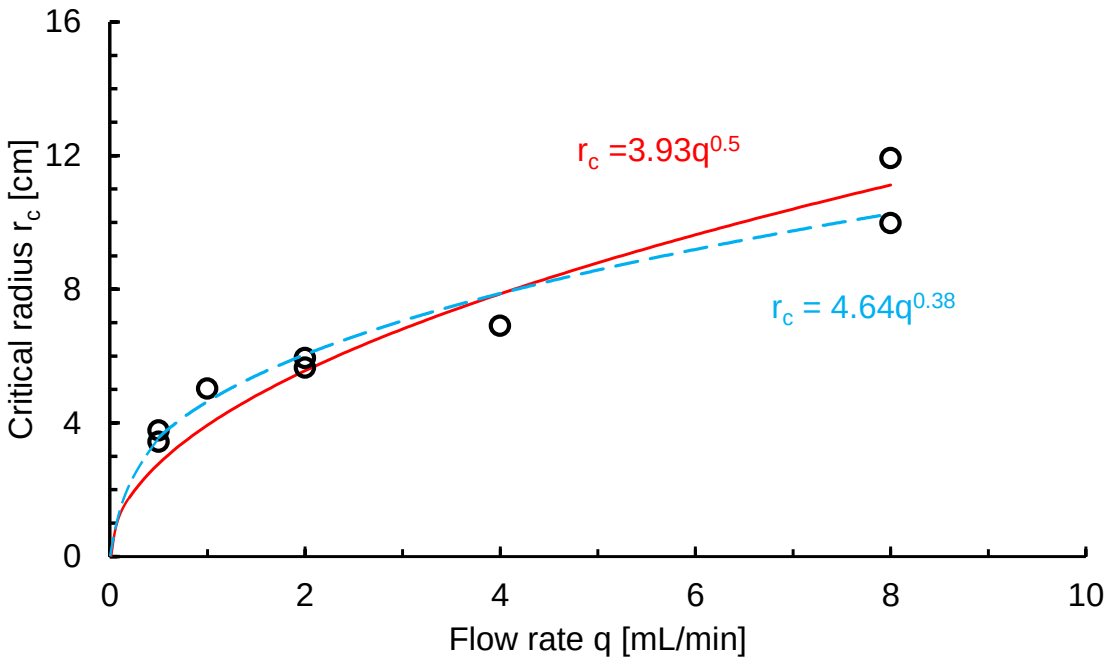

Figure 6.8. Measured critical radius vs. flow rate.

6.5 Conclusions

This chapter documented the study of the effect of nanoparticle-coated interfaces on flow. In particular, we observe mushroom-like invasion topology during the displacement of a less viscous fluid by a more viscous fluid in a radial Hele-Shaw cell. This result deviates from the stable displacement pattern expected when $\mu_{inv}>\mu_{def}$.

The mushroom-like pattern results from the formation of a nanoparticle-coated interface during displacement. The nanoparticle-coated interface resists flow; the shell-like interface breaks and allows fast flow and the growth of mushroom-like "local" stable displacements. The critical radius where the instabilities occur depends on the flow rate because nanoparticle adsorption on the interface is time dependent. The lower the flow rate, the smaller the critical radius.

Experiments in a microfluidic channel and a capillary tube confirm the assumption that the nanoparticle-coated interface resists flow. In the microfluidic channel where the cross-section is a thin rectangle, we observe the break-off of the nanoparticle-coated interface and the pinning of the interface on the microfluidic channel surface. In the circular capillary tube, the nanoparticle-coated interface crumples and requires a higher pressure to push through a constriction.

These findings suggest that shell-like films such as the nanoparticle-coated interface may have a significant effect on flow in porous media. This is critical for hydrocarbon recovery, geological CO_2 storage, and contamination remediation. In these applications, the adsorption of nanoparticles, fine particles, biofilms, and asphaltenes on the fluid interface can alter the interfacial behavior and affect the displacement efficiency.

CHAPTER 7. TIME-DEPENDENT PORE FILLING

7.1 Introduction

Capillarity traps fluids in porous media and affects hydrocarbon migration [Dickey, 1975; Dembiki and Anderson, 1989], hydrocarbon extraction [Chatzis et al., 1983; Oren et al., 1992; Babadagli, 2007; Muggeridge et al., 2014], groundwater contamination by non-aqueous phase liquids and subsequent remediation efforts [Rao et al., 1997; Soga et al., 2004; Essaid et al., 2015], geological CO_2 storage [Espinoza and Santamarina, 2010; Andrew et al., 2014], and sediment-atmosphere interactions [Gens, 2010; Shin and Santamarina, 2011].

Laboratory studies often focus on short-term fluid trapping during either wetting or non-wetting fluid invasion (e.g. classical work by Dullien, 1992 and Lenormand et al., 1983). In these conditions, capillary, viscous, and gravitational forces, together with the topology of the porous network determine displacement patterns and trapped fluid distribution. Related processes include a wide range of pore-scale instabilities such as Haines jumps and snap-offs [Berg et al., 2013; Jang et al., 2016; Rossen, 2003], and viscous or capillary fingering at the macroscale [Lenormand et al., 1988; Zhang et al., 2011].

However, recovery, remediation, and storage are long-term processes and are not necessarily dominated by the same mechanisms that are significant in the short term. Nonaqueous phase liquids (NAPLs), CO_2 and air have a finite solubility in water although they are often treated as immiscible [Mercer and Cohen, 1990; Spycher et al., 2003]. This experimental pore-scale study explores the fate of trapped fluids after invasion and

displacement (i.e., after the flow by advection and capillary-driven counter flow), and examines the roles of diffusion, capillarity, wettability and pore geometry on changes in saturation over time.

7.2 Experimental Study

We use time-lapse microscopy to record the evolution of trapped fluids in capillary tubes under quasi-static conditions. The experimental setup (Figure 7.1) consists of a stereo microscope (Leica DMS300) and a flat glass beaker; the auto-filling bottle maintains a constant water depth in the glass beaker (h=12 mm). A capillary tube filled with a preselected fluid is immersed into the water-filled beaker. There is no pressure gradient acting on the capillary; both ends are submerged and not connected to the atmosphere (unlike the boundary conditions in Gruener et al., 2012). The evolution of pore filling is recorded using time-lapse photography; the time interval between photographs varies from 1 min/frame to 10 min/frame to avoid aliasing internal processes. Experiments last from 2 days to over 6 months.

Tests involve borosilicate glass capillaries to represent water-wet pores and perfloroalkoxy alkanes (PFA) capillaries for oil-wet pores. Table 7.1 describes the geometry and size of all capillaries used in this study. The tubes have a (1) circular cross section, (2) circular section with a thin internal rod of borosilicate glass sitting inside the tube, and (3) a square cross section. The two non-circular cross sections are analogues to the complex geometry of natural pores and allow capillary water invasion along corners. Capillaries are not pre-treated and only used once. The tested fluid pairs represent various gas-liquid and liquid-liquid interactions: air-water, benzene-water, hexane-water and

toluene-water (DI water: milli-Q water. Benzene, hexane and toluene: from Sigma-Aldrich). Table 7.2 lists their mutual solubilities, diffusion coefficients and interfacial tensions.

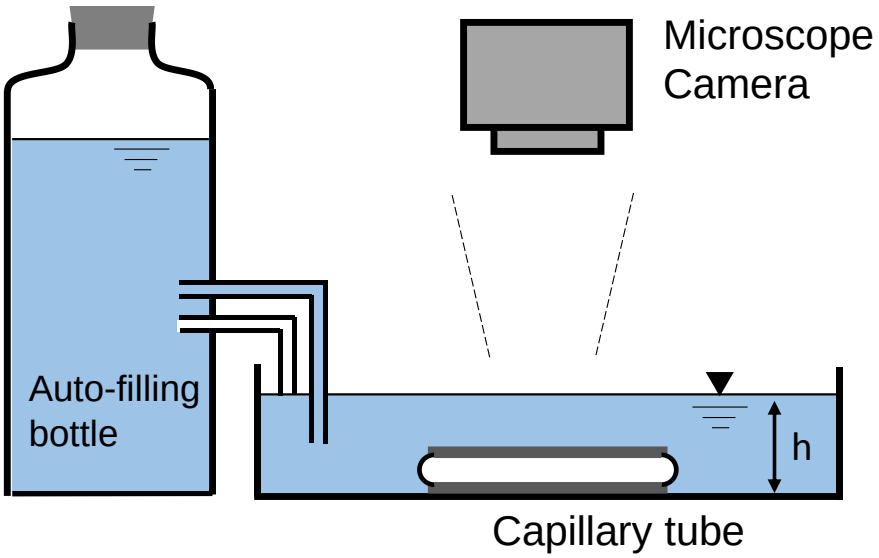

Figure 7.1. Experimental Setup. A capillary tube filled with a preselected fluid is immersed into the water-filled flat beaker. The water level in the beaker is maintained constant by the auto-filling bottle.

7.3 Results

The experimental study allows comparisons between gas-water and liquid-water interactions, water-wet and oil-wet systems, and different pore sizes and geometries. Salient observations based on water-air systems follow. Complementary results obtained with other fluid-pairs and analyses are presented in subsequent sections.

7.3.1 Short-term: Initial Corner Flow and Water Vapor Condensation.

Figure 7.2 shows snapshots of the evolution of water saturation within an initially air-filled capillary tube during the first 800 minutes of water submersion. Two cases are

shown: a) a capillary tube with a circular cross-section, and b) the same cylindrical tube with a thin rod sitting at the bottom (see Table 7.1 for geometric details).

Table 7.1. Capillary tubes: sizes and cross sections.

	Cross-section	**Length [mm]**	**Diameter or Width [mm]**	**Volume [mm^3]**
Borrosilicate Galss	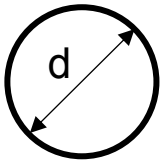	8	d = 0.94	5.55
	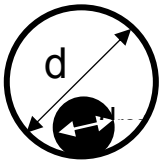	8	d = 0.94 d_{rod} = 0.17	5.37
	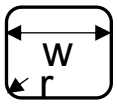	4	w = 0.1 r = 0.015	0.04
PFA	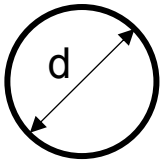	8	d = 1.5	14.13

Water evaporates into the air-filled capillary and starts condensing on the capillary wall adjacent to the water-air interface (Figure 7.2 (a)). Water droplets first appear close to the water-air interface and then develop into the center of the capillary. Droplets closer to the water-air interface also have a larger volume. The condensation pattern reflects the gradual diffusive transport of the water vapor from the water-air interface to the space inside the capillary.

Table 7.2. Fluid properties. Data gathered at 20°C unless otherwise noted.

Fluids		Molecular structure♥	Density [kg/m^3]	Solubility in water [g/L]	Diffusion coefficient [cm^2/s]	Water solubility [g/L]	Diffusion coefficient [cm^2/s]	Interfacial tension with water [mN/m]
Air	O2 21%; N2 78%		1.2	0.0089 (O_2) 0.0138 (N_2) (1atm) [25 °C]	2×10^{-5} (O_2); 2×10^{-5} (N_2) [25 °C]♦	0.017	0.242♦	72
Hexane	C_6H_{14}	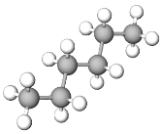	660.3♣	0.014♣	0.85×10^{-5} [25 ° C]♠	0.009♣	Not found	51♣
Benzene	C_6H_6	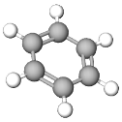	876.5♣	1.733♣	1.02×10^{-5} ♦	0.582♣	Not found	35 ♣
Toluene	C_7H_8	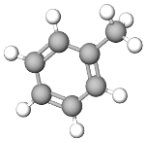	866.9♣	0.542 [25 °C]♣	0.85×10^{-5} ♦	0.464 [25 °C]♣	6.19×10^{-5} [25 °C]♦	36 [25 °C]♣

♥ molview.org
♣ Demond and Lindner (1993)
♦ Haynes (2014)
♠ Montgomery (2007)

In the tube shown in Figure 7.2 (b), the high initial curvature next to the internal rod at the base ($1/r_{arc}>2/r_{main}$) promotes capillary-driven water flow along corners [Dong and Chatzis, 1995; Bico and Quéré, 2002; Weislogel, 1996]. Rapid corner flow expels air out of long capillaries within seconds after the tube is submerged in water (counter-current imbibition, see Unsal et al., 2007)). The condensation of water on the wall is more uniform in this case in comparison to Figure 7.2 (a) because the fast initial invasion along the corners places water throughout the full length of the tube.

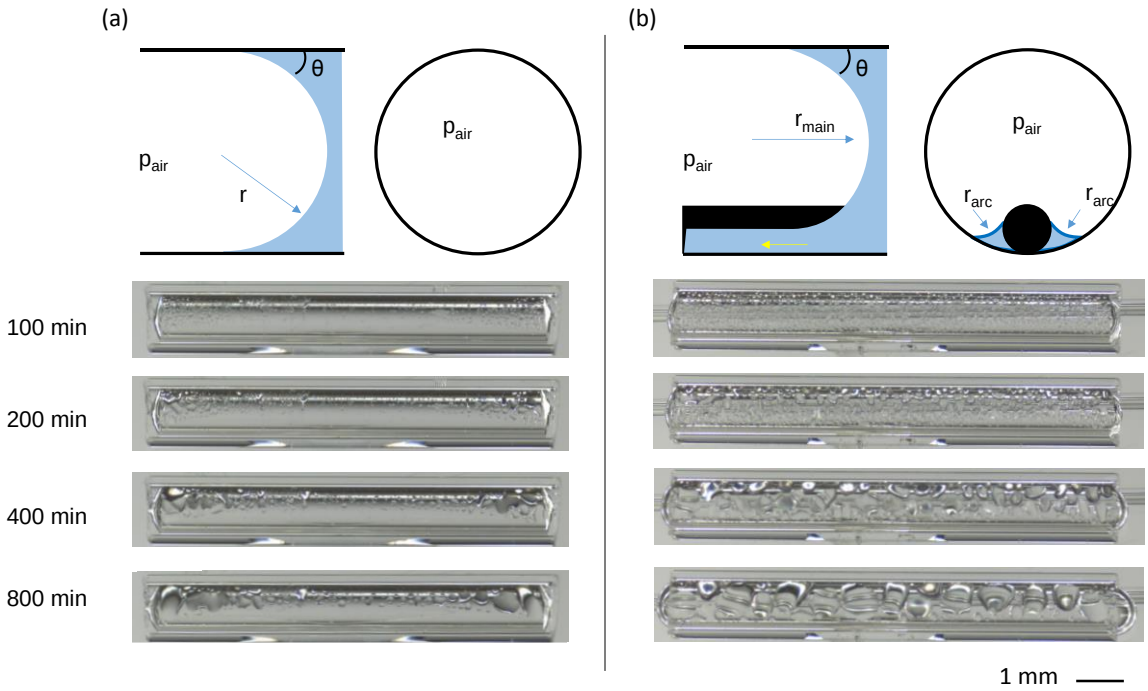

Figure 7.2. Water vapor condensation patterns in air-filled capillaries. Patterns observed in (a) a cylindrical capillary, and (b) a cylindrical capillary with a thin internal rod to create a non-circular cross section. Time starts when the air-filled capillary is submerged in water. Capillary: borosilicate glass, *d*=0.94 mm.

7.3.2 Long-term Pore Filling Processes

Figure 7.3 presents the evolution of pore filling in the water-air system during the first 120 days. There are two concurrent transport sequences: (1) water evaporation, transport and condensation into the air-filled space, and (2) air dissolution and diffusion out of the capillary tube. Water drops condense on the pore walls, gradually enlarge and may form a water collar inside the capillary. Eventually, collars become unstable and suddenly close-in to form water blocks across the pore. These newly formed water blocks split the air bubble into segments. The interfacial energy decreases as small droplets coalesce into water blocks.

Water blocks develop close to the open ends of cylindrical tubes, and anywhere inside the non-cylindrical capillaries where corner flow facilitates water transport into the capillary (Figure 7.3, day 20). These blocks continue to grow by water vapor diffusion and condensation, and by merging water droplets that have condensed on the nearby pore wall. Eventually water blocks connect with the water in the container.

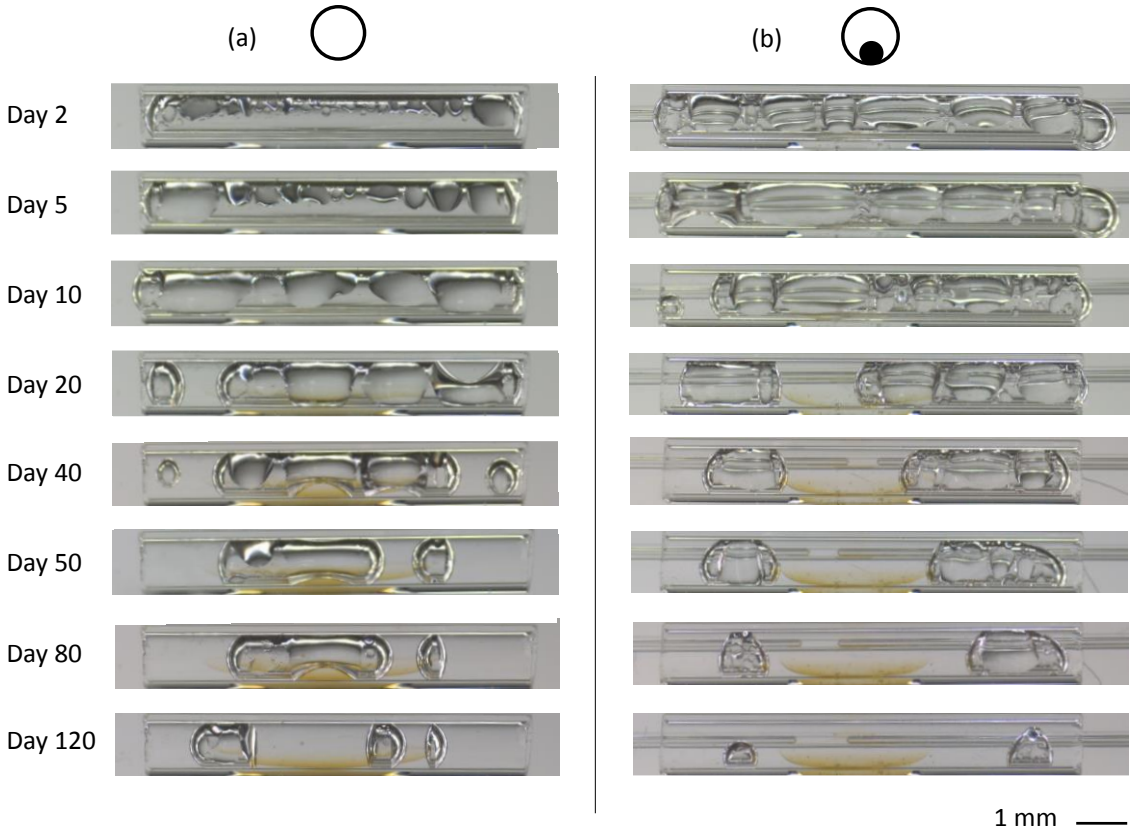

Figure 7.3. Long-term pore filling processes in the air-water system: (a) a cylindrical capillary, and (b) a cylindrical capillary with a thin internal rod to create a non-circular cross section. Time starts when the air-filled capillary is submerged in water. Capillary: borosilicate glass, d=0.94 mm.

7.4 Analyses

7.4.1 Diffusive Transport

Trapped air diffuses into the water and gradually leaves the capillary. The underlying processes combine pressure dissolution and diffusion. First, the air pressure in the capillary is higher than outside the capillary (Young-Laplace equation, assuming perfect wetting. See radii of curvature in Hsu et al., 2012)):

$$p_{air} - p_{water} = \frac{2\gamma}{r} \tag{7.1}$$

where γ is the surface tension, and r is the radius of the capillary tube. Second, gas solubility in water c_p is pressure-dependent (Henry's Law):

$$c_p = H^{cp} p \tag{7.2}$$

where Henry's constant is H^{cp} = 7.1×10^{-4} mol·L^{-1}·atm^{-1} for nitrogen and H^{cp} = 14×10^{-4} mol·L^{-1}·atm^{-1} for oxygen at 20°C. Therefore, the solubility of air in water inside the capillary is higher than in the surrounding bulk water, and the concentration gradient sustains air transport.

7.4.2 Rate of Capillary Filling

Figure 7.4 shows pore filling data for different fluid-pairs. The volume of trapped gas or hydrocarbon decreases over time in all tests.

The displaced defending fluid may form an external droplet at the end of the capillary and gradually dissolve into the surrounding bulk water. Figure 7.4 (a) displays

the dissolution rate of a spherical benzene droplet in water. The analytical solution accurately predicts the changing droplet radius $a(t)$ as a function of the initial radius a_0 [m], the diffusion coefficient D [m^2/s], the saturated concentration c_{sat} [kg/m^3], the concentration in the far field c_0 [kg/m^3], and the fluid density ρ [kg/m^3] (see derivation in the Appendix A) [Crank, 1975; Epsein and Plesset, 1950]:

$$a(t)^2 - a_0^2 = -\frac{D(c_{sat} - c_0)}{\rho} t \quad \textit{spherical diffusion} \tag{7.3}$$

Experimental results show that the interface can either remain pinned to the end of the capillary pore or move-in symmetrically from both open ends (Table 7.3). For example, the air-water interfaces in Figure 7.3 (a) are either pinned or stay at the edge of the capillary before day 40 and move into the capillary on day 50. Consequently, the pore filling rate also changes as shown in Figure 7.4 (b). When transport is controlled by pinned interfaces, the dissolution rate is constant, and the length filled with water x is linear with time t in a capillary of radius r (see derivations in the Appendix A):

$$x = \frac{2D(c_{sat} - c_0)}{\rho r} t \quad \textit{pinned interface} \tag{7.4}$$

However, when the interfaces move into the capillary as the defending fluid dissolves into the water, the filled length x increases with $t^{1/2}$ (see Appendix A):

$$x = 2\sqrt{\frac{2D(c_{sat} - c_0)}{\rho} t} \quad \textit{free interface} \tag{7.5}$$

Thus, the pore filling rate becomes slower as the diffusion length increases in the free interface model. Model predictions agree with experimental measurements and associated micro-photography sequences that identify either pinned or free interfaces. Figure 7.4 shows data and fitted models for pore filling processes in benzene-water, toluene-water, and air-water. The pinned and free interface models are two extreme conditions. The true evolution of saturation shown in Figures 7.2 and 7.3 demonstrates complex behavior with additional phenomena described below.

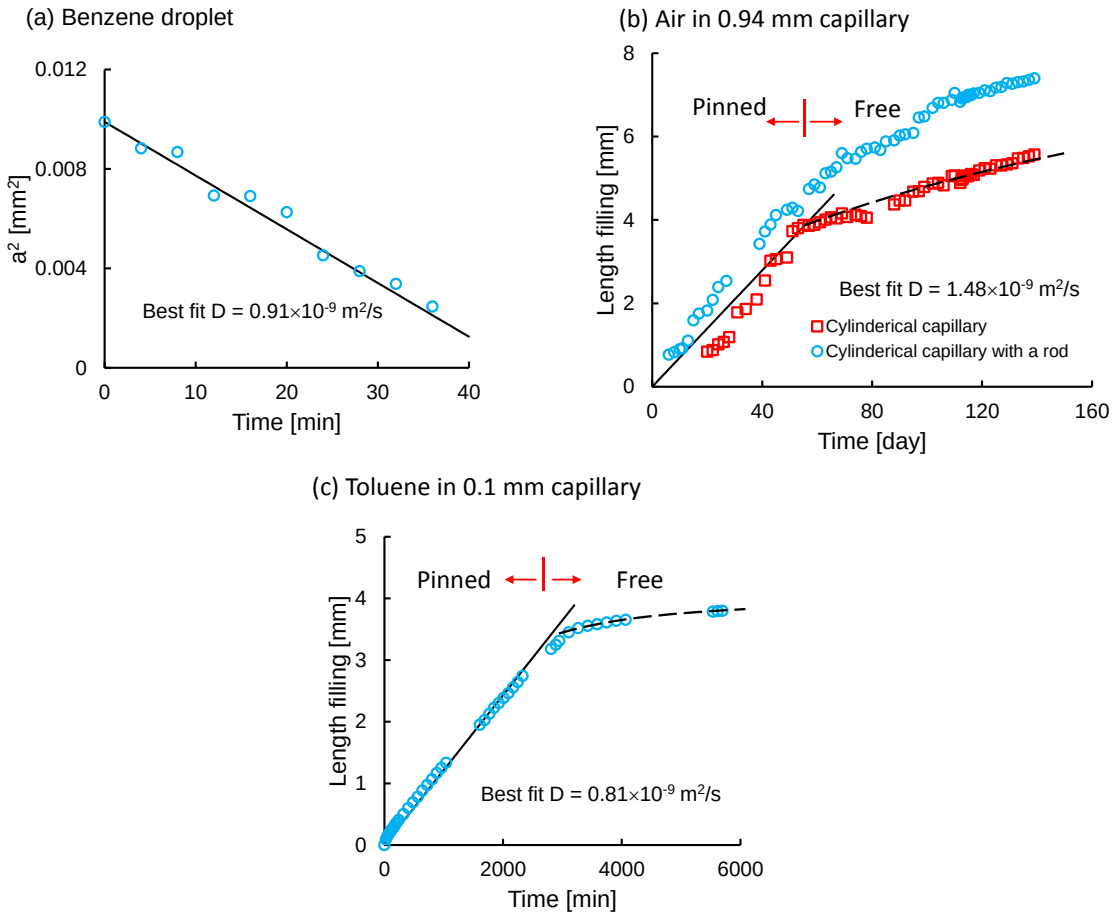

Figure 7.4. Fluid volume changes over time. Experimental data and analytical models. (a) Dissolution of a spherical benzene droplet in water; (b) air-filled 0.94 mm capillary; (c) toluene-filled 0.1 mm capillary. Note: Solid lines and dashed lines correspond to predictions (Eq. 7.3, 7.4, or 7.5).

Table 7.3. Dissolution and pore filling models.

Model	Sketch	Equation
Dissolution of a sphere bubble/drop	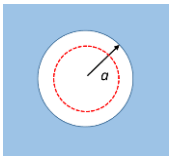	$a(t)^2 - a_0^2 = -\frac{D(c_{sat} - c_0)}{\rho} t$
Pore filling with free interfaces	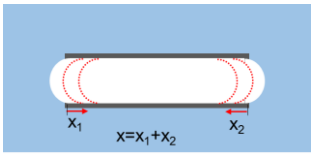	$x = 2\sqrt{\frac{2D(c_{sat} - c_0)}{\rho} t}$ (for $x>r$)
Pore filling with pinned interfaces	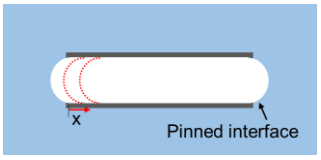	$x = \frac{2D(c_{sat} - c_0)}{\rho r} t$
Pore filling with one pinned interface	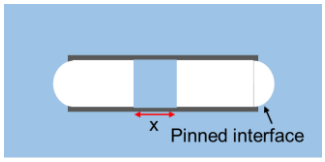	Between free interfaces case and pinned interfaces case

7.4.3 Other Phenomena Involved in Pore Filling

In general, experimental results show that diffusion controls the long-term pore filling process. However, other concurrent phenomena identified in this study affect pore filling. These are described next.

Condensation. Surface heterogeneities and defects create favorable sites for vapor condensation as the water vapor saturates the capillary in the air-water system [Lopez et al., 1993; Zhao and Beysens, 1995; Kalikmanov, 2013]. Due to a reduction in the number of suitable nucleation sites, water condensation on the non-wetting PFA capillary tube is much slower and sparser than the condensation on the water-wet borosilicate glass. There is no observable water vapor condensation in the benzene-water and toluene-water

systems. The low solubility and diffusivity of water in these liquids decrease the possibility of nucleation and condensation can only occur in conditions of high supersaturation [Boistelle and Astier, 1988].

Corner Flow. Corner flow rapidly transports water into the non-circular capillaries. In the absence of gravitational effects, corner flow continues until a constant radius of curvature develops along the full length of exposed corners (Figure 7.2 (b)) [Mason and Morrow, 1984, 1991, 1994].

Unbalanced Capillary Forces. Pore edges and surface roughness allow for various stable interface geometries which can cause asymmetrical interfaces at both ends, unbalanced capillary forces and flow [Morrow, 1970]. Fluid configurations evolve under this transient condition [Schluter et al., 2017]. Figure 7.5 demonstrates capillary driven flow in a benzene-water system: the radius r_2 of the meniscus on the right side is initially larger in comparison to the meniscus on the left r_1, therefore, benzene is displaced to the right. The difference in radii becomes larger, and the length of the benzene droplet rapidly decreases in the capillary. The expelled benzene forms a spherical droplet outside the tube where diffusive transport is more effective (i.e., the model in Eq. 7.3, rather than Eqs. 7.4 or 7.5).

Instabilities. Various instabilities affect the evolution of pore filling. Water collars gradually become unstable, form water blocks and split the fluid trapped in the capillary (Figure 7.6 (a)). Converging or diverging pore geometries near pore throats (e.g. the enlargement at the end of the capillary in Figure 7.6 (b)) induce snap-offs and external bubbles detach from the capillary (see related analyses in Yu and Wardlaw, 1986, and

Roof, 1970). Snap-offs change the fluid distribution, leave disconnected trapped fluids, and affect the pore filling process in porous networks [Sahloul et al., 2002].

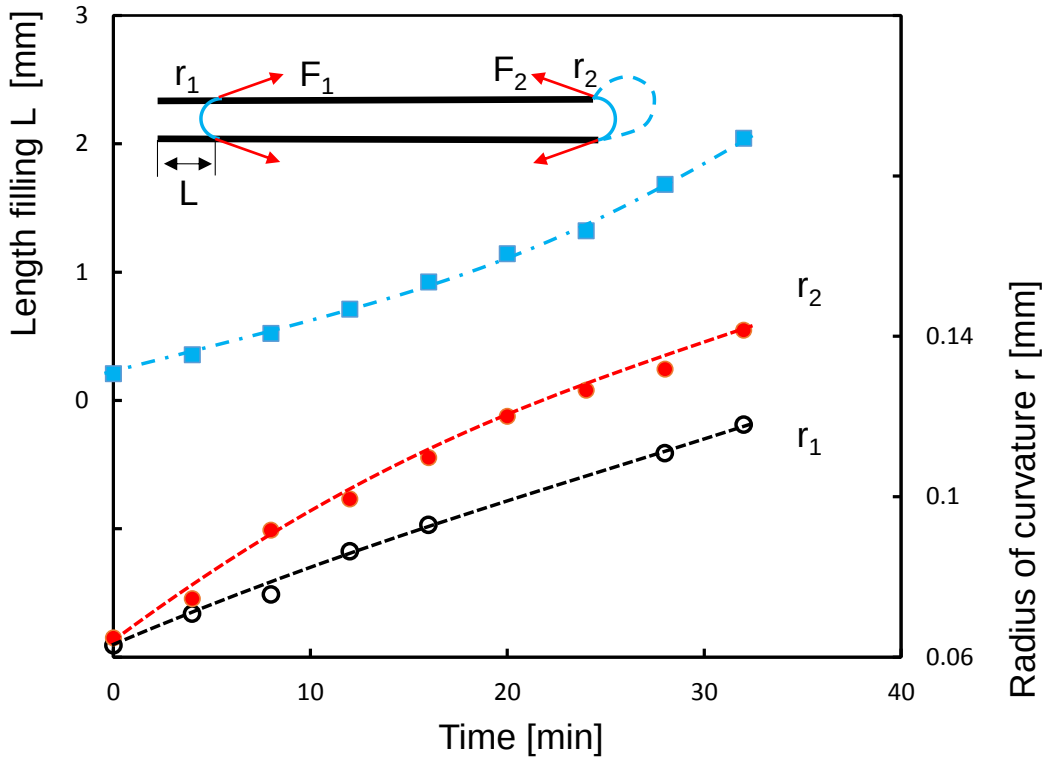

Figure 7.5. Unbalanced capillary pressure due to unequal radii of curvature $r_1<r_2$ cause capillary driven flow (Case: benzene-water system in 0.1mm capillary).

Changes in Wettability. Some systems exhibit a gradual change in the contact angle with time during pore filling. For example, this is observed in the toluene-water and benzene-water systems (Figure 7.6 (c)). Time-dependent changes in wettability may be due to: (1) the mutual dissolution of water and the trapped fluid (see images for liquid CO_2-water system in Espinoza and Santamarina, 2010), and (2) the preferential dissolution of certain species which results in the residual accumulation of less soluble components such as surfactants or long polar molecules. The change in wettability prompts different pore

fluid configurations, for example, the benzene block breaks and forms films (Figure 7.6 (c)). Changes in wettability may even initiate corner flow and facilitate diffusive transport with an increase in the interfacial area and a shorter diffusion distance [Sahloul et al., 2002].

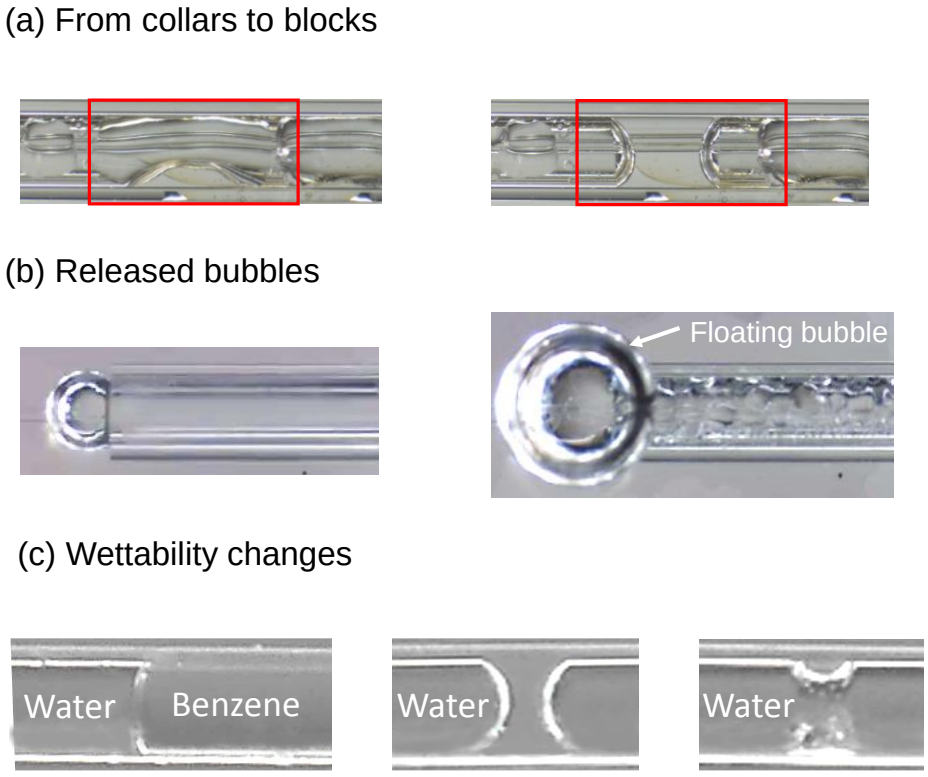

Figure 7.6. Other concurrent processes during time-dependent pore filling. (a) A block forms from a contracting water collar (Case: air-water system in 0.94mm capillary). (b) Gas is displaced from the capillary by rapid water invasion along corners, and forms a gas bubble at the end of the capillary (Case: air-water system in 0.94mm non-circular capillary with an internal rod). (c) Changes in wettability (Case: benzene-water system in 0.1mm capillary).

7.5 Implications

Results presented above highlight the inherent time-dependent nature of pore filling. Implications are relevant to natural processes and industrial applications. Two salient examples follow.

7.5.1 Reservoirs

A defending wetting phase remains connected through narrow pore corners until the later stages of desaturation when the wetting fluid becomes isolated at grain contacts (pendular regime). On the other hand, the non-wetting fluid often forms isolated droplets (snap-offs at pore throats) and patches (bypassed zones) that rest trapped in the formation. Isolated wetting and non-wetting fluids can be found in near-surface soils towards either end of wet-and-dry cycles; when buoyant oil, gas or CO_2 migrate upwards to fill a reservoir; during LNAPL/DNAPL contamination and remediation; and throughout water flooding for enhanced oil recovery. Our experiments do not reproduce reservoir P-T conditions but do capture the essential phenomena involved in the long-term evolution of saturation. For example, it is known that the amount of stored CO_2 increases with time because of capillary trapping, solubility trapping, and mineral trapping [Zhang et al., 2009; McGrail et al., 2009]. However, measurements of noble gases and carbon isotopes show that CO_2 dissolution into the formation water is the main cause of CO_2 loss from natural CO_2 reservoirs [Giffillan et al., 2009].

7.5.2 Super-hydrophobicity

Air trapping is a major contributor to the super-hydrophobic response of natural and synthetic surfaces [Quéré, 2008; Lv et al., 2017]. Typically, super-hydrophobic surfaces consist of an array of micron to sub-micron size posts where air pockets remain trapped under otherwise wetting fluids, i.e., Cassie state (Cassie and Baxter, 1944; Koch and Barthlott, 2009; Beysens, 2006; Mishra et al., 2016). This study shows that diffusion, heterogeneous condensation, and water flow along corners will gradually fill the pockets

and reduce the apparent super-hydrophobicity (Wenzel transition). Since water vapor prefers to condense on water-wet surfaces, the fabrication of super-hydrophobic surfaces consisting of hydrophobic posts with hydrophilic tops would prevent vapor condensation in air-filled pockets and extend the super-hydrophobicity effect [Varansi et al., 2009]. Alternatively, the hydrophilic surface should avoid sharp curvatures to hinder corner flow.

7.6 Conclusions

Capillarity traps fluids in porous media during immiscible fluid displacement. Short-term experimental and numerical studies fail to observe or reproduce the time-dependent filling of capillary pores. This study explored long-term pore filling using time-lapse microphotography. The photographic sequences capture a lively pore filling history where various concurrent physical phenomena coexist.

In the long-term, pore filling progresses by dissolution and diffusion through two counter-transport sequences: (1) water evaporation, transport and condensation into the fluid-filled pore, and (2) trapped fluid dissolution and diffusion out of the capillary tube. Water droplets coalesce to form water collars inside the capillary. Collars suddenly close-in to form water blocks across the pore and split the trapped fluid into segments.

Wetting fluids flow along corners in pores with non- circular geometry. Corner flow promotes pore filling and favors uniform vapor condensation.

The pinning of one interface next to a pore-end shortens the diffusion path and maintains a high constant rate of pore filling. Unpinned interfaces move gradually away

from pore ends and the diffusion length increases with time; in this case, pore filling progresses proportional to the square root of time.

The contact angle may change during pore filling because of the mutual dissolution of interacting fluids and the preferential dissolution of certain species that results in the residual accumulation of less soluble components.

Results highlight the role of time on mixed fluid conditions in porous media. Underlying long-term processes affect reservoir filling and resource recovery, contamination-and-remediation, geological CO_2 storage, sediment-atmosphere interaction, and the time-dependent response of super-hydrophobic natural or fabricated surfaces.

CHAPTER 8. GAS MIGRATION IN SOFT SEDIMENTS

8.1 Introduction

Widespread methane release from the seafloor may have a significant impact on methane flux into the atmosphere, marine environment, and energy resources. Plumes of methane bubbles occur in a variety of seafloor locations worldwide, e.g. the West Spitsbergen continental margin [Westbrook et al., 2009], the northern US Atlantic margin [Skarke et al., 2014], the sea of Marmara [Tary et al., 2012], the Gulf of Mexico [Sassen et al., 2001; Wang et al., 2016], and the Håkon Mosby Mud Volcano [Sauter et al., 2006]. Sediments in lakes, swamps, and wetlands can also generate methane [Scandella et al., 2011]. Methane can be biogenic from organic matter, thermogenic gas migrating from deep faults, or from the dissociation of methane hydrates [Andreassen et al., 2017]. Gas and oil seeps can erode the seafloor and form craters and pockmarks [Riboulot et al., 2016; Andreassen et al., 2017; Prunele et al., 2017]. Furthermore, gas migration in soft sediments is critical for the development of gas recovery from hydrates in shallow marine accumulations. In addition, the development of geological CO_2 storage requires evaluating CO_2 leakage risks [Bang et al., 2013; Lewicki et al., 2007; Cevatoglu et al., 2015].

Clearly, a detailed knowledge of gas migration mechanisms in soft sediments is critical for understanding gas release events [Dupre et al., 2015]. Gas invades into pores and creates capillary fingers in coarse-grained deep sediments. However, gas migration deforms the sediment and creates preferential pathways [Clayton and Hay, 1994; Shin and Santamarina, 2010, Clennell et al., 2000, Dai et al., 2012; Etiope and Martinelli, 2002].

A limited number of studies have directly observed gas migration in sediments. Theoretical studies assume spherical gas inclusions in shallow sediments [Wheeler, 1988, 1990; Pietruszczak and Pande, 1996]. Some experimental studies have shown other forms such as oblate spheroids, fingers, and fractures [Johnson et al., 2002; Sandnes et al., 2011]. Most of these experiments used either quasi-2D Hele-Shaw cells [Sandnes et al., 2011; Oppenheimer et al., 2015] or a transparent gel [Johnson et al., 2002; Boudreau et al., 2005]. These approaches have two limitations. First, Hele-Shaw cells impose a boundary condition and stress state which are different to what sediments experience in the 3D space. Second, unlike the elastic and cohesive gel used in previous experiments, natural sediments are frictional granular materials and have stress-dependent properties (e.g. frictional strength, Hertzian stiffness).

In this chapter, we visualize gas migration in a soft, shallow medium in 3D using a transparent and granular material which is analogous to a soft clay. Various vertical stress levels are applied to simulate gas migration in sediments at different depths.

8.2 Materials and Method

Transparent soils consist of solid grains mixed with a liquid of the same refractive index [Mannheimer and Oswald, 1993; Iskander, 2010]. Due to their high transparency and granular nature, transparent soils have been used to study pile penetration [Gill and Lehane, 2001; Ni et al., 2010], shallow foundations [Liu and Iskander, 2010], multiphase flow [Serrano et al., 2011; Krummel et al., 2013], and tunneling (Ahmed and Iskander, 2012).

8.2.1 Transparent Soil

The transparent soil used in this study consists of fumed silica and blended oil (similar to Gill and Lehane, 2001). Fumed silica (from Sigma-Aldrich) comprises fine particles with a size of around 30 nm. These particles form aggregates which are in the order of several micrometers. The fumed silica has a density of 2.2 g/cm^3 and specific surface of 200 m^2/g measured by the methylene blue absorption method [Santamarina et al., 2002]. The pore fluid used to match the refractive index of fumed silica mixes two baby oils (Mom to Mom Baby Oil and Johnson's Baby Oil) at 1:1 by volume. Viscosities of the two baby oils are 15 and 23 mPa·s, respectively. The density of the mixed oil is 0.825 g/mL.

We use a three-step procedure to make the transparent soil. First, we mix fumed silica with the blended oil at 3 g : 40 mL ratio to form a gassy slurry. This ratio ensures a high silica content while retaining liquidity. Then, the slurry is put in a vacuum for a few hours to remove all air bubbles inside the slurry; after de-airing, the slurry becomes transparent. Finally, the transparent slurry is poured into a consolidometer designed for this study and consolidated to a desired effective stress level.

The geotechnical properties of the transparent soil are characterized by consolidation tests, and shear wave measurements with bender elements [Lee and Santamarina, 2004]. The maximum consolidation stress applied to the specimen is 44 kPa. Table 8.1 summarizes the results. There are no observations of shear waves at effective stress levels lower than 4 kPa. The measured α, β, and C_c values agree well with relationships described in Cha et al. (2014) which uses a large database of real soil samples.

The transparent soil falls into the clay soil region in this database. Overall, the transparent soil can be an accurate analogue to soft sediments in terms of both geotechnical properties and particulate nature.

Table 8.1. Transparent soil: mechanical properties.

Property	Value	Note
Particle size/ Aggregate size	~30 nm/ ~1 μm	From SEM image of fumed silica powder
Specific surface	200 m^2/g	Methylene blue method
Density	0.874 g/cm^3	Slurry
	0.912 g/cm^3	At σ'=44 kPa
Void ratio	17.6	At σ'=44 kPa
Hydraulic conductivity	2.2×10^{-7} cm/s	At σ'=44 kPa, from consolidation tests
Coefficient of consolidation	~1.3×10^{-3} cm^2/s	From consolidation tests
Compression index	~3.3	From consolidation tests
Small-strain shear stiffness	0.3 MPa	At σ'=44 kPa , from shear wave velocity
α factor	3.34 m/s	From shear wave velocity
β factor	0.543	From shear wave velocity
Peak and ultimate friction angle	37° and 31°	Gill and Lehane (2001)

8.2.2 Experimental Setup and Procedure

The design of the experimental setup (Figure 8.1 (a)) fulfills the following functions: applying vertical stress, consolidation and drainage, gas injection, and recording the gas migration process. The experimental cell has a square shape Plexiglas tube as the wall (width 50.8 mm; wall thickness 3.2 mm) and an aluminum bottom plate. A pneumatic cylinder which pushes a permeable piston applies the load. Excess pore fluid drains from both the top and bottom of the specimen. An LVDT monitors the vertical displacement of the specimen. A stainless steel needle for gas injection is fixed at the center of the bottom plate and connects to a pressure transducer and syringe. The needle is cylindrical and has

an ID of 0.83 mm and OD of 1.27 mm. Two cameras (Sony) are set with same shooting settings and placed at an identical distance from the cell on the central axes. Two LED panels serve as background for illumination.

To prevent clogging of the injection system due to the consolidation process, we test different needle configurations. In the first configuration, we cover the needle tip with paper which prevents particle entry but allows gas flow. In the second configuration, a metal wire inserted inside the needle during the consolidation process prevents particle entry. The metal wire is then removed and a stopper is placed at the end before the injection starts (Figure 8.1 (b)). The majority of the tests use the second configuration.

Cell dimensions minimize boundary effects while maintaining high-quality imaging conditions. A spherical cavity has less than a 4% effect on the stress field outside 3 times the radius of the cavity [Yu, 2000]. Therefore, the boundary effect is negligible for a gas bubble with a radius smaller than 1 cm. The friction coefficient between the wall and the specimen is measured independently and is approximately 0.3. Estimates of the stress state at the tip of the injection needle consider the wall friction effect.

A typical experiment starts with a thorough examination and test of the injection system without the presence of transparent soil. The tip of the needle is plugged. Gas pressure builds up during the injection and becomes constant when the injection stops, which indicates negligible leakage. A sudden drop in pressure which immediately follows the fast opening of the tip suggests that the injection system has no plug and allows unimpeded flow.

Following a successful injection system test, the transparent slurry is poured into the cell and consolidated to a desired effective stress level. The gas injection starts after the consolidation process when the LVDT reading becomes constant. A metal wire cleans the inside of the needle to prevent clogging. A syringe pump injects gas at a constant rate (2 mL/hr). Two cameras record the entire injection process from two orthogonal directions at a frequency of 1 frame/ 10 second. A pressure transducer (Omega) measures the gas pressure.

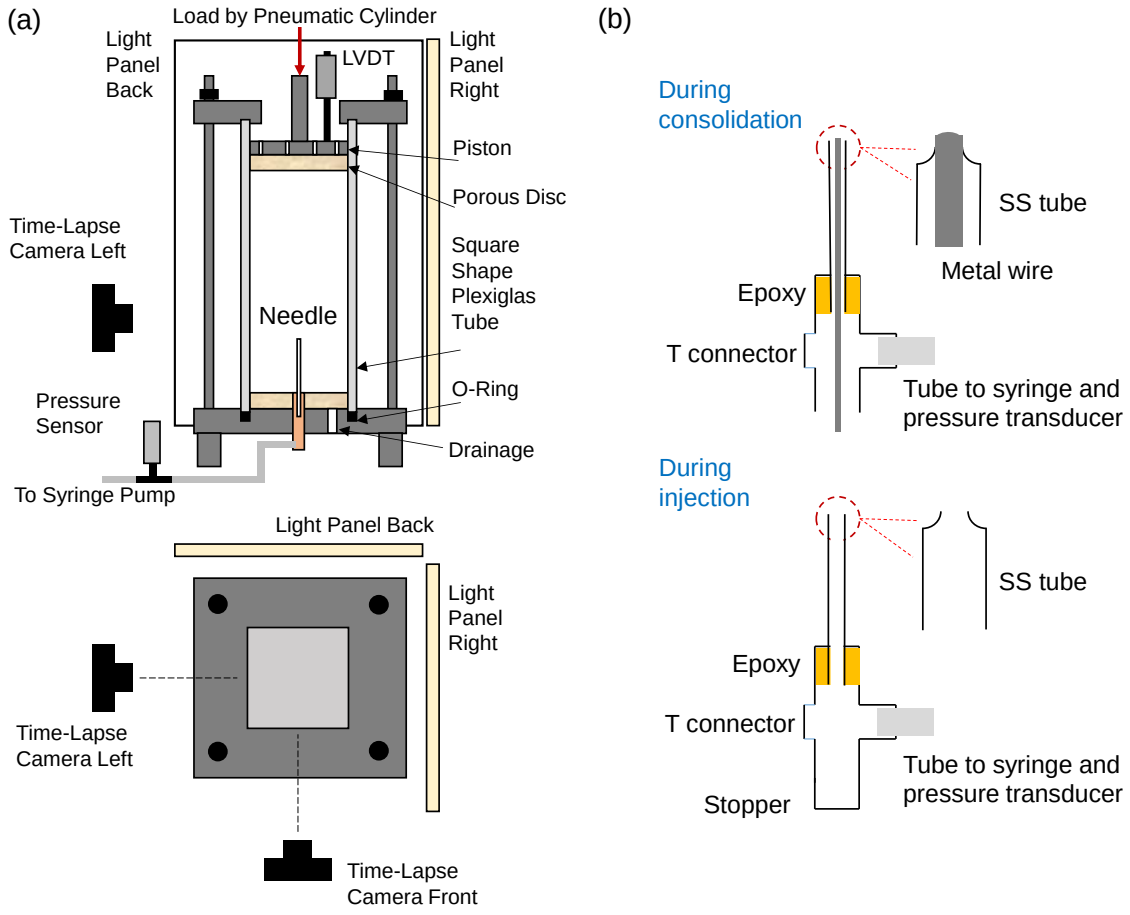

Figure 8.1. (a) Experimental Setup. (b) Detail of the gas injection needle.

8.3 Results

8.3.1 Gas Inclusion Growth Patterns and Pressure Signatures

We consolidate the transparent soil to vertical effective stress levels that range from 0.15 kPa to 44 kPa. These stress levels correspond to shallow marine sediments at depths ranging from less than 10 cm to more than 10 m. Figure 8.2 shows typical results at σ_v'=0.15 kPa, 3.8 kPa, and 24 kPa. The volume of the gas inclusion (blue line) in the transparent soil is calculated based on the pressure-volume relationship (Ideal Gas Law):

$$P \cdot \left(V_{ini} - V_{inj} + V_{gi}\right) = C \tag{8.1}$$

where C is a constant which depends on temperature; V_{ini} is the initial volume of gas in the injection system; V_{inj} is the injected volume which is the product of the injection rate and injection time; and V_{gi} is the volume of the gas inclusion in the transparent soil.

Gas migrates as bubbles at σ_v'=0.15 kPa. Bubbles are rarely spherical due to the resistance from sediments. These bubbles can float, interact and merge. The pressure signature shows a saw shape with sudden drops which indicate gas bubble inflation. Note that individual bubbles move along the same trajectory created by the leading bubble.

The growth of the gas inclusion transitions from a bubble to a fracture at σ_v'=3.8 kPa. In the beginning, the gas inclusion grows as a cavity (point a). The gas pressure drops sharply as the cavity increases to a finite volume. Then the cavity expands with a saw-shape pressure and step-shape volume signature. The pressure increase corresponds with the elastic deformation of the soil, which causes little volume change. When the pressure reaches a critical value, the gas inclusion suddenly expands and the pressure drops.

Gradually, the cavity develops corners and edges. Fractures then initiate from these locations (point b). Finally, the gas inclusion grows as a thin fracture (point c).

At higher effective stresses (e.g. σ_v'=24 kPa), gas migrates by creating fractures without experiencing the cavity expansion stage. The pressure plateaus after the fracture initiates. Note that the pressure signature is also a saw-shape; however, the teeth are fine, and each pressure drop signifies a step growth in the volume of the fracture. As the effective stress becomes even higher (e.g. σ_v'=44 kPa), the gas pressure continuously increases during fracture growth, unlike the saw shape described earlier. This is because the gas injection rate is higher than the growth rate of the gas inclusion.

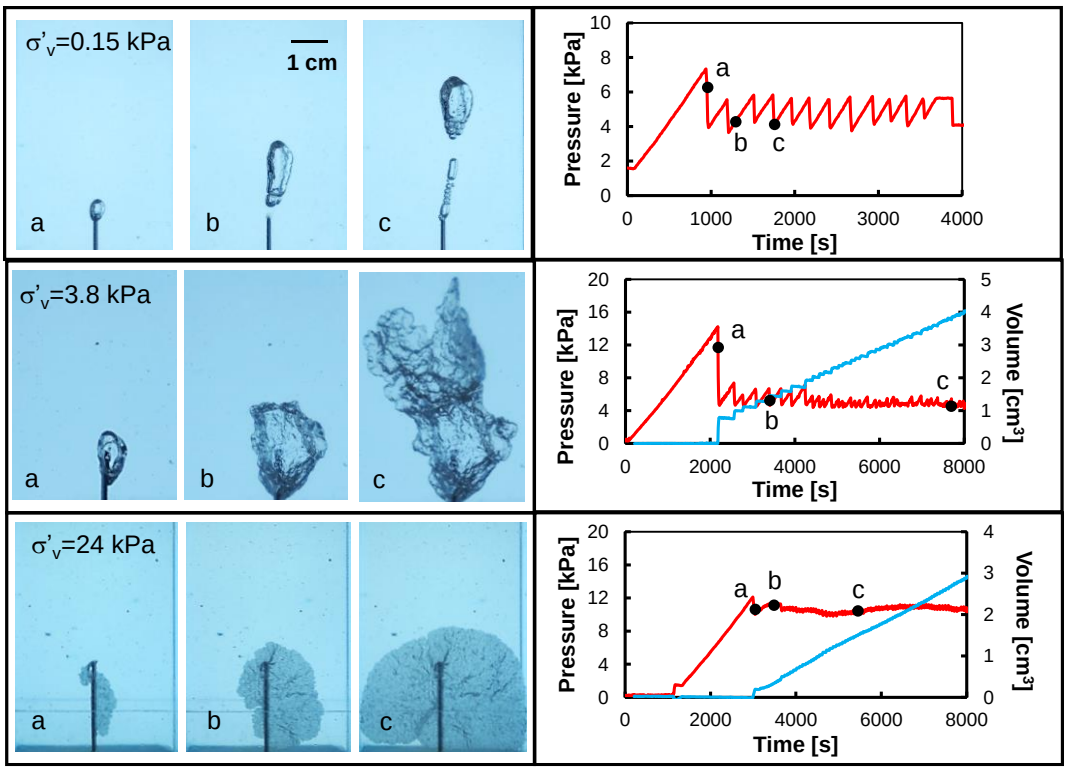

Figure 8.2. Typical examples of gas invasion evolution and pressure signatures. Plots show gas pressure (red line) and gas inclusion volume (blue line) signatures.

8.3.2 Cyclic Loading (Unloading and Reloading)

Additional experiments examine the effect of cyclic loading on gas migration to simulate tidal cycles. Cyclic loading (unloading and reloading cycles) involve reducing and increasing the vertical stress after the injection process. Figure 8.3 shows an example of a sample unloaded and reloaded from 14 kPa. During unloading, the gas expands and advances the fracture. It migrates upwards, reaches the top porous disk, and leaks gas into the atmosphere. During reloading, the gas inclusion partially closes and the leakage pathway temporarily shuts down. It then reopens during unloading.

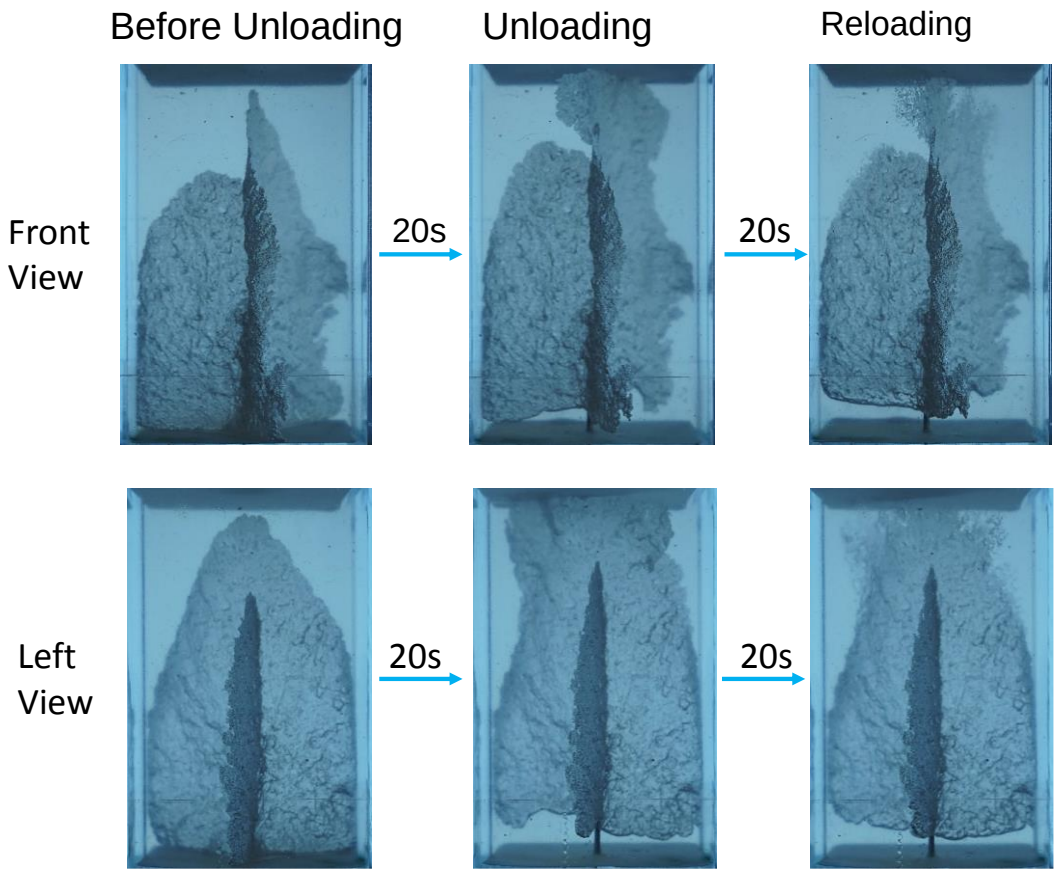

Figure 8.3. Unloading and reloading of the vertical stress. Note: the effective stress was 14 kPa before unloading.

8.3.3 Memory Effect

Injection sequences exhibit clear memory effects. After the first injection, the gas inclusion gradually closes, probably as a result of gas adsorption or diffusion into the medium. This process takes days. For the example shown in Figure 8.4, the first injection occurs at an effective stress of 4 kPa. The second injection takes place at the same effective stress 4 days after the first injection when the gas inclusion completely disappears. Note the soil was subjected to cyclic loading before the secondary injection. During the second injection, gas invades the sediment at a lower injection pressure and follows a pathway very similar to the pathway created by the first injection. The similarities are not only in overall geometry, but also in the fine details. For example, both have the same broken-curved geometry next to the needle (Front view), and vein patterns (Side view). Similarly, tests at low effective stress levels show that the individual bubbles move along the same trajectory created by the leading bubble. Memory remains in the sediment even when additional gas injections are separated by long inactive periods.

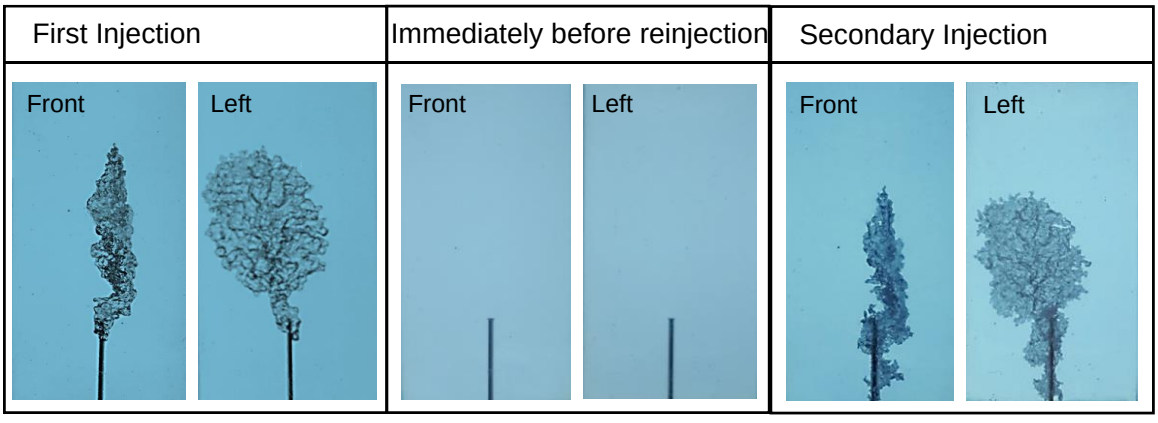

Figure 8.4. Memory effect. After the first injection, the sample experiences loading (to 15 kPa) and unloading (back to 4 kPa). The secondary injection occurs 4 days after the first injection.

8.4 Analyses and Discussion

8.4.1 Gas Inclusion Morphology in Soft Sediments

In previous studies, gas inclusions in shallow sediments were assumed to be spheres in conceptual models [Wheeler, 1988, 1990; Pietruszczak and Pande, 1996], observed as oblate spheroids in gelatin [Johnson et al., 2002; Boudreau et al., 2005], viscous fingers in 2D Hele-Shaw cells [Sandnes et al., 2011; Oppenheimer et al., 2015], and measured by CT scans [Barry et al., 2010; Abegg et al., 1997; Anderson et al., 1998]. In this study, we directly observe gas migration in a transparent soil which is particulate and analogous to natural soft clay.

Our results reveal that morphologies of gas inclusions in sediments depend on the effective stress, which results from effective stress-dependent properties of particulate materials. Gas migrates as tubes and bubbles at very low effective stress. Cavities deviate from the smooth spherical geometry of bubbles in water and gain a faceted geometry as the role of the surface tension vanishes as a shape-controlling parameter. A transition from cavity expansion to opening-mode "fractures" is observed at an effective stress of around 4 kPa. At higher effective stress, gas migrates by developing thin fractures in sediments. Gas can invade into pores if the effective stress is too high and prevents any sediment deformation.

Figure 8.5 displays the influence of sediment properties on the evolving morphology of the gaseous body. Shear stiffness is calculated from shear wave measurements, and image analysis estimates the average thickness of the gas inclusion. In most cases, the gas inclusion can be treated as one or multiple thin planes with a vertical

axis. Based on this assumption, we obtain the area of the plane S from images taken in two orthogonal directions (theorem for orthogonal projections of plane):

$$S = \sqrt{S_L^2 + S_F^2} \tag{8.2}$$

where S_L and S_F are areas of the orthogonal projections of the plane. We do not consider the effect of image distortion in first-order calculations. The average thickness is then calculated based on the volume of the gas inclusion and the area of the plane. The calculated thickness to width ratio for the different gaseous bodies decreases as the sediment stiffness increases. For an open-mode fracture, the correlation between the average thickness and shear stiffness shows the relationship thickness $\propto G^{-1}$.

These results contrast with observations in quasi-2D Hele-Shaw cells [Sandnes et al., 2011; Oppenheimer et al., 2015] and in transparent gels [Johnson et al., 2002]. Sandnes et al. (2011) observed a transition of deformation patterns from fingers to bubbles to fractures with increases in granular filling friction. However, the quasi-2D boundary confinement may significantly affect characteristics of these patterns (see examples in Saintyves et al., 2013). The gelatin used in Johnson et al. (2002) and Boudreau et al. (2005) is elastic and cohesive. The observed oblate spheroidal bubbles were explained by linear elastic fracture mechanics [Barry et al., 2010]. Their results omit the particulate nature of sediments and therefore are unable to demonstrate stress-dependent patterns. In summary, this study and previous studies suggest that confinement, stress state, and material properties are all key factors which control the deformation morphology of gas in sediments.

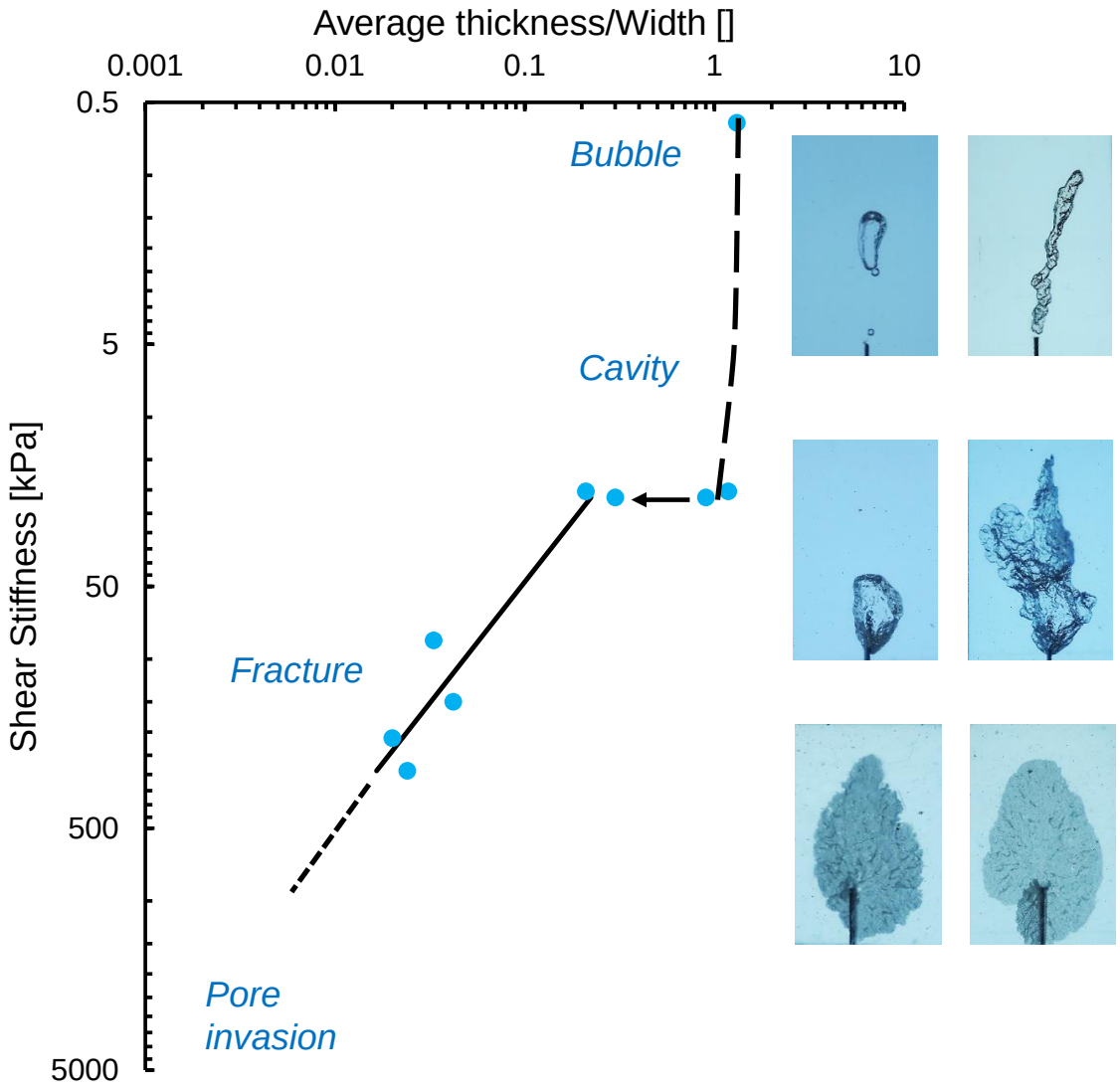

Figure 8.5. Gas invasion morphology in sediments: the effect of effective stress and stiffness. Images show injected gas in transparent soil at different vertical effective stress conditions. The plot shows the average thickness to width ratio as a function of sediment shear stiffness. A transition from cavity expansion to fracture takes place as the shear stiffness increases. The solid line shows the reciprocal relationship.

8.4.2 Cavity to Fracture Transition

Different morphologies of gas inclusions in sediments relate to the failure modes of particulate materials at different states. Experiments have shown that failure modes of particulate materials include fracture, shear rupture and plastic yield, which depend on the stress state, liquidity, and preconsolidation [Thusyanthan et al., 2007; Aluko and Seig, 2000; Hatibu and Hettiaratchi, 1993; Hettiaratchi and Callaghan, 1980]. Sediment failure as fractures or shear rupture at low confinement and low liquidity can create cracks or large pores. This also creates new surfaces where gas/liquid exerts pressure. However, at high confinement and high liquidity, plastic yield is preferred and does not create any discontinuities in sediments [Schofield, 1980].

Our results are consistent with these observations. Additional experiments include gas injection tests on samples consolidated at high stress and then unloaded to low confinement levels. Fracture is the only mode of deformation in these cases where the confinement and the liquidity are both low.

8.4.3 Fracture Growth Process

In terms of the growth process, our results also contrast with experiments that use Hele-Shaw cells and gels. Figure 8.6 (a) plots over the boundary of the fracture front extracted from continuous images. Unlike the smooth surface of gas bubbles in gelatin, the boundary between the gas and transparent soil is rough and full of irregularities. The growth front does not propagate as a continuous line, but is highly localized (see also Figures 8.6 (b) and 8.6 (c)). Fractures do not grow as a single front but rather as intermittent bursts that result in fingers. These fingers eventually merge into a circular front as the

finger extension is approximately the same size as its width. The injection fluid affects the nature of these fingers, i.e. there is more stick-slip in the gas injection.

The growth features in this study also differ from experiments in Hele-Shaw cells [Huang et al., 2011; Oppenheimer et al., 2015]. Fractures propagate and form viscous fingering-like patterns in quasi-2D conditions. By contrast, in the 3D condition, fractures propagate along the plane and have a rough front (see also Murdoch, 1993a). Unlike the viscous fingering interfacial instabilities in 2D conditions, the fracture front in 3D conditions is irregular but is independently stable due to the stress concentration mechanism. Note that instabilities in Hele-Shaw cells can also be induced by the friction between the medium in the cell and the wall (Saintyves et al., 2013), thus distorting the observations.

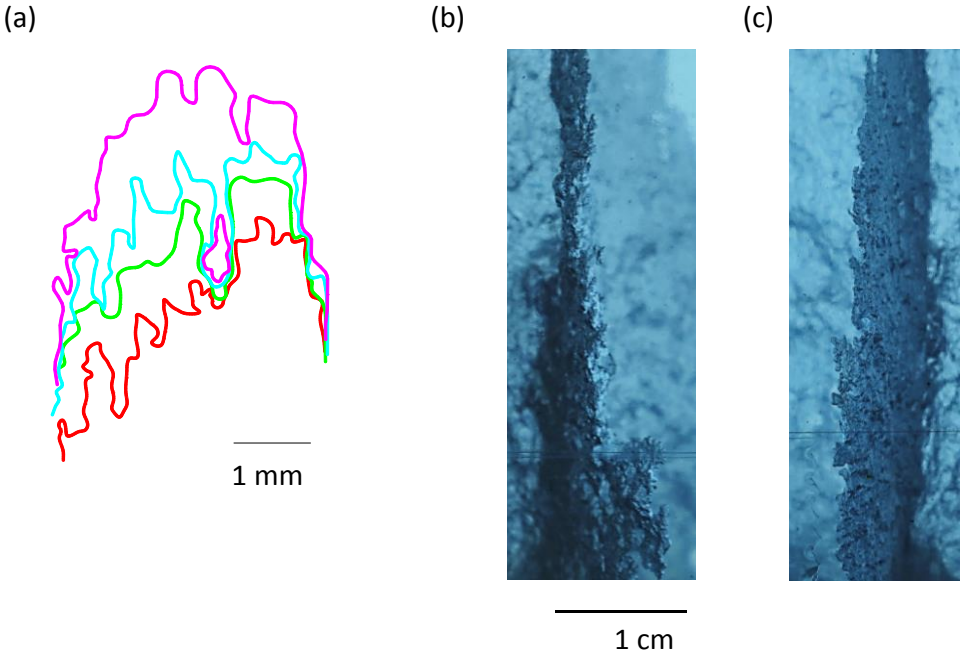

Figure 8.6. Fracture growth. (a) Front view. (b) and (c) Side views of the fracture propagation fronts.

8.4.4 Gas Injection Pressure

The critical injection pressure which induces sediment failure is critical to a wide variety of engineering applications. These include directional drilling [Xia and Moore, 2006], dam safety [Yanagisawa and Panah, 1994], hydraulic conductivity measurements [Bjerrum et al., 1972], in situ remediation [Alfaro and Wong, 2001], and grouting [Marchi et al., 2013]. Table 8.2 summarizes the major models that predict critical injection pressures (please refer to Alfaro and Wong, 2001; Marchi et al., 2013 and Keulen, 2001). Most models assume tensile strength, fracture toughness, and apply linear elastic fracture mechanics.

Our results show various modes of deformations and a transition from a cavity to a fracture-like failure at different effective stress levels. Existing models do not consider failure modes of particulate materials and the effects of stress, liquidity, and preconsolidation. The assumption that sediments have elastic and cohesive properties, and the use of linear elastic fracture mechanics hinder the development of a complete model because they do not account for the particulate nature of sediments.

For a cavity expansion solution, the undrained shear strength c_u should be calculated based on critical state soil mechanics (Wood, 1990, pp181-pp184). The undrained shear strength calculated from critical state soil mechanics is (normal consolidated) [Wood, 1990; Cao et al., 2001]:

$$c_u = \frac{Mp_i'}{2}\left(\frac{n_p}{2}\right)^{\Lambda} \tag{8.3}$$

where M is the slope of the critical state line in the p'-q plane, n_p is the isotropic overconsolidation ratio, and Λ is the plastic volumetric strain ratio. The Tresca criterion or critical state can calculate the ultimate pressure [Cao et al., 2001; Carter et al., 1986, Yu, 2013]. The pressure p_{lim} for a spherical cavity expansion is [Yu, 2013; Carter et al., 1986; Cao et al., 2001]:

$$p_{\lim} = \frac{4c_u}{3}\left[1 + \ln\left(\frac{G}{c_u}\right)\right] + p_0 \tag{8.4}$$

where G is the shear stiffness of the soil.

Fractures propagate perpendicular to the direction of minimum stress. The pressure is linear to the minimum stress.

Figure 8.7 compares trends with experimental data. The injection pressure required for gas inclusion growth is plotted as a function of the vertical effective stress. Blue dots are data for cavity expansion cases, and red dots for open-mode opening cases. Figure 8.2 shows a remarkable peak pressure in tests at low effective stress which corresponds with cavity expansion. However, there is minimal difference between the peak pressure and subsequent pressures in tests with high effective stress. The pressure required for fracture growth follows the K_0 line, while the pressure required for cavity expansion is much higher and follows the cavity expansion solution.

Table 8.2. Models for internal pressure-induced failure in sediments (cylindrical hole cases).

Category	Equation	Description	Reference
Cavity Expansion	$P_{ci} = \sigma_0 + s_u\left[1 + \ln\left(\frac{G}{s_u}\right)\right]$	Limit pressure of cavity expansion theory; cohesive soil	Wheeler (1990); Vesic (1972); Carter et al. (1986)
	$P_{ci} = (\sigma'_f + c\cdot\cot\varphi)\cdot\left[\left(\frac{r_0}{r_p}\right)^2 + Q\right]^{\frac{-\sin\varphi}{1+\sin\varphi}} - c\cdot\cot\varphi + u$ $\sigma'_f = \sigma'_0(1+\sin\varphi) + c\cos\varphi$ $Q = (\sigma'_0\sin\varphi + c\cos\varphi)/G$	Cavity expansion theory, Mohr-Coulomb criterion	Keulen (2001)
	$\varepsilon_{\max} = \frac{\sigma_0 + a}{2\mu}\cdot\frac{1-m}{1+m}\cdot\left(\frac{1+m}{2}\cdot\frac{P_{ci}+a}{\sigma_0+a}\right)^{\frac{k+1}{1-m}}$ $a = c\cot\varphi; m = (1-\sin\varphi)/1+\sin\varphi; k = (1-\sin\psi)/(1+\sin\psi)$	Cavity expansion theory, maximum strain criterion	Keulen (2001)
Linear Elastic Fracture Mechanics	$P_{ci} = \sigma_0 + \frac{CK_{IC}}{\sqrt{\pi a}}$	Linear elastic fracture mechanics	Murdoch (1993); Johnson et al. (2002); Barry et al. (2010); Jain and Juanes (2009)
Elastic Theory	$P_{ci} = 2\sigma_0 - u_0 + \sigma'_t$	Elasticity, tensile failure criterion	Marchi et al. (2013)
	$P_{ci} = \sigma_0 + s_u$	Elasticity, shear failure, unconsolidated undrained shear strength	Yanagisawa and Panah (1994)
Empirical formula	$P_{ci} = m\sigma_0 + \sigma_{ta}$	Empirical formula, tensile failure	Jaworski et al. (1981)
Nonlinear/ Pore Pressure Change	$P_{ci} = \sigma_0 + \Delta u$ Δu is calculated	Tensile failure	Anderson et al,. (1994)

Note: σ_0' confining stress; s_u undrained shear strength; G shear modulus; P_{ci} critical pressure; φ friction angle; ψ dilation angle; c cohesion of soil; u pore pressure; σ_t' tensile strength; K_{IC} fracture toughness; a length of crack; C shape factor; m empirical factor.

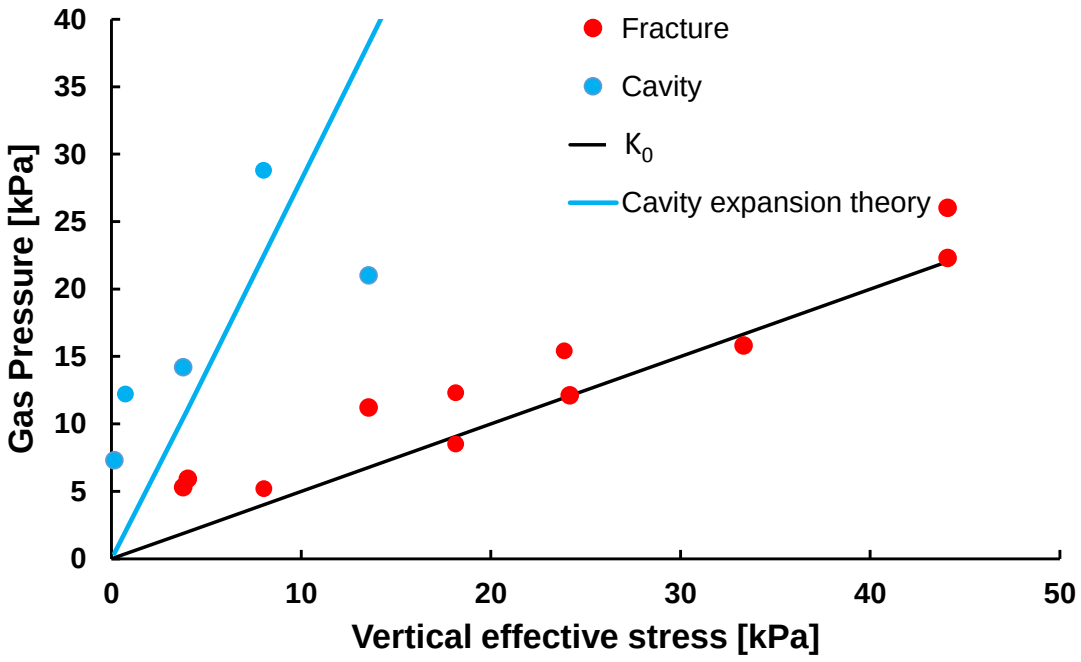

Figure 8.7. Gas injection pressure vs. vertical effective stress. Red dots represent the pressure required for open-mode fracture growth. Blue dots represent pressures required for cavity expansion (peak values). The solid black line is the K_0 line. The solid blue line is the calculation based on cavity expansion theory.

8.4.5 Cyclic Loading Effect

Ocean bottom pressures are not constant but vary with time due to tidal fluctuations or other movements [Jeng, 2003]. This pressure fluctuation affects the effective stress and pore water pressure which may influence the movement of the gas body in sediments. The gas inclusion can gradually move up during cyclic loading [Wheeler, 1990].

Figure 8.8 analyzes the evolution of total stress, effective stress, pore water pressure and pressure differences during unloading and reloading. During unloading, the pressure difference between the gas and pore fluid increases and the effective stress decreases. This causes the gas body to move up and create further fractures in the sediment. Gas release

can occur during this process. However, the pressure difference decreases and the effective stress increases during reloading. Therefore, the gas body halts and contracts.

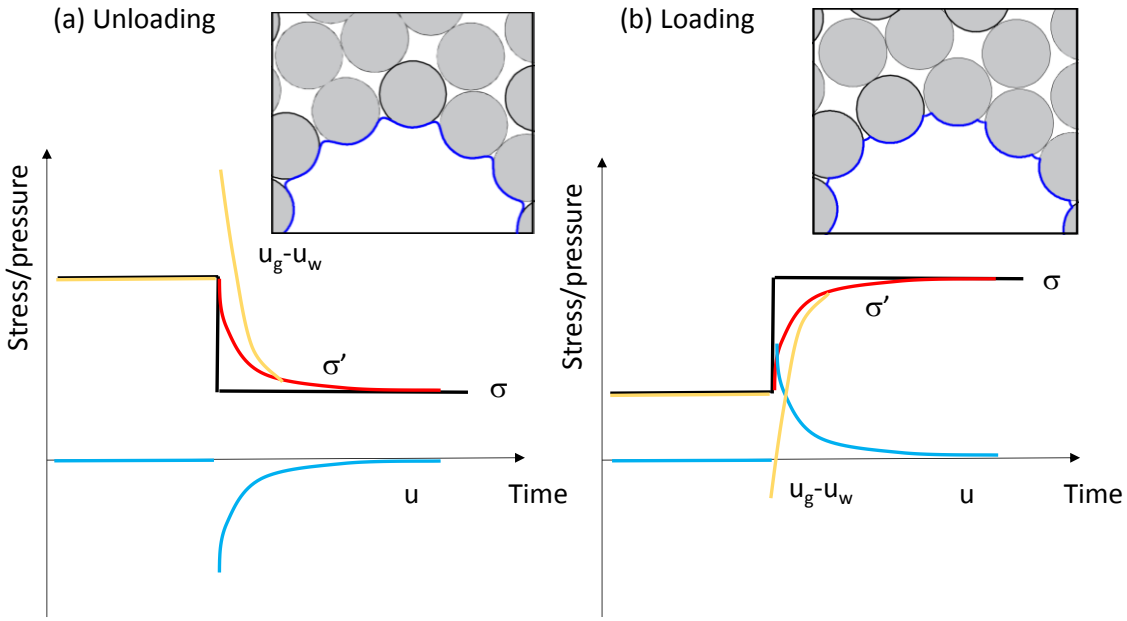

Figure 8.8. Evolution of the total stress, effective stress, pore pressure and pressure difference between the invading gas and the host pore fluid. During unloading, the pore pressure decreases and the pressure difference between the gas and pore fluid exceeds the effective stress, bubbles expand and the internal pressure decreases. Eventually the pressure difference drops below the effective stress and expansion stops. During loading, pore pressures increase and the pressure difference between the invading gas and the host pore fluid decreases below the effective stress, bubbles contract and the internal pressure increases. Eventually bubbles stop contracting.

8.4.6 Memory Effect

Sediments exhibit memory effects. One possible reason is the break of any historical bonding due to diagenesis during the first injection, with less pressure required for the second injection. The deformation process during the first injection and the relaxation during the "fracture" healing cause irreversible changes of the horizontal effective stress and void ratio distribution (Figure 8.9). This redistribution of horizontal effective stress and void ratio creates a zone with lower horizontal effective stress and a

higher void ratio. Therefore, new fractures nucleate at locations of previous "fractures" with less effort.

The presence of discontinuities in sediments alters the original stress and property fields and creates a relaxation zone when discontinuities close. Evidence can be found in the effect of contracting tunnels or wellbores on soils [Cheng et al., 2007; Yu and Rose, 1999]; the evolution of horizontal effective stress during mineral dissolution [Shin et al., 2008], and the formation of polygonal faults [Shin et al., 2010]. This memory effect also suggests burrows and plant roots can serve as preferential pathways for gas leakage [Oades, 1993]. These potential discontinuities can facilitate gas migration in sediments [Olivella and Alonso, 2008; Etiope and Martinelli, 2002]. Previously disturbed or fractured pathways can remain in the sediment even when there are prolonged inactive periods.

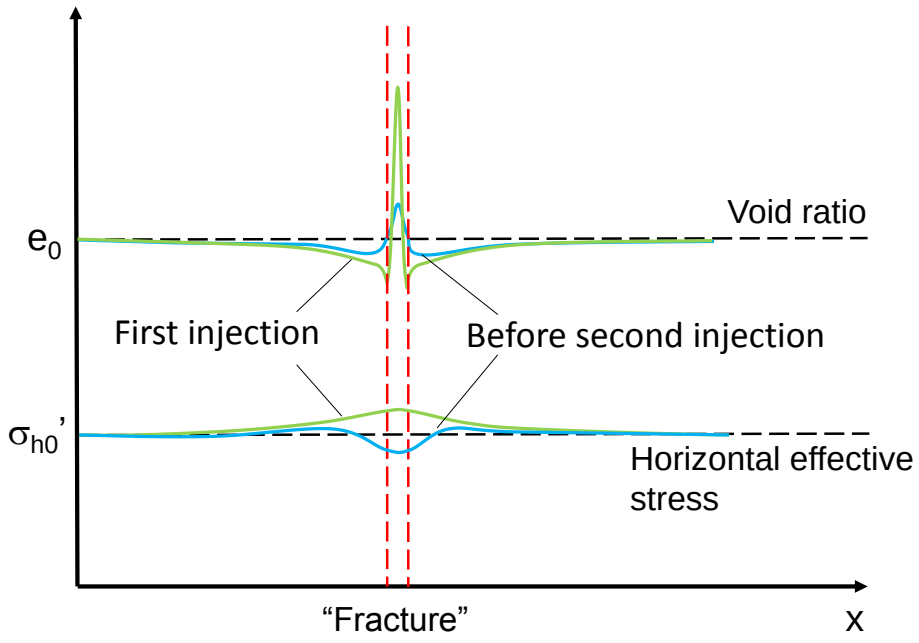

Figure 8.9. Proposed mechanism for memory effect: compression during gas injection and contraction during "fracture" closure causes the redistribution of the void ratio and horizontal effective stress.

8.5 Conclusions

We visualize gas migration in 3D using a transparent soil that allows direct observation of gas invasion. The transparent soil resembles soft sediments in both geotechnical properties and granular nature. Image analysis and gas injection pressure measurements provide quantitative information for mechanistic analyses. The main conclusions follow:

- The morphology of the gas body in sediments varies at different effective stress conditions. Gas tubes and bubbles form at very low effective stress, while fracture-like openings form under high effective stress. In other words, there is a transition from cavity expansion to fracture-like invasion as the effective stress increases.
- Fractures do not grow as a single front but are highly localized. The fracture plane thickness is inversely proportional to the sediment shear stiffness.
- The fracture grows perpendicular to the minimum principal stress. The initial pressure peak related to cavity expansion has a higher value. This transition from cavity expansion to open-mode discontinuity is controlled by the sediment mechanical behavior.
- The gas body can migrate upwards in sediments driven by buoyancy and internal pressure. Fluctuations in ocean bottom pressures can promote this movement.
- Closed discontinuities can re-open at a lower pressure and with a similar configuration as additional gas invades the formation. The memory of preferential pathways can remain even when gas flow ceases for prolonged periods.

CHAPTER 9. CONCLUSIONS

This study aims to advance the fundamental understanding of multi-phase flow in porous media for applications in the area of energy and the environment. This research investigates key capillary phenomena in porous media, which include: the effect of pore geometry on multi-phase flow, Haines jumps, multi-phase flow with particle-coated interfaces, gas-sediment interactions, and long-term pore filling. The main conclusions for each chapter are presented separately:

Chapter 2: An Overview of Capillary Phenomena in Porous Media

- Surface tension varies with pressure, temperature, solute concentration, and surfactant concentration; on the other hand, the contact angle responds to interfacial tensions, surface topography, invasion velocity, and chemical interactions.
- Interfaces are not isolated but interact through the fluid pressure and respond to external fields. Jumps, snap-offs and percolating wetting liquids along edges and crevices are ubiquitous in real, non-cylindrical porous networks.
- The saturation-pressure characteristic curve is affected by the saturation history, flow rate, the mechanical response of the porous medium, and time-dependent reactive and diffusive processes. In addition, there are salient differences between unsaturation by internal gas nucleation and gas invasion.
- Capillary forces add to other skeletal forces in the porous medium and can generate open-mode discontinuities when the capillary entry pressure is high relative to the effective stress.

Chapter 3: Capillary Pressure across a Pore Constriction in the Presence of Surfactants

- The capillary pressure is a function of the contact angle, surface tension and the evolving pore geometry as the fluid interface traverses the pore constriction in advancing and receding tests.
- Distinct instabilities including jumps and snap-offs are observed; pore-scale instabilities alter the measured pressure-time signatures.
- When aqueous surfactant solutions are involved, measured capillary pressures cannot be readily anticipated from static-bulk fluid measurements due to the transient surfactant-pore geometry interaction.
- Plugs form when residual annular wetting films/droplets left behind after a jump contract back towards the pore throat. Plugs split the non-wetting fluid into isolated globules and add resistance against fluid flow.

Chapter 4: Mechanisms of Haines Jumps

- Haines jumps occur as a result of interactions between the meniscus and the system. Three mechanisms of interactions are entrapped gas bubbles, deformable solid matrix, and interconnected menisci.
- Proposed models which compute the pressure-volume response of the system predict the occurrence of Haines jumps. Experiments in capillary pore models and micro-chips verify proposed models.
- Results suggest that experiments in micro-chips should be carefully conducted and consider interactions of the fluid with entrapped gas bubbles and tubes. Findings

also indicate that the system response can alter by changing the contact angle or mechanical properties of the interface.

Chapter 5: The Mechanical Response of Nanoparticle-coated Interfaces

- The particle-coated interface undergoes a transition from fluid-like to solid-like during shrinkage. Particles are packed from a loose packing to a dense packing. Further compression of the closely packed particles results in interface buckling.
- The mechanical response of the interface is time-dependent due to the adsorption kinetics of nanoparticles to the interface.
- The particle-coated interface exhibits an asymmetric, curvature-dependent mechanical behavior. Analyses of the stability of particle chains suggest that the particle-interface interactions contribute to this asymmetric behavior.

Chapter 6: Fingering Patterns Induced by Nanoparticle-coated Interfaces

- Experiments in capillary pore models and microfluidic channels demonstrate the break of the nanoparticle-coated interface and the pinning of the interface on the microfluidic channel surface.
- Mushroom-like instabilities occur during the displacement of a less viscous fluid by a more viscous fluid in a radial Hele-Shaw cell. This result deviates from classical viscous fingering theory which predicts a stable displacement.
- The mushroom-like instability results from the formation of a nanoparticle-coated interface during displacement. The critical radius where the instabilities occur depends on the flow rate because nanoparticle adsorption on the interface is time dependent. The lower the flow rate, the smaller the critical radius.

Chapter 7: Time-dependent Pore Filling

- Results show very dynamic processes and coexisting events as the trapped fluid volume decreases with time. Dissolution and diffusion play a central role. Observations indicate preferential transport of the wetting liquid along corners, vapor condensation, capillary flow induced by asymmetrical interfaces, and interface pinning that defines the diffusion length.
- The rate of pore filling is diffusion-controlled in this experiment; diffusive transport occurs at a constant rate for pinned interfaces, and is proportional to $t^{1/2}$ for free interfaces where the diffusion length increases with time.

Chapter 8: Gas Migration in Soft Sediments

- The morphology of the gas body in sediments varies at different effective stress conditions. Tubes and bubbles can form at very low effective stress levels, while fracture-like openings can easily form under high effective stress levels. A transition from cavity expansion to fracture-like openings can occur as the effective stress increases.
- The gas pressure required to keep the fracture growing follows the minimum principle stress. The peak pressure related to cavity expansion has a higher value. This transition from cavity expansion to open-mode discontinuity is controlled by the mechanical behavior and failure modes of sediments.
- Cyclic loading promotes gas migration and escape through sediments. The memory effect of sediments suggest that previously disturbed or fractured pathways can remain in the sediment even when there are prolonged inactive periods.

This study has broad implications for multiphase flow issues related to energy and the environment. Results in Chapter 3 highlight the inherent instabilities in non-uniform pore geometry. These instabilities result in fluid trapping during fluid displacement. Proposed mechanisms in Chapter 4 hint to the possibility of controlling these instabilities to create stable fluid displacement and improve displacement efficiency. Future work can investigate the relationship between pore-scale instabilities and fluid displacement patterns at the pore-network or core scales.

Solid-like interfaces between immiscible fluids may develop within reservoirs, although they are ignored in most studies. It is still unclear how this kind of interfaces affect fluid displacement. Chapter 5 shows the asymmetrical behavior of these interfaces. Chapter 6 demonstrates the potential to change the interfacial response at the pore scale by nanoparticle-coated interfaces. Many issues remain, such as the effect of particle types, asphaltene films and bio-films, interactions between particle-coated interfaces and the solid surface, and upscaling consequences.

Time is important in long-term processes, even for immiscible fluids. Results in Chapter 7 suggests the evaluation of trapped fluid (e.g. CO_2, NAPL) saturation over time should consider many phenomena such as mutual dissolution, interface pinning, wettability alteration, and corner flow. The effects of environmental conditions and fluctuations should also be considered. Chapter 8 demonstrates a method to visualize gas migration in sediments. The method and the results can be used to further study of air sparging, seafloor erosion and gas release during gas production from shallow gas hydrates.

APPENDIX A. DIFFUSION MODELS FOR CHAPTER 7

Model 1: Dissolution of a spherical drop. Concentration c varies with radial distance r and time t (Fick's second law):

$$\frac{\partial c}{\partial t} = D\left(\frac{\partial^2 c}{\partial r^2} + \frac{2}{r}\frac{\partial c}{\partial r}\right) \tag{A1}$$

where D is the diffusion coefficient. A sphere with a radius a immersed in a fluid with far-field concentration c_0 reaches saturation concentration c_{sat} at the surface $r=a$. From Equation A1, the concentration gradient at the surface is [Crank, 1975; Epstein and Plesset, 1950]:

$$\left.\frac{\partial c}{\partial r}\right|_{r=a} = \left(c_{sat} - c_0\right)\left(-\frac{1}{a} - \frac{1}{\sqrt{\pi D t}}\right) \tag{A2}$$

Therefore the mass flow from the surface is:

$$\frac{dm}{dt} = 4\pi a^2 D\left(c_{sat} - c_0\right)\left(-\frac{1}{a} - \frac{1}{\sqrt{\pi D t}}\right) \tag{A3}$$

On the other hand, mass conservation implies that

$$\frac{dm}{dt} = 4\pi a^2 \rho \frac{da}{dt} \tag{A4}$$

Equations A3 and A4 predict the rate of change in the sphere size da/dt

$$\frac{da}{dt} = \frac{D\left(c_{sat} - c_0\right)}{\rho}\left(-\frac{1}{a} - \frac{1}{\sqrt{\pi D t}}\right) \tag{A5}$$

The approximate solution for the droplet size a as a function of time t is:

$$a^2 = a_0^2 - \frac{D(c_{sat} - c_0)}{\rho} t \qquad \textit{for large } t \tag{A6}$$

where a_0 is the initial radius of the droplet.

Model 2: Trapped fluid in a capillary – Pinned interface. The mass flow reaches steady state for a capillary with a pinned interface at the pore end:

$$\frac{dm}{dt} = 2A_1 D\left(\frac{\partial c}{\partial a}\right) = A_1 D \frac{c_{sat} - c_0}{r} \tag{A7}$$

where r is the capillary radius and A_1 is the area of interface ($\pi r^2 \leq A_1 \leq 4\pi r^2$). In this case, mass conservation implies:

$$\frac{dm}{dt} = A_2 \rho \frac{dx}{dt} \tag{A8}$$

where A_2 is the cross section area. From equations A7 and A8, the filled length x evolves in time t as (A_1=A_2)

$$x = \frac{2D(c_{sat} - c_0)}{\rho r} t \tag{A9}$$

Model 3: Free interface. The mean concentration gradient is

$$\frac{\partial c}{\partial a} = \frac{2(c_{sat} - c_0)}{x} \tag{A10}$$

Substituting equation A10 into equation A7, and taking into consideration mass conservation (equation A8), the filled length as a function of time is (A_1=A_2)

$$x = 2\sqrt{\frac{2D\left(c_{sat} - c_0\right)}{\rho}t} \tag{A11}$$

REFERENCES

Abdallah, W., Buckley, J. S., Carnegie, A., Edwards, J., Herold, B., Fordham, E., Graue, A., Habashy, T., Seleznev, N., Signer, C., Montaron, B., Hussain, H., & Ziauddin, M. (2007). Fundamentals of wettability. *Oilfield Review*, *19*(2), 44-61.

Abegg, F., & Anderson, A. L. (1997). The acoustic turbid layer in muddy sediments of Eckernfoerde Bay, Western Baltic: methane concentration, saturation and bubble characteristics. *Marine Geology*, *137(1)*, 137-147.

Abkarian, M., Subramaniam, A. B., Kim, S. H., Larsen, R. J., Yang, S. M., & Stone, H. A. (2007). Dissolution arrest and stability of particle-covered bubbles. *Physical review letters*, 99(18), 188301.

Ahmed, M., & Iskander, M. (2012). Evaluation of tunnel face stability by transparent soil models. *Tunnelling and Underground Space Technology,27(1)*, 101-110.

Al-Anssari, S., Barifcani, A., Wang, S., & Iglauer, S. (2016). Wettability alteration of oil-wet carbonate by silica nanofluid. *Journal of colloid and interface science, 461*, 435-442.

Alfaro, M. C., & Wong, R. C. (2001). Laboratory studies on fracturing of low-permeability soils. *Canadian Geotechnical Journal*, 38(2), 303-315.

Aluko, O. B., & Seig, D. A. (2000). An experimental investigation of the characteristics of and conditions for brittle fracture in two-dimensional soil cutting. *Soil and Tillage Research, 57(3)*, 143-157.

Alvarellos, J. (2003). *Fundamental Studies of Capillary Forces in Porous Media.* Georgia Tech, Atlanta.

Andersen, K. H., Rawlings, C. G., Lunne, T. A., & By, T. H. (1994). Estimation of hydraulic fracture pressure in clay. *Canadian geotechnical journal, 31(6)*, 817-828.

Anderson, A. L., Abegg, F., Hawkins, J. A., Duncan, M. E., & Lyons, A. P. (1998). Bubble populations and acoustic interaction with the gassy floor of Eckernförde Bay. *Continental Shelf Research, 18(14)*, 1807-1838.

Anderson, W. (1986). Wettability literature survey-part 1: Rock/oil/brine interactions and the effects of core handling on wettability. *Journal of Petroleum Technology*, *38*(11), 1-246.

Andreassen, K., Hubbard, A., Winsborrow, M., Patton, H., Vadakkepuliyambatta, S., Plaza-Faverola, A., Gudlaugsson, E., Serov, P., Deryabin, A., Mattingsdal, R., Mienert, J., & Bunz, S. (2017). Massive blow-out craters formed by hydrate-controlled methane expulsion from the Arctic seafloor. *Science, 356(6341),* 948-953.

Andrew, M., Bijeljic, B., & Blunt, M. J. (2014). Pore-scale imaging of trapped supercritical carbon dioxide in sandstones and carbonates. *International Journal of Greenhouse Gas Control, 22*, 1-14.

Armstrong, R. T., & Berg, S. (2013). Interfacial velocities and capillary pressure gradients during Haines jumps. *Physical Review E, 88(4)*, 043010.

Arriola, A., Willhite, G. P., & Green, D. W. (1983). Trapping of oil drops in a noncircular pore throat and mobilization upon contact with a surfactant. *Society of Petroleum Engineers Journal*, *23*(01), 99-114.

Asekomhe, S. O., Chiang, R., Masliyah, J. H., & Elliott, J. A. (2005). Some observations on the contraction behavior of a water-in-oil drop with attached solids. *Industrial & engineering chemistry research, 44(5)*, 1241-1249.

Aumaitre, E., Vella, D., & Cicuta, P. (2011). On the measurement of the surface pressure in Langmuir films with finite shear elasticity. *Soft Matter*, *7(6)*, 2530-2537.

Aussillous, P., & Quéré, D. (2001). Liquid marbles. *Nature*, *411(6840)*, 924-927.

Babadagli, T. (2007). Development of mature oil fields—a review. *Journal of Petroleum Science and Engineering, 57(3),* 221-246.

Bang, E. S., Son, J. S., & Santamarina, J. C. (2013). Subsurface CO_2 leakage: Lab-scale study of salient characteristics and assessment of borehole-based detection using resistivity tomography. In *Geotechnical and Geophysical Site Characterization 4*. Taylor & Francis Group London.

Barry, M. A., Boudreau, B. P., Johnson, B. D., & Reed, A. H. (2010). First-order description of the mechanical fracture behavior of fine-grained surficial marine sediments during gas bubble growth. *Journal of Geophysical Research: Earth Surface, 115(F4).*

Bechtel, S. E., K. W. Koelling, W. Nguyen and G. Tan (2002), A new technique for the measurement of the dynamic evolution of surface tension, *J Colloid Interf Sci, 245(1)*, 142-162.

Bennion, B. and S. Bachu (2006), The impact of interfacial tension and pore size distribution/capillary pressure character on CO_2 relative permeability at reservoir conditions in CO_2-brine systems, *SPE*, 99325-MS.

Bensimon, D., Kadanoff, L. P., Liang, S., Shraiman, B. I., & Tang, C. (1986). Viscous flows in two dimensions. *Reviews of Modern Physics, 58(4)*, 977.

Berg, S., Ott, H., Klapp, S. A., Schwing, A., Neiteler, R., Brussee, N., Makurat, A., Leu, L., Enzmann, F., Schwarz, J., Kersten, M., Irvine, S., and Stampanoni, M. (2013). Real-time 3D imaging of Haines jumps in porous media flow. *Proceedings of the National Academy of Sciences, 110(10)*, 3755-3759.

Berhanu, M., & Kudrolli, A. (2010). Heterogeneous structure of granular aggregates with capillary interactions. *Physical review letters, 105(9)*, 098002.

Beysens, D. (2006). Dew nucleation and growth. *Comptes Rendus Physique, 7(9-10),* 1082-1100.

Bico, J., & Quéré, D. (2002). Rise of liquids and bubbles in angular capillary tubes. *Journal of colloid and Interface Science*, *247*(1), 162-166.

Bihi, I., Baudoin, M., Butler, J. E., Faille, C., & Zoueshtiagh, F. (2016). Inverse Saffman-Taylor experiments with particles lead to capillarity driven fingering instabilities. *Physical review letters, 117(3),* 034501.

Binks, B. P. (2002). Particles as surfactants—similarities and differences. *Current opinion in colloid & interface science, 7(1),* 21-41.

Binks, B. P., & Murakami, R. (2006). Phase inversion of particle-stabilized materials from foams to dry water. *Nature materials, 5(11),* 865-869.

Bjerrum, L., Nash, J. K. T. L., Kennard, R. M., & Gibson, R. E. (1972). Hydraulic fracturing in field permeability testing. *Geotechnique, 22(2),* 319-332.

Blake, T. D. (2006). The physics of moving wetting lines. *Journal of Colloid and Interface Science*, *299*(1), 1-13.

Bloomfield, J. P., D. C. Gooddy, M. I. Bright and P. J. Williams (2001), Pore-throat size distributions in Permo-Triassic sandstones from the United Kingdom and some implications for contaminant hydrogeology, *Hydrogeol J, 9(3),* 219-230.

Blunt, M., Zhou, D., & Fenwick, D. (1995). Three-phase flow and gravity drainage in porous media. In *Multiphase Flow in Porous Media* (pp. 77-103). Springer Netherlands.

Boistelle, R., & Astier, J. P. (1988). Crystallization mechanisms in solution. *Journal of Crystal Growth, 90(1-3),* 14-30.

Böker, A., He, J., Emrick, T., & Russell, T. P. (2007). Self-assembly of nanoparticles at interfaces. *Soft matter, 3(10),* 1231-1248.

Bonn, D., Kellay, H., Amar, M. B., & Meunier, J. (1995). Viscous finger widening with surfactants and polymers. *Physical review letters, 75(11),* 2132.

Bordács, S., Agod, A., & Hórvölgyi, Z. (2006). Compression of Langmuir films composed of fine particles: collapse mechanism and wettability. *Langmuir, 22(16),* 6944-6950.

Boudreau, B. P. (2012). The physics of bubbles in surficial, soft, cohesive sediments. *Marine and Petroleum Geology, 38(1),* 1-18.

Bresme, F., & Oettel, M. (2007). Nanoparticles at fluid interfaces. *Journal of Physics: Condensed Matter, 19(41),* 413101.

Brooks, R. H., & Corey, A. T. (1964). Hydraulic properties of porous media and their relation to drainage design. *Trans. ASAE, 7*(1), 0026-0028.

Buckley, J. S. (2001). Effective wettability of minerals exposed to crude oil. *Current opinion in colloid & interface science*, *6*(3), 191-196.

Buckley, J. S., & Liu, Y. (1998). Some mechanisms of crude oil/brine/solid interactions. *Journal of Petroleum Science and Engineering*, *20*(3), 155-160.

Butt, H., Graf, K., & Kappl, M. (2003). *Physics and chemistry of interfaces*. WILEY-VCH GmbH & Co. KGaA, Weinheim

Camuffo, D. (1984). Condensation-evaporation cycles in pore and capillary systems according to the Kelvin model. *Water, Air, and Soil Pollution*, *21*(1-4), 151-159.

Cao, L. F., Teh, C. I., & Chang, M. F. (2001). Undrained cavity expansion in modified Cam clay. *Geotechnique, 51(4),* 323-34.

Carter, J. P., Booker, J. Y., & Yeung, S. K. (1986). Cavity expansion in cohesive frictional soils. *Geotechnique, 36(3),* 349-358.

Caskey, J. A. and W. B. Barlage (1971), Improved experimental technique for determining dynamic surface tension of water and surfactant solutions, *J Colloid Interf Sci, 35(1),* 46-52.

Cassie, A. B. D., & Baxter, S. (1944). Wettability of porous surfaces. *Transactions of the Faraday Society, 40*, 546-551.

Cha, M., Santamarina, J. C., Kim, H. S., & Cho, G. C. (2014). Small-strain stiffness, shear-wave velocity, and soil compressibility. *Journal of Geotechnical and Geoenvironmental Engineering, 140(10),* 06014011.

Chalbaud, C., Robin, M., Lombard, J. M., Martin, F., Egermann, P., & Bertin, H. (2009). Interfacial tension measurements and wettability evaluation for geological CO_2 storage. *Advances in Water Resources*, *32*(1), 98-109.

Chatzis, I. and F. A. L. Dullien (1983), Dynamic immiscible displacement mechanisms in pore doublets - theory versus experiment, *J Colloid Interf Sci, 91(1),* 199-222.

Chatzis, I., Morrow, N. R., & Lim, H. T. (1983). Magnitude and detailed structure of residual oil saturation. *Society of Petroleum Engineers Journal, 23(02),* 311-326.

Chen, P. L. and K. K. Mohanty (2013), Surfactant-mediated spontaneous imbibition in carbonate rocks at harsh reservoir conditions, *SPE J, 18(1),* 124-133.

Cheng, C. Y., Dasari, G. R., Chow, Y. K., & Leung, C. F. (2007). Finite element analysis of tunnel–soil–pile interaction using displacement controlled model. *Tunnelling and Underground Space Technology, 22(4),* 450-466.

Chevalier, Y., & Bolzinger, M. A. (2013). Emulsions stabilized with solid nanoparticles: Pickering emulsions. *Colloids and Surfaces A: Physicochemical and Engineering Aspects, 439*, 23-34.

Cho, G. C., & Santamarina, J. C. (2001). Unsaturated particulate materials—particle-level studies. *Journal of geotechnical and geoenvironmental engineering*, *127*(1), 84-96.

Choi, D., Lee, H., Kang, I. S., Lim, G., Kim, D. S., & Kang, K. H. (2013). Spontaneous electrical charging of droplets by conventional pipetting. *Scientific reports*, *3*, 2037.

Cicuta, P., & Vella, D. (2009). Granular character of particle rafts. *Physical review letters, 102(13),* 138302.

Cicuta, P., Stancik, E. J., & Fuller, G. G. (2003). Shearing or compressing a soft glass in 2D: time-concentration superposition. *Physical review letters, 90(23),* 236101.

Clayton, C. J., & Hay, S. J. (1994). Gas migration mechanisms from accumulation to surface. *Bulletin of the Geological Society of Denmark,41(1),* 12-23.

Clements, J. A., Brown, E. S., & Johnson, R. P. (1958). Pulmonary surface tension and the mucus lining of the lungs: some theoretical considerations. *J. of app. physiology*, *12*(2), 262-268.

Clennell, M. B., Judd, A., & Hovland, M. (2000). Movement and accumulation of methane in marine sediments: relation to gas hydrate systems. In *Natural Gas Hydrate* (pp. 105-122). Springer Netherlands.

Coussy, O. (2007). Revisiting the constitutive equations of unsaturated porous solids using a Lagrangian saturation concept. *International Journal for Numerical and Analytical Methods in Geomechanics*, *31*(15), 1675-1694.

Coussy, O. (2010). *Mechanics and physics of porous solids*. John Wiley & Sons, Ltd. Chichester, UK.

Coussy, O., & Brisard, S. (2009). Prediction of drying shrinkage beyond the pore isodeformation assumption. *Journal of Mechanics of Materials and Structures*, *4*(2), 263-279.

Coussy, O., & Monteiro, P. (2007). Unsaturated poroelasticity for crystallization in pores. *Computers and geotechnics*, *34*(4), 279-290.

Crank, J. (1979). *The Mathematics of Diffusion*. Oxford university press, New York.

Dai, S., & Santamarina, J. C. (2013). Water retention curve for hydrate-bearing sediments. *Geophysical Research Letters*, *40*(21), 5637-5641.

Dai, S., Santamarina, J. C., Waite, W. F., & Kneafsey, T. J. (2012). Hydrate morphology: Physical properties of sands with patchy hydrate saturation. *Journal of Geophysical Research: Solid Earth*, *117*, B11205.

Daniel, D. E., L. Alvarez, W. Dershowitz, H. H. Einstein, C. Gable, F. M. Orr, D. Reynolds, J. C. Santamarina, A. M. Shapiro and K. Singha (2015), *Characterization, Modeling, Monitoring and Remediation of Fractured Rock*, National Academis Press.

Dasgupta, S., Auth, T., & Gompper, G. (2017). Nano-and microparticles at fluid and biological interfaces. *Journal of Physics: Condensed Matter*, *29(37)*, 373003.

Datta, S. S., Shum, H. C., & Weitz, D. A. (2010). Controlled buckling and crumpling of nanoparticle-coated droplets. *Langmuir*, *26(24)*, 18612-18616.

De Gennes, P. G. (1985), Wetting: static and dynamics, *Rev Mod Phys*, *57(3)*, 827-863.

De Gennes, P. G., Brochard-Wyart, F., & Quéré, D. (2004). *Capillarity and wetting phenomena: drops, bubbles, pearls, waves*. Springer Science & Business Media, New York

de Pater, C. J., Dong, Y., & Bohloli, B. (2007, January). Experimental study of hydraulic fracturing in sand as a function of stress and fluid rheology. *In SPE hydraulic fracturing technology conference*. Society of Petroleum Engineers.

De Prunele, A., Ruffine, L., Riboulot, V., Peters, C. A., Croguennec, C., Guyader, V., ... & Germain, Y. (2017). Focused hydrocarbon-migration in shallow sediments of a

pockmark cluster in the Niger Delta (Off Nigeria). *Geochemistry, Geophysics, Geosystems, 18(1),* 93-112.

Deák, A., Hild, E., Kovács, A. L., & Hórvölgyi, Z. (2007). Contact angle determination of nanoparticles: film balance and scanning angle reflectometry studies. *Physical Chemistry Chemical Physics, 9(48),* 6359-6370.

Defay, R. and I. Prigogine (1949), Surface tension of regular solutions, *Trans Faraday Soc, 46,* 199-204.

Dembicki Jr, H., & Anderson, M. J. (1989). Secondary migration of oil: Experiments supporting efficient movement of separate, buoyant oil phase along limited conduits: Geologic note. *AAPG Bulletin, 73(8),* 1018-1021.

Demond, A. H., & Lindner, A. S. (1993). Estimation of interfacial tension between organic liquids and water. *Environmental Science & Technology, 27(12),* 2318-2331.

Derganc, J., Antonny, B., & Čopič, A. (2013). Membrane bending: the power of protein imbalance. *Trends in biochemical sciences, 38(11),* 576-584.

Deshmukh, O. S., van den Ende, D., Stuart, M. C., Mugele, F., & Duits, M. H. (2015). Hard and soft colloids at fluid interfaces: Adsorption, interactions, assembly & rheology. *Advances in colloid and interface science, 222,* 215-227.

Diamantopoulos, E., & Durner, W. (2012). Dynamic nonequilibrium of water flow in porous media: A review. *Vadose Zone Journal*, *11*(3).

DiCarlo, D. A., Aminzadeh, B., Roberts, M., Chung, D. H., Bryant, S. L., & Huh, C. (2011). Mobility control through spontaneous formation of nanoparticle stabilized emulsions. *Geophysical Research Letters, 38(24).*

Dickey, P. A. (1975). Possible primary migration of oil from source rock in oil phase: Geologic notes. *AAPG Bulletin, 59(2),* 337-345.

Dominik, C., & Tielens, A. G. G. M. (1995). Resistance to rolling in the adhesive contact of two elastic spheres. *Philosophical Magazine A, 72(3),* 783-803.

Dong, M., & Chatzis, I. (1995). The imbibition and flow of a wetting liquid along the corners of a square capillary tube. *Journal of colloid and interface science*, *172*(2), 278-288.

Dorsey, A. T., & Martin, O. (1987). Saffman-Taylor fingers with anisotropic surface tension. *Physical Review A, 35(9),* 3989.

Drescher, A., & De Jong, G. D. J. (1972). Photoelastic verification of a mechanical model for the flow of a granular material. *Journal of the Mechanics and Physics of Solids, 20(5),* 337-340.

Drummond, C., & Israelachvili, J. (2004). Fundamental studies of crude oil–surface water interactions and its relationship to reservoir wettability. *Journal of Petroleum Science and Engineering*, *45*(1), 61-81.

Du, K., Glogowski, E., Emrick, T., Russell, T. P., & Dinsmore, A. D. (2010). Adsorption energy of nano-and microparticles at liquid− liquid interfaces. *Langmuir, 26(15),* 12518-12522.

Dullien, F. A. (1992). *Porous Media: Fluid Transport and Pore Structure.* Academic press, San Diego, California.

Dupre, S., Scalabrin, C., Grall, C., Augustin, J. M., Henry, P., Şengör, A. M., Goeruer, N., Cagatay, M., & Géli, L. (2015). Tectonic and sedimentary controls on widespread gas emissions in the Sea of Marmara: Results from systematic, shipborne multibeam echo sounder water column imaging. *Journal of Geophysical Research: Solid Earth, 120(5),* 2891-2912.

Eiji Yannagisawa and Ali Komak Panah (1994). Two dimensional study of hydraulic fracturing criteria in cohesive soils. *Soils and Foundations, 34(1),* 1-9.

Epstein, P. S., & Plesset, M. S. (1950). On the stability of gas bubbles in liquid-gas solutions. *The Journal of Chemical Physics, 18(11),* 1505-1509.

Espinoza, D. N., & Santamarina, J. C. (2010). Water-CO_2-mineral systems: Interfacial tension, contact angle, and diffusion—Implications to CO_2 geological storage. *Water resources research*, *46*, W03537.

Espinoza, D. N., & Santamarina, J. C. (2012). Clay interaction with liquid and supercritical CO_2: the relevance of electrical and capillary forces. *International Journal of Greenhouse Gas Control, 10*, 351-362.

Essaid, H. I., Bekins, B. A., & Cozzarelli, I. M. (2015). Organic contaminant transport and fate in the subsurface: Evolution of knowledge and understanding. *Water Resources Research, 51(7),* 4861-4902.

Essaid, H. I., W. N. Herkelrath and K. M. Hess (1993), Simulation of fluid distributions observed at a crude-oil spill site incorporating hysteresis, oil entrapment, and spatial variability of hydraulic-properties, *Water Resour Res*, *29(6),* 1753-1770.

Etiope, G., & Martinelli, G. (2002). Migration of carrier and trace gases in the geosphere: an overview. *Physics of the earth and planetary interiors, 129(3),* 185-204.

Ezzein, F. M. & Bathurst, R. J. (2011). A Transparent Sand for Geotechnical Laboratory Modeling.*Geotechnical Testing Journal, 34 (6),* 1-12.

Fauria, K. E., & Rempel, A. W. (2011). Gas invasion into water-saturated, unconsolidated porous media: Implications for gas hydrate reservoirs. *Earth and Planetary Science Letters, 312(1),* 188-193.

Ferdous, S., Ioannidis, M. A., & Henneke, D. (2011). Adsorption kinetics of alkanethiol-capped gold nanoparticles at the hexane–water interface. *Journal of Nanoparticle Research, 13(12),* 6579-6589.

Francisca, F. M., Rinaldi, V. A., & Santamarina, J. C. (2003). Instability of hydrocarbon films over mineral surfaces: Microscale experimental studies. *Journal of environmental engineering*, *129*(12), 1120-1128.

Fredlund, D. G. (2000). The 1999 RM Hardy Lecture: The implementation of unsaturated soil mechanics into geotechnical engineering. *Canadian Geotechnical Journal*, *37*(5), 963-986.

Fredrickson, J. K., J. P. McKinley, B. N. Bjornstad, P. E. Long, D. B. Ringelberg, D. C. White, L. R. Krumholz, J. M. Suflita, F. S. Colwell, R. M. Lehman, T. J. Phelps and T. C. Onstott (1997), Pore-size constraints on the activity and survival of subsurface bacteria in a late Cretaceous shale-sandstone sequence, northwestern New Mexico, *Geomicrobiol J, 14(3),* 183-202.

Frelichowska, J., Bolzinger, M. A., Pelletier, J., Valour, J. P., & Chevalier, Y. (2009). Topical delivery of lipophilic drugs from o/w Pickering emulsions. *International journal of pharmaceutics, 371(1-2),* 56-63.

Frelichowska, J., Bolzinger, M. A., Valour, J. P., Mouaziz, H., Pelletier, J., & Chevalier, Y. (2009). Pickering w/o emulsions: drug release and topical delivery. *International Journal of Pharmaceutics, 368(1),* 7-15.

Furuberg, L., K. J. Maloy and J. Feder (1996), Intermittent behavior in slow drainage, *Phys Rev E, 53(1),* 966-977.

Gai, Y., Kim, M., Pan, M., & Tang, S. K. (2017). Amphiphilic nanoparticles suppress droplet break-up in a concentrated emulsion flowing through a narrow constriction. *Biomicrofluidics, 11(3),* 034117.

Gallipoli, D., Gens, A., Sharma, R., & Vaunat, J. (2003). An elasto-plastic model for unsaturated soil incorporating the effects of suction and degree of saturation on mechanical behaviour. *Géotechnique.*, *53*(1), 123-136.

Gao, S., Moran, K., Xu, Z., & Masliyah, J. (2009). Role of bitumen components in stabilizing water-in-diluted oil emulsions. *Energy & Fuels, 23(5),* 2606-2612.

Garcimartín, A., Zuriguel, I., Pugnaloni, L. A., & Janda, A. (2010). Shape of jamming arches in two-dimensional deposits of granular materials. *Physical Review E, 82(3),* 031306.

Gauglitz, P. A., & Radke, C. J. (1989). Dynamics of Haines jumps for compressible bubbles in constricted capillaries. *AIChE journal*, *35*(2), 230-240.

Gens, A. (2010), Soil-environment interactions in geotechnical engineering, *Geotechnique, 60(1),* 3-74.

Gerber, F., M. P. Krafft, T. F. Vandamme, M. Goldmann and P. Fontaine (2006), Fluidization of a dipalmitoyl phosphatidylcholine monolayer by fluorocarbon gases: Potential use in lung surfactant therapy, *Biophys J, 90(9),* 3184-3192.

Ghadiali, S. N. and D. P. Gaver (2000), An investigation of pulmonary surfactant physicochemical behavior under airway reopening conditions, *J Appl Physiol, 88(2),* 493-506.

Ghadiali, S. N. and D. P. Gaver (2008), Biomechanics of liquid-epithelium interactions in pulmonary airways, *Resp Physiol Neurobi, 163(1-3),* 232-243.

Ghumare, A. K. (2012), *Synthesis, Characterization and Applications of Cationic Gemini Surfactants,* PhD Thesis, Institute of Chemical Technology, Mumbai, India.

Gilfillan, S. M., Lollar, B. S., Holland, G., Blagburn, D., Stevens, S., Schoell, M., Cassidy, M., Ding, Z., Zhou, Z., Lacrampe-Couloume, G. & Ballentine, C. J. (2009).

Solubility trapping in formation water as dominant CO2 sink in natural gas fields. *Nature, 458(7238),* 614-618.

Gill, D. & Lehane, B. (2001). An Optical Technique for Investigating Soil Displacement Patterns.*Geotechnical Testing Journal, 24 (3),* 324-329.

Giordano, R. M., & Slattery, J. C. (1983). Stability of static interfaces in a sinusoidal capillary. *Journal of Colloid and Interface Science, 92(1),* 13-24.

Glass, R. J., S. H. Conrad and W. Peplinski (2000), Gravity-destabilized nonwetting phase invasion in macroheterogeneous porous media: Experimental observations of invasion dynamics and scale analysis, *Water Resour Res, 36(11),* 3121-3137.

Good, R. J. (1966), Estimation of surface energies from contact angles, *Nature, 212(5059),* 276-277.

Goringe, M. J., & Gardner, T. N. (1988). The measurement of gas bubble size distributions in a three phase laboratory gassy soil.

Gruener, S., Sadjadi, Z., Hermes, H. E., Kityk, A. V., Knorr, K., Egelhaaf, S. U., Rieger, H. & Huber, P. (2012). Anomalous front broadening during spontaneous imbibition in a matrix with elongated pores. *Proceedings of the National Academy of Sciences, 109(26),* 10245-10250.

Guo, D., Xie, G., & Luo, J. (2013). Mechanical properties of nanoparticles: basics and applications. *Journal of physics D: applied physics, 47(1),* 013001.

Guzman, I. L., Iskander, M., Suescun-Florez, E., & Omidvar, M. (2014). A transparent aqueous-saturated sand surrogate for use in physical modeling.*Acta Geotechnica, 9(2),* 187-206.

Haigh, S. K., Vardanega, P. J., & Bolton, M. D. (2013). The plastic limit of clays. Géotechnique, 63(6), 435.

Haines, W. B. (1930). Studies in the physical properties of soil. V. The hysteresis effect in capillary properties, and the modes of moisture distribution associated therewith. *The Journal of Agricultural Science, 20(1),* 97-116.

Hassanizadeh, S. M., Celia, M. A., & Dahle, H. K. (2002). Dynamic effect in the capillary pressure–saturation relationship and its impacts on unsaturated flow. *Vadose Zone Journal, 1*(1), 38-57.

Hatibu, N., & Hettiaratchi, D. R. P. (1993). The transition from ductile flow to brittle failure in unsaturated soils. *Journal of agricultural engineering research, 54(4),* 319-328.

Haynes, W. M. (Ed.). (2014). *CRC Handbook of Chemistry and Physics*. Taylor and Francis, Boca Raton, FL.

Heim, L. O., Blum, J., Preuss, M., & Butt, H. J. (1999). Adhesion and friction forces between spherical micrometer-sized particles. *Physical Review Letters, 83(16),* 3328.

Hettiaratchi, D. R. P., & O'Callaghan, J. R. (1980). Mechanical behaviour of agricultural soils. *Journal of Agricultural Engineering Research, 25(3),* 239-259.

Hill, S. (1952). Channeling in packed columns. *Chemical Engineering Science, 1(6),* 247-253.

Hirasaki, G. J., C. A. Miller and M. Puerto (2011), Recent advances in surfactant EOR, *SPE J, 16(4),* 889-907.

Hoffman, R. L. (1975), Study of advancing interface .1. Interface shape in liquid-gas systems, *J Colloid Interf Sci, 50(2),* 228-241.

Holmberg, K., B. Josson, B. Kronberg and B. Lindman (2003), *Surfactants and Polymers in Aqueous Solution*, John Wiley & Sons, Ltd, Chichester, UK.

Holtzman, R., & Segre, E. (2015). Wettability stabilizes fluid invasion into porous media via nonlocal, cooperative pore filling. *Physical review letters, 115(16),* 164501.

Holtzman, R., M. L. Szulczewski and R. Juanes (2012), Capillary fracturing in granular media, *Phys Rev Lett, 108(26),* 264504.

Homsy, G. M. (1987). Viscous fingering in porous media. *Annual review of fluid mechanics, 19(1),* 271-311.

Horozov, T. S., Binks, B. P., Aveyard, R., & Clint, J. H. (2006). Effect of particle hydrophobicity on the formation and collapse of fumed silica particle monolayers at the oil–water interface. *Colloids and Surfaces A: Physicochemical and Engineering Aspects, 282*, 377-386.

Hsu, S. Y., & Hilpert, M. (2015). Pore-scale visualization of the mobilization of a partially wetting droplet. *Advances in Water Resources, 95,* 235-245.

Hsu, S. Y., Glantz, R., & Hilpert, M. (2012). Pore-scale analysis of the effects of contact angle hysteresis on blob mobilisation in a pore doublet. *International Journal of Oil, Gas and Coal Technology, 5(2-3),* 207-228.

Huang, H., Zhang, F., Callahan, P., & Ayoub, J. A. (2012). Fluid injection experiments in 2d porous media. *SPE Journal, 17(03),* 903-911.

Huang, Z., Z. L. Yan and T. R. Gu (1989), Mixed adsorption of cationic and anionic surfactants from aqueous-solution on silica-gel, *Colloid Surface, 36(3),* 353-358.

Iglauer, S., Y. F. Wu, P. Shuler, Y. C. Tang and W. A. Goddard (2010), New surfactant classes for enhanced oil recovery and their tertiary oil recovery potential, *J Petrol Sci Eng, 71(1-2),* 23-29.

Iskander, M. (2010). *Modelling with transparent soils: Visualizing soil structure interaction and multi phase flow, non-intrusively*. Springer Science & Business Media.

Iskander, M., Lai, J., Oswald, C., & Mannheimer, R. (1994). Development of a Transparent Material to Model the Geotechnical Properties of Soils. *Geotechnical Testing Journal, 17 (4),* 425-433.

Israelachvili, J. N. (2011), *Intermolecular and Surface Forces*, Academic Press, San Diego, CA.

Jain, A. K., & Juanes, R. (2009). Preferential mode of gas invasion in sediments: Grain-scale mechanistic model of coupled multiphase fluid flow and sediment mechanics. *Journal of Geophysical Research: Solid Earth,114(B8).*

Jambon-Puillet, E., & Protière, S. (2016). Drop floating on a granular raft. *Physical Review Fluids, 1(5),* 050501.

Jambon-Puillet, E., Josserand, C., & Protière, S. (2017). Wrinkles, folds, and plasticity in granular rafts. *Physical Review Materials, 1(4),* 042601.

Jang, J., & Santamarina, J. C. (2011). Recoverable gas from hydrate-bearing sediments: Pore network model simulation and macroscale analyses. *Journal of geophysical research: Solid Earth, 116*(B8).

Jang, J., & Santamarina, J. C. (2014). Evolution of gas saturation and relative permeability during gas production from hydrate-bearing sediments: Gas invasion vs. gas nucleation. *Journal of Geophysical Research: Solid Earth, 119*(1), 116-126.

Jang, J., Sun, Z., & Santamarina, J. C. (2016). Capillary pressure across a pore throat in the presence of surfactants. *Water Resources Research, 52*, 9586–9599.

Jasper, J. J. (1972). The surface tension of pure liquid compounds. *Journal of physical and chemical reference data, 1*(4), 841-1010.

Jaworski, G. W., Duncan, J. M., & Seed, H. B. (1981). Laboratory study of hydraulic fracturing. *J. Geotech. Eng. Div., Am. Soc. Civ. Eng.;(United States), 107.*

Jeng, D. S. (2003). Wave-induced sea floor dynamics. Applied Mechanics Reviews, 56(4), 407-429.

Johannessen, A. M. and K. Spildo (2013), Enhanced oil recovery (EOR) by combining surfactant with low salinity injection, *Energ Fuel, 27(10),* 5738-5749.

Johnson, B. D., Boudreau, B. P., Gardiner, B. S., & Maass, R. (2002). Mechanical response of sediments to bubble growth. *Marine Geology,187(3),* 347-363.

Jung, J. W., Jang, J., Santamarina, J. C., Tsouris, C., Phelps, T. J., & Rawn, C. J. (2012). Gas production from hydrate-bearing sediments: the role of fine particles. *Energy & Fuels*, *26*(1), 480-487.

Kalikmanov, V. (2013). *Nucleation theory* (Vol. 860). Springer. Netherlands.

Kang, Z., Yeung, A., Foght, J. M., & Gray, M. R. (2008). Mechanical properties of hexadecane–water interfaces with adsorbed hydrophobic bacteria. *Colloids and Surfaces B: Biointerfaces, 62(2),* 273-279.

Karapetsas, G., Sahu, K. C., Sefiane, K., & Matar, O. K. (2014). Thermocapillary-driven motion of a sessile drop: effect of non-monotonic dependence of surface tension on temperature. *Langmuir, 30*(15), 4310-4321.

Ketcham, R. A., & Carlson, W. D. (2001). Acquisition, optimization and interpretation of X-ray computed tomographic imagery: applications to the geosciences. *Computers & Geosciences, 27(4),* 381-400.

Keulen, B. (2001). *Maximum allowable pressures during horizontal directional drillings focused on sand* (Doctoral dissertation, TU Delft, Delft University of Technology).

Khalili, N., Habte, M. A., & Zargarbashi, S. (2008). A fully coupled flow deformation model for cyclic analysis of unsaturated soils including hydraulic and mechanical hystereses. *Computers and Geotechnics*, *35*(6), 872-889.

Kim, J. K., Rühs, P. A., Fischer, P., & Hong, J. S. (2013). Interfacial localization of nanoclay particles in oil-in-water emulsions and its reflection in interfacial moduli. *Rheologica acta*, *52(4)*, 327-335.

Kim, J., Xu, F., & Lee, S. (2017). Formation and destabilization of the particle band on the fluid-fluid interface. *Physical review letters*, *118(7)*, 074501.

Kim, S. and J. C. Santamarina (2014), Engineered CO2 injection: The use of surfactants for enhanced sweep efficiency, *Int J Greenh Gas Con*, *20*, 324-332.

Koch, K., & Barthlott, W. (2009). Superhydrophobic and superhydrophilic plant surfaces: an inspiration for biomimetic materials. *Philosophical Transactions of the Royal Society of London A: Mathematical, Physical and Engineering Sciences*, *367(1893)*, 1487-1509.

Kodikara, J., Barbour, S. L., & Fredlund, D. G. (1999). Changes in clay structure and behaviour due to wetting and drying. In *Proceedings 8th Australia New Zealand Conference on Geomechanics: Consolidating Knowledge* (p. 179). Australian Geomechanics Society.

Kondic, L., Shelley, M. J., & Palffy-Muhoray, P. (1998). Non-newtonian hele-shaw flow and the saffman-taylor instability. *Physical Review Letters*, *80(7)*, 1433.

Kovscek, A. R., Wong, H., & Radke, C. J. (1993). A Pore-Level Scenario for the Development of Mixed Wettability in Oil Reservoirs. *AIChE Journal*, *39*(6), 1073.

Kralchevsky, P. A., Ivanov, I. B., Ananthapadmanabhan, K. P., & Lips, A. (2005). On the thermodynamics of particle-stabilized emulsions: curvature effects and catastrophic phase inversion. *Langmuir*, *21(1)*, 50-63.

Krummel, A. T., Datta, S. S., Münster, S., & Weitz, D. A. (2013). Visualizing multiphase flow and trapped fluid configurations in a model three-dimensional porous medium. *AIChE Journal*, *59(3)*, 1022-1029.

Kutuzov, S., He, J., Tangirala, R., Emrick, T., Russell, T. P., & Böker, A. (2007). On the kinetics of nanoparticle self-assembly at liquid/liquid interfaces. *Physical Chemistry Chemical Physics*, *9(48)*, 6351-6358.

Kwok, D. Y. and A. W. Neumann (2000), Contact angle interpretation in terms of solid surface tension, *Colloid Surface A*, *161(1)*, 31-48.

Lago, M., & Araujo, M. (2001). Threshold pressure in capillaries with polygonal cross section. *Journal of colloid and interface science*, *243*(1), 219-226.

Le, T. M. H., Gallipoli, D., Sanchez, M., & Wheeler, S. J. (2012). Stochastic analysis of unsaturated seepage through randomly heterogeneous earth

embankments. *International Journal for Numerical and Analytical Methods in Geomechanics*, *36*(8), 1056-1076.

Leahy, B. D., Pocivavsek, L., Meron, M., Lam, K. L., Salas, D., Viccaro, P. J., Lee, K. C., & Lin, B. (2010). Geometric stability and elastic response of a supported nanoparticle film. *Physical review letters*, *105(5)*, 058301.

Lee, J. S., & Santamarina, J. C. (2005). Bender elements: performance and signal interpretation. *Journal of geotechnical and geoenvironmental engineering*, *131(9)*, 1063-1070.

Lenormand, R., Touboul, E., & Zarcone, C. (1988). Numerical models and experiments on immiscible displacements in porous media. *Journal of fluid mechanics*, *189*, 165-187.

Lenormand, R., Zarcone, C., & Sarr, A. (1983). Mechanisms of the displacement of one fluid by another in a network of capillary ducts. *Journal of Fluid Mechanics*, *135*, 337-353.

Levine, S., Bowen, B. D., & Partridge, S. J. (1989). Stabilization of emulsions by fine particles I. Partitioning of particles between continuous phase and oil/water interface. *Colloids and Surfaces*, *38(2)*, 325-343.

Lewicki, J. L., Birkholzer, J., & Tsang, C. F. (2007). Natural and industrial analogues for leakage of CO_2 from storage reservoirs: identification of features, events, and processes and lessons learned. *Environmental Geology*, *52(3)*, 457-467.

Li, W. Q., R. D. Vigil, I. A. Beresnev, P. Iassonov and R. Ewing (2005), Vibration-induced mobilization of trapped oil ganglia in porous media: Experimental validation of a capillary-physics mechanism, *J Colloid Interf Sci*, *289(1)*, 193-199.

Liggieri, L., Ravera, F., & Passerone, A. (1990). Drop formation instabilities induced by entrapped gas bubbles. *Journal of colloid and interface science*, *140(2)*, 436-443.

Likos, W. J. and N. Lu (2004), Hysteresis of capillary stress in unsaturated granular soil, *J Eng Mech-Asce*, *130(6)*, 646-655.

Lindner, A., Coussot, P., & Bonn, D. (2000). Viscous fingering in a yield stress fluid. *Physical Review Letters*, *85(2)*, 314.

Liou, W. W., Peng, Y., & Parker, P. E. (2009). Analytical modeling of capillary flow in tubes of nonuniform cross section. *Journal of colloid and interface science*, *333(1)*, 389-399.

Liu, J., & Iskander, M. G. (2010). Modelling capacity of transparent soil. *Canadian Geotechnical Journal*, *47(4)*, 451-460.

Lopez, G. P., Biebuyck, H. A., Frisbie, C. D., & Whitesides, G. M. (1993). Imaging of features on surfaces by condensation figures. *Science*, *260(5108)*, 647-649.

Lowry, M. I. and C. T. Miller (1995), Pore-scale modeling of nonwetting-phase residual in porous-media, *Water Resour Res*, *31(3)*, 455-473.

Lozano, C., Lumay, G., Zuriguel, I., Hidalgo, R. C., & Garcimartín, A. (2012). Breaking arches with vibrations: the role of defects. *Physical review letters*, *109(6)*, 068001.

Lu, N. and W. J. Likos (2004), Unsaturated Soil Mechanics, John Wiley & Sons, Inc., Hoboken, NJ.

Luo, D., Wang, F., Zhu, J., Cao, F., Liu, Y., Li, X., Willson, R. C., Yang, Z., Chu, C., & Ren, Z. (2016). Nanofluid of graphene-based amphiphilic Janus nanosheets for tertiary or enhanced oil recovery: High performance at low concentration. *Proceedings of the National Academy of Sciences, 113(28),* 7711-7716.

Lv, P., Xiang, Y., Xue, Y., Lin, H., & Duan, H. (2017). Morphological bubble evolution induced by air diffusion on submerged hydrophobic structures. *Physics of Fluids, 29(3),* 032001.

Ma, S., Mason, G., & Morrow, N. R. (1996). Effect of contact angle on drainage and imbibition in regular polygonal tubes. *Colloids and Surfaces A: Physicochemical and Engineering Aspects*, *117*(3), 273-291.

Maestro, A., Guzmán, E., Santini, E., Ravera, F., Liggieri, L., Ortega, F., & Rubio, R. G. (2012). Wettability of silica nanoparticle–surfactant nanocomposite interfacial layers. *Soft Matter, 8(3),* 837-843.

Maestro, A., Rio, E., Drenckhan, W., Langevin, D., & Salonen, A. (2014). Foams stabilised by mixtures of nanoparticles and oppositely charged surfactants: relationship between bubble shrinkage and foam coarsening. *Soft Matter, 10(36),* 6975-6983.

Mannheimer, R. J., & Oswald, C. J. (1993). Development of transparent porous media with permeabilities and porosities comparable to soils, aquifers, and petroleum reservoirs. *Ground Water, 31(5),* 781-788.

Marchi, M., Gottardi, G., & Soga, K. (2013). Fracturing pressure in clay.*Journal of Geotechnical and Geoenvironmental Engineering, 140(2),* 04013008.

Mason, G., & Morrow, N. R. (1984). Meniscus curvatures in capillaries of uniform cross-section. *Journal of the Chemical Society, Faraday Transactions 1: Physical Chemistry in Condensed Phases, 80(9),* 2375-2393.

Mason, G., & Morrow, N. R. (1991). Capillary behavior of a perfectly wetting liquid in irregular triangular tubes. *Journal of Colloid and Interface Science*, *141*(1), 262-274.

Mason, G., & Morrow, N. R. (1994). Effect of contact angle on capillary displacement curvatures in pore throats formed by spheres. *J. of colloid and interface science*, *168*(1), 130-141.

Massoudi, R., & King Jr, A. D. (1974). Effect of pressure on the surface tension of water. Adsorption of low molecular weight gases on water at 25. deg. *The Journal of Physical Chemistry*, *78*(22), 2262-2266.

McCloud, K. V., & Maher, J. V. (1995). Experimental perturbations to Saffman-Taylor flow. *Physics Reports, 260(3),* 139-185.

McGrail, B. P., Schaef, H. T., Glezakou, V. A., Dang, L. X., & Owen, A. T. (2009). Water reactivity in the liquid and supercritical CO_2 phase: Has half the story been neglected?. *Energy Procedia, 1(1),* 3415-3419.

McLean, J. W., & Saffman, P. G. (1981). The effect of surface tension on the shape of fingers in a Hele Shaw cell. *Journal of Fluid Mechanics, 102*, 455-469.

Mei, Y., Li, G., Moldenaers, P., & Cardinaels, R. (2016). Dynamics of particle-covered droplets in shear flow: unusual breakup and deformation hysteresis. *Soft matter, 12(47)*, 9407-9412.

Melrose, J. C. (1970). Interfacial phenomena as related to oil recovery mechanisms. *Canadian Journal of Chemical Engineering, 48(6),* 638.

Melrose, J. C. (1974). Role of capillary forces in detennining microscopic displacement efficiency for oil recovery by waterflooding. *Journal of Canadian Petroleum Technology, 13(04).*

Mendoza, A. J., Guzmán, E., Martínez-Pedrero, F., Ritacco, H., Rubio, R. G., Ortega, F., Starov, V. M., & Miller, R. (2014). Particle laden fluid interfaces: dynamics and interfacial rheology. *Advances in colloid and interface science, 206*, 303-319.

Mercer, J. W., & Cohen, R. M. (1990). A review of immiscible fluids in the subsurface: properties, models, characterization and remediation. *Journal of Contaminant Hydrology, 6(2),* 107-163.

Meyer, E. E., Rosenberg, K. J., & Israelachvili, J. (2006). Recent progress in understanding hydrophobic interactions. *Proceedings of the National Academy of Sciences, 103*(43), 15739-15746.

Miller, R., P. Joos and V. B. Fainerman (1994), Dynamic surface and interfacial tensions of surfactant and polymer solutions, *Adv Colloid Interfac, 49*, 249-302.

Minagawa, H., Y. Nishikawa, I. Ikeda, K. Miyazaki, N. Takahara, Y. Sakamoto, T. Komai and H. Narita (2008), Characterization of sand sediment by pore size distribution and permeability using proton nuclear magnetic resonance measurement, *J Geophys Res-Sol Ea, 113(B7)*

Mishra, H., Schrader, A. M., Lee, D. W., Gallo Jr, A., Chen, S. Y., Kaufman, Y., Das, S. & Israelachvili, J. N. (2016). Time-Dependent Wetting Behavior of PDMS Surfaces with Bioinspired, Hierarchical Structures. *ACS Applied Materials & Interfaces, 8(12),* 8168-8174.

Miwa, M., A. Nakajima, A. Fujishima, K. Hashimoto and T. Watanabe (2000), Effects of the surface roughness on sliding angles of water droplets on superhydrophobic surfaces, *Langmuir, 16(13),* 5754-5760.

Mix, A. W., & Giacomin, A. J. (2011). Standardized polymer durometry. *Journal of Testing and evaluation, 39*(4), 696-705.

Moebius, F., & Or, D. (2012). Interfacial jumps and pressure bursts during fluid displacement in interacting irregular capillaries. *Journal of colloid and interface science, 377(1),* 406-415.

Mohanty, K. K., Davis, H. T., & Scriven, L. E. (1987). Physics of oil entrapment in water-wet rock. *SPE Reservoir Engineering, 2*(01), 113-128.

Monteux, C., Kirkwood, J., Xu, H., Jung, E., & Fuller, G. G. (2007). Determining the mechanical response of particle-laden fluid interfaces using surface pressure isotherms and bulk pressure measurements of droplets. *Physical Chemistry Chemical Physics, 9(48),* 6344-6350.

Montgomery, J. H. (2007). Groundwater Chemicals Desk Reference. Taylor and Francis, Boca Raton, FL.

Morrow, N. R. (1970). Physics and thermodynamics of capillary action in porous media. *Industrial & Engineering Chemistry*, *62*(6), 32-56.

Morrow, N. R. (1990). Wettability and its effect on oil recovery. *Journal of Petroleum Technology*, *42*(12), 1-476.

Muggeridge, A., Cockin, A., Webb, K., Frampton, H., Collins, I., Moulds, T., & Salino, P. (2014). Recovery rates, enhanced oil recovery and technological limits. *Phil. Trans. R. Soc. A, 372(2006),* 20120320.

Mulligan, C. N., R. N. Yong and B. F. Gibbs (2001), Surfactant-enhanced remediation of contaminated soil: a review, *Eng Geol, 60(1-4),* 371-380.

Murdoch, L. C. (1993). Hydraulic fracturing of soil during laboratory experiments. Part 1. Methods and observations. *Geotechnique, 43(2),* 255-265.

Murdoch, L. C. (1993). Hydraulic fracturing of soil during laboratory experiments Part 2. Propagation. *Geotechnique, 43(2),* 267-276.

Mysels, K. J. (1986), Surface tension of solutions of pure sodium dodecyl sulfate, Langmuir, 2(4), 423-428.

Nakahara, H., S. Lee, M. P. Krafft and O. Shibata (2010), Fluorocarbon-hybrid pulmonary surfactants for replacement therapy - a Langmuir mono layer study, *Langmuir, 26(23),* 18256-18265.

Nazari Moghaddam, R., Bahramian, A., Fakhroueian, Z., Karimi, A., & Arya, S. (2015). Comparative study of using nanoparticles for enhanced oil recovery: wettability alteration of carbonate rocks. *Energy & Fuels, 29(4),* 2111-2119.

NI, Q., Hird, C. C., & Guymer, I. (2010). Physical modelling of pile penetration in clay using transparent soil and particle image velocimetry.*Géotechnique, 60(2),* 121-132.

Niezgodzinski, T., & Swiniarski, J. (2010). Numerical calculations of stability of spherical shells. *Mechanics and Mechanical Engineering*, *14*(2), 325-337

Nikolaides, M. G., Bausch, A. R., Hsu, M. F., Dinsmore, A. D., Brenner, M. P., Gay, C., & Weitz, D. A. (2002). Electric-field-induced capillary attraction between like-charged particles at liquid interfaces. *Nature, 420(6913),* 299.

Nikolov, A. D., D. T. Wasan, A. Chengara, K. Koczo, G. A. Policello and I. Kolossvary (2002), Superspreading driven by Marangoni flow, *Adv Colloid Interfac, 96(1-3),* 325-338.

Nordbotten, J. M., M. A. Celia and S. Bachu (2005), Injection and storage of CO2 in deep saline aquifers: Analytical solution for CO_2 plume evolution during injection, *Transport Porous Med, 58(3),* 339-360.

Nygård, R., Gutierrez, M., Bratli, R. K., & Høeg, K. (2006). Brittle-ductile transition, shear failure and leakage in shales and mudrocks. *Marine and Petroleum Geology, 23(2),* 201-212.

Oades, J. M. (1993). The role of biology in the formation, stabilization and degradation of soil structure. *Geoderma, 56(1-4),* 377-400.

Olivella Pastallé, S., & Alonso Pérez de Agreda, E. (2008). Gas flow through clay barriers. *G¿ otechnique, 58(3),* 157-176.

Oppenheimer, J., Rust, A. C., Cashman, K. V., & Sandnes, B. (2015). Gas migration regimes and outgassing in particle-rich suspensions. *Frontiers in Physics, 3*, 60.

Oren, P. E., Billiotte, J., & Pinczewski, W. V. (1992). Mobilization of waterflood residual oil by gas injection for water-wet conditions. *SPE Formation Evaluation, 7(01),* 70-78.

Payatakes, A. C. (1982). Dynamics of oil ganglia during immiscible displacement in water-wet porous media. *Annual Review of Fluid Mechanics, 14(1),* 365-393.

Peña, T. J., Carvalho, M. S., & Alvarado, V. (2009). Snap-off of a liquid drop immersed in another liquid flowing through a constricted capillary. *AIChE journal, 55*(8), 1993-1999.

Pietruszczak, S., & Pande, G. N. (1996). Constitutive relations for partially saturated soils containing gas inclusions. *Journal of geotechnical engineering, 122(1),* 50-59.

Planchette, C., Lorenceau, E., & Biance, A. L. (2012). Surface wave on a particle raft. *Soft Matter, 8(8),* 2444-2451.

Pocivavsek, L., Frey, S. L., Krishan, K., Gavrilov, K., Ruchala, P., Waring, A. J., Walther, F. J., Dennin, M., Witlen, T. A., & Lee, K. Y. C. (2008). Lateral stress relaxation and collapse in lipid monolayers. *Soft Matter, 4(10),* 2019-2029.

Podgorski, T., Flesselles, J. M., & Limat, L. (2001). Corners, cusps, and pearls in running drops. *Physical Review Letters, 87*(3), 036102.

Podgorski, T., Sostarecz, M. C., Zorman, S., & Belmonte, A. (2007). Fingering instabilities of a reactive micellar interface. *Physical Review E, 76(1),* 016202.

Powers, S. E., & Tamblin, M. E. (1995). Wettability of porous media after exposure to synthetic gasolines. *Journal of Contaminant Hydrology, 19*(2), 105-125.

Powers, S. E., Anckner, W. H., & Seacord, T. F. (1996). Wettability of NAPL-contaminated sands. *Journal of Environmental Engineering, 122*(10), 889-896.

Prosser, A. J. and E. I. Franses (2001), Adsorption and surface tension of ionic surfactants at the air-water interface: Review and evaluation of equilibrium models, *Colloid Surface A, 178(1-3),* 1-40.

Pruess, K. and J. Garcia (2002), Multiphase flow dynamics during CO_2 disposal into saline aquifers, *Environ Geol, 42(2-3),* 282-295.

Purcell, W. R. (1950), Interpretation of capillary pressure data, Petroleum Transactions, *AIME, 2(8),* 369-371.

Puzrin, A. M., Tront, J., Schmid, A., & Hughes, J. B. (2011). Engineered use of microbial gas production to decrease primary consolidation settlement in clayey soils. *Géotechnique*, *61*(9), 785-794.

Quéré, D. (2008). Wetting and roughness. *Annu. Rev. Mater. Res.*, *38*, 71-99.

Ransohoff, T. C., & Radke, C. J. (1988a). Laminar flow of a wetting liquid along the corners of a predominantly gas-occupied noncircular pore. *Journal of Colloid and Interface Science*, *121*(2), 392-401.

Ransohoff, T. C., & Radke, C. J. (1988b). Mechanisms of foam generation in glass-bead packs. *SPE reservoir engineering*, *3*(02), 573-585.

Ransohoff, T. C., P. A. Gauglitz and C. J. Radke (1987), Snap-off of gas-bubbles in smoothly constricted noncircular capillaries, *AIChE J, 33(5),* 753-765.

Rao, P. S. C., Annable, M. D., Sillan, R. K., Dai, D., Hatfield, K., Graham, W. D., Wood, A. L., & Enfield, C. G. (1997). Field-scale evaluation of in situ cosolvent flushing for enhanced aquifer remediation. *Water Resources Research, 33(12),* 2673-2686.

Rapacchietta, A. V., & Neumann, A. W. (1977). Force and free-energy analyses of small particles at fluid interfaces: II. Spheres. *Journal of Colloid and Interface Science, 59(3),* 555-567.

Ravera, F., Ferrari, M., Liggieri, L., Loglio, G., Santini, E., & Zanobini, A. (2008). Liquid–liquid interfacial properties of mixed nanoparticle–surfactant systems. *Colloids and Surfaces A: Physicochemical and Engineering Aspects, 323(1-3),* 99-108.

Ravera, F., Santini, E., Loglio, G., Ferrari, M., & Liggieri, L. (2006). Effect of nanoparticles on the interfacial properties of liquid/liquid and liquid/air surface layers. *The Journal of Physical Chemistry B, 110(39),* 19543-19551.

Razavi, S., Cao, K. D., Lin, B., Lee, K. Y. C., Tu, R. S., & Kretzschmar, I. (2015). Collapse of particle-laden interfaces under compression: buckling vs particle expulsion. *Langmuir, 31(28),* 7764-7775.

Rebata-Landa, V., & Santamarina, J. C. (2012). Mechanical effects of biogenic nitrogen gas bubbles in soils. *J. Geotechnical and Geoenvironmental Engineering*, *138*(2), 128-137.

Reddy, K. R. and R. E. Saichek (2003), Effect of soil type on electrokinetic removal of phenanthrene using surfactants and cosolvents, *J Environ Eng-Asce, 129(4),* 336-346.

Riboulot, V., Sultan, N., Imbert, P., & Ker, S. (2016). Initiation of gas-hydrate pockmark in deep-water Nigeria: Geo-mechanical analysis and modelling. *Earth and Planetary Science Letters*, *434*, 252-26

Richards Jr, R., & Mark, R. (1966). Gelatin models for photoelastic analysis of gravity structures. *Experimental Mechanics, 6(1),* 30-38.

Roof, J. G. (1970). Snap-off of oil droplets in water-wet pores. *Society of Petroleum Engineers Journal*, *10*(01), 85-90.

Rose, W. and R. W. Heins (1962), Moving interfaces and contact angle rate-dependency, *J Coll Sci, 17(1),* 39-48.

Rosen, M. J. (2004), *Surfactants and Interfacial Phenomena*, John Wiley & Sons. Haboken, NJ.

Rossen, W. R. (2003). A critical review of Roof snap-off as a mechanism of steady-state foam generation in homogeneous porous media. *Colloids and Surfaces A: Physicochemical and Engineering Aspects*, *225*(1), 1-24.

Rühs, P. A., Böni, L., Fuller, G. G., Inglis, R. F., & Fischer, P. (2013). In-situ quantification of the interfacial rheological response of bacterial biofilms to environmental stimuli. *PLoS One, 8(11),* e78524.

Sadek, S., Iskander, M. G., & Liu, J. (2002). Geotechnical properties of transparent silica. *Canadian Geotechnical Journal, 39(1),* 111-124.

Saenton, S., T. H. Illangasekare, K. Soga and T. A. Saba (2002), Effects of source zone heterogeneity on surfactant-enhanced NAPL dissolution and resulting remediation end-points, *J Contam Hydrol, 59(1-2),* 27-44.

Saffman, P. G., & Taylor, G. (1958). The Penetration of a Fluid into a Porous Medium or Hele-Shaw Cell Containing a More Viscous Liquid. *Proceedings of the Royal Society of London Series A, 245,* 312-329.

Sahloul, N. A., Ioannidis, M. A., & Chatzis, I. (2002). Dissolution of residual non-aqueous phase liquids in porous media: pore-scale mechanisms and mass transfer rates. *Advances in Water Resources, 25(1),* 33-49.

Sandnes, B., Flekkøy, E. G., Knudsen, H. A., Måløy, K. J., & See, H. (2011). Patterns and flow in frictional fluid dynamics. *Nature communications, 2,* 288.

Santamarina, J. C. (2003). Soil behavior at the microscale: particle forces.*Geotechnical Special Publication, 25-56.*

Santamarina, J. C., & Jang, J. (2010). Energy geotechnology: Implications of mixed fluid conditions. In *International conference on unsaturated soils,* Sep. 6-8, Barcelona, Spain.

Santamarina, J. C., Klein, K. A., Wang, Y. H., & Prencke, E. (2002). Specific surface: determination and relevance. *Canadian Geotechnical Journal, 39(1),* 233-241.

Santamarina, J.C., in collaboration with Klein, K. and Fam, M. (2001). *Soils and Waves*, J. Wiley and Sons, Chichester, UK.

Santini, E., Krägel, J., Ravera, F., Liggieri, L., & Miller, R. (2011). Study of the monolayer structure and wettability properties of silica nanoparticles and CTAB using the Langmuir trough technique. *Colloids and Surfaces A: Physicochemical and Engineering Aspects, 382(1),* 186-191.

Santos, L. P., Ducati, T. R., Balestrin, L. B., & Galembeck, F. (2011). Water with excess electric charge. *The Journal of Physical Chemistry C*, *115*(22), 11226-11232.

Sassen, R., Losh, S. L., Cathles, L., Roberts, H. H., Whelan, J. K., Milkov, A. V., Sweet, S. T., & DeFreitas, D. A. (2001). Massive vein-filling gas hydrate: relation to ongoing gas migration from the deep subsurface in the Gulf of Mexico.*Marine and Petroleum Geology, 18(5),* 551-560.

Sauter, E. J., Muyakshin, S. I., Charlou, J. L., Schlüter, M., Boetius, A., Jerosch, K., Damm, E., Foucher, J., & Klages, M. (2006). Methane discharge from a deep-sea submarine mud volcano into the upper water column by gas hydrate-coated methane bubbles. *Earth and Planetary Science Letters, 243(3),* 354-365.

Scandella, B. P., Varadharajan, C., Hemond, H. F., Ruppel, C., & Juanes, R. (2011). A conduit dilation model of methane venting from lake sediments.*Geophysical Research Letters, 38(6).*

Schlüter, S., Berg, S., Li, T., Vogel, H. J., & Wildenschild, D. (2017). Time scales of relaxation dynamics during transient conditions in two-phase flow. *Water Resources Research.*

Schlüter, S., Berg, S., Rücker, M., Armstrong, R. T., Vogel, H. J., Hilfer, R., & Wildenschild, D. (2016). Pore-scale displacement mechanisms as a source of hysteresis for two-phase flow in porous media. *Water Resources Research, 52(3),* 2194-2205.

Schofield, A. N. (1980). Cambridge geotechnical centrifuge operations.Geotechnique, 30(3), 227-268.

Schramm, L. L. and F. Wassmuth (1994), *Foams: basic principles*, Foams: Fundamentals and Applications in the Petroleum Industry. Schramm, L. ed, American Chemical Society, Washington, DC.

Schulz, J. C. and G. G. Warr (2002), Adsorbed layer structure of cationic and anionic surfactants on mineral oxide surfaces, *Langmuir, 18(8),* 3191-3197.

Scriven, L. E. and C. V. Sternling (1960), Marangoni effects, *Nature, 187(4733),* 186-188.

Serrano, R. F., Iskander, M., & Tabe, K. (2011). 3D contaminant flow imaging in transparent granular porous media. *Géotechnique Letters, 1(3),* 71-78.

Sharma, R. and D. S. Ross (1991), Kinetics of liquid penetration into periodically constricted capillaries, *J Chem Soc Faraday T, 87(4),* 619-624.

Shin, H., & Santamarina, J. C. (2010). Fluid-driven fractures in uncemented sediments: Underlying particle-level processes. *Earth and Planetary Science Letters*, *299*(1), 180-189.

Shin, H., & Santamarina, J. C. (2011a). Desiccation cracks in saturated fine-grained soils: particle-level phenomena and effective-stress analysis. *Géotechnique*, *61*(11), 961-972.

Shin, H., & Santamarina, J. C. (2011b). Open-mode discontinuities in soils. *Géotechnique Letters*, *1*(4), 95-99.

Shin, H., Santamarina, J. C., & Cartwright, J. A. (2008). Contraction-driven shear failure in compacting uncemented sediments. *Geology, 36(12)*, 931-934.

Shin, H., Santamarina, J. C., & Cartwright, J. A. (2010). Displacement field in contraction-driven faults. *Journal of Geophysical Research: Solid Earth,115(B7).*

Sicard, F. X., & Striolo, A. (2017). Buckling in Armored Droplets. *Nanoscale.*

Siebold, A., M. Nardin, J. Schultz, A. Walliser and M. Oppliger (2000), Effect of dynamic contact angle on capillary rise phenomena, *Colloid Surface A, 161(1),* 81-87.

Sills, G. C., & Wheeler, S. J. (1992). The significance of gas for offshore operations. *Continental Shelf Research*, *12*(10), 1239-1250.

Sills, G. C., Wheeler, S. J., Thomas, S. D., & Gardner, T. N. (1991). Behaviour of offshore soils containing gas bubbles. *Geotechnique*, *41*(2), 227-241.

Singh, K., Scholl, H., Brinkmann, M., Di Michiel, M., Scheel, M., Herminghaus, S., & Seemann, R. (2017). The role of local instabilities in fluid invasion into permeable media. *Scientific reports, 7(1),* 444.

Skarke, A., Ruppel, C., Kodis, M., Brothers, D., & Lobecker, E. (2014). Widespread methane leakage from the sea floor on the northern US Atlantic margin. *Nature Geoscience, 7(9),* 657-661.

Snoeijer, J. H., & Andreotti, B. (2013). Moving contact lines: scales, regimes, and dynamical transitions. *Annual review of fluid mechanics*, *45*, 269-292.

Sobolev, V. D., Churaev, N. V., Velarde, M. G., & Zorin, Z. M. (2000). Surface tension and dynamic contact angle of water in thin quartz capillaries. *Journal of colloid and interface science*, *222*(1), 51-54.

Soga, K., Page, J. W. E., & Illangasekare, T. H. (2004). A review of NAPL source zone remediation efficiency and the mass flux approach. *Journal of Hazardous Materials, 110(1),* 13-27.

Song, W. and A. R. Kovscek (2015), Functionalization of micromodels with kaolinite for investigation of low salinity oil-recovery processes, *Lab Chip, 15(16),* 3314-3325.

Spycher, N., Pruess, K., & Ennis-King, J. (2003). CO_2-H_2O mixtures in the geological sequestration of CO_2. I. Assessment and calculation of mutual solubilities from 12 to 100 C and up to 600 bar. *Geochimica et cosmochimica acta, 67(16),* 3015-3031.

Stachowiak, J. C., Schmid, E. M., Ryan, C. J., Ann, H. S., Sasaki, D. Y., Sherman, M. B., Geissler, P. L., Fletcher, D. A., & Hayden, C. C. (2012). Membrane bending by protein–protein crowding. *Nature cell biology, 14(9),* 944.

StewartáRoss, D. (1991). Kinetics of liquid penetration into periodically constricted capillaries. *Journal of the Chemical Society, Faraday Transactions, 87(4),* 619-624.

Still, T., P. J. Yunker and A. G. Yodh (2012), Surfactant-induced Marangoni eddies alter the coffee-rings of evaporating colloidal drops, *Langmuir, 28(11),* 4984-4988.

Stokes, J. P., D. A. Weitz, J. P. Gollub, A. Dougherty, M. O. Robbins, P. M. Chaikin and H. M. Lindsay (1986), Interfacial stability of immiscible displacement in a porous-medium, *Phys Rev Lett, 57(14),* 1718-1721.

Subramaniam, A. B., Abkarian, M., Mahadevan, L., & Stone, H. A. (2006). Mechanics of interfacial composite materials. *Langmuir, 22(24),* 10204-10208.

Sun, Z., Jang, J. and Santamarina, J.C. (2017). Long-term pore filling – Implications in reservoir formation and resource recovery. Submitted for publication – Available from the authors.

Tabeling, P., Zocchi, G., & Libchaber, A. (1987). An experimental study of the Saffman-Taylor instability. *Journal of Fluid Mechanics*, *177*, 67-82.

Tadmor, R. (2009), Marangoni flow revisited, *J Colloid Interf Sci, 332(2),* 451-454.

Taina, I. A., Heck, R. J., & Elliot, T. R. (2008). Application of X-ray computed tomography to soil science: A literature review. *Canadian Journal of Soil Science, 88(1),* 1-19.

Take, W. A. (2015). Thirty-Sixth Canadian Geotechnical Colloquium: Advances in visualization of geotechnical processes through digital image correlation. *Canadian Geotechnical Journal, 52(9),* 1199-1220.

Tang, H., Grivas, W., Homentcovschi, D., Geer, J., & Singler, T. (2000). Stability considerations associated with the meniscoid particle band at advancing interfaces in Hele-Shaw suspension flows. *Physical Review Letters, 85(10),* 2112.

Tarantino, A. (2009). A water retention model for deformable soils. *Géotechnique*, *59*(9), 751-762.

Tary, J. B., Geli, L., Guennou, C., Henry, P., Sultan, N., Çağatay, N., & Vidal, V. (2012). Microevents produced by gas migration and expulsion at the seabed: a study based on sea bottom recordings from the Sea of Marmara.*Geophysical Journal International, 190(2),* 993-1007.

Thomson, W. (1886), Capillary attraction, *Nature, 34,* 270-272.

Thusyanthan, N. I., Take, W. A., Madabhushi, S. P. G., & Bolton, M. D. (2007). Crack initiation in clay observed in beam bending. *Geotechnique,57(7),* 581-594.

Trojer, M., M. L. Szulczewski and R. Juanes (2015), Stabilizing fluid-fluid displacements in porous media through wettability alteration, *Phys Rev Appl, 3(5),* 054008.

Unsal, E., Mason, G., Morrow, N. R., & Ruth, D. W. (2007). Co-current and counter-current imbibition in independent tubes of non-axisymmetric geometry. *Journal of colloid and interface science, 306(1),* 105-117.

Urso, M. E. D., C. J. Lawrence and M. J. Adams (1999), Pendular, funicular, and capillary bridges: Results for two dimensions, *J Colloid Interf Sci, 220(1),* 42-56.

Van Genuchten, M. T. (1980). A closed-form equation for predicting the hydraulic conductivity of unsaturated soils. *Soil science society of America journal*, *44*(5), 892-898.

van Kesteren, W., & van Kessel, T. (2002). Gas bubble nucleation and growth in cohesive sediments. *Proceedings in Marine Science*, *5*, 329-341.

Varanasi, K. K., Hsu, M., Bhate, N., Yang, W., & Deng, T. (2009). Spatial control in the heterogeneous nucleation of water. *Applied Physics Letters, 95(9),* 094101.

Vargaftik, N. B., B. N. Volkov and L. D. Voljak (1983), International tables of the surface tension of water, *J Phys Chem Ref Data, 12(3),* 817-820.

Vella, D., Aussillous, P., & Mahadevan, L. (2004). Elasticity of an interfacial particle raft. *EPL (Europhysics Letters), 68(2),* 212.

Vesic, A. S. (1972). Expansion of cavities in infinite soil mass. *Journal of Soil Mechanics & Foundations Div, 98(sm3).*

Vliegenthart, G. A., & Gompper, G. (2011). Compression, crumpling and collapse of spherical shells and capsules. *New Journal of Physics, 13*(4), 045020.

Wang, B., Socolofsky, S. A., Breier, J. A., & Seewald, J. S. (2016). Observations of bubbles in natural seep flares at MC 118 and GC 600 using in situ quantitative imaging. *Journal of Geophysical Research: Oceans,121(4),* 2203-2230.

Ward, A. F. H., & Tordai, L. (1946). Time-dependence of boundary tensions of solutions I. The role of diffusion in time-effects. *The Journal of Chemical Physics, 14(7),* 453-461.

Wardlaw, N. C. (1982). The effects of geometry, wettability, viscosity and interfacial tension on trapping in single pore-throat pairs. *J. Canadian Petroleum Technology*, *21*(03), 21-27

Washburn, E. W. (1921), The dynamics of capillary flow, *Phys Rev, 17,* 273-283.

Weislogel, M. M. (1996). Capillary Flow in an Interior Corner. *NASA Technical Memorandum 107364*.

Weislogel, M. M. and S. Lichter (1998), Capillary flow in an interior corner, *J Fluid Mech, 373*, 349-378.

Weissenborn, P. K., & Pugh, R. J. (1996). Surface tension of aqueous solutions of electrolytes: relationship with ion hydration, oxygen solubility, and bubble coalescence. *Journal of Colloid and Interface Science*, *184*(2), 550-563.

Wenzel, R. N. (1936), Resistance of solid surfaces to wetting by water, *Ind Eng Chem, 28(8),* 988-994.

Westbrook, G. K., Thatcher, K. E., Rohling, E. J., Piotrowski, A. M., Pälike, H., Osborne, A. H., ... & Hühnerbach, V. (2009). Escape of methane gas from the seabed along the West Spitsbergen continental margin. *Geophysical Research Letters, 36(15).*

Wheeler, S. J. (1988). A conceptual model for soils containing large gas bubbles. *Geotechnique, 38(3),* 389-397.

Wheeler, S. J. (1990). Movement of large gas bubbles in unsaturated fine-grained sediments. *Marine Georesources & Geotechnology, 9(2),* 113-129.

Wheeler, S. J., Sharma, R. S., & Buisson, M. S. R. (2003). Coupling of hydraulic hysteresis and stress-strain behaviour in unsaturated soils. *Géotechnique*, *53*(1), 41-54.

White, D. J., Take, W. A., & Bolton, M. D. (2003). Soil deformation measurement using particle image velocimetry (PIV) and photogrammetry. *Geotechnique, 53(7),* 619-632.

Wong, T. F., & Baud, P. (2012). The brittle-ductile transition in porous rock: A review. *Journal of Structural Geology,* 44, 25-53.

Wood, D. M. (1990). *Soil behaviour and critical state soil mechanics.* Cambridge university press.

Worthen, A. J., Parikh, P. S., Chen, Y., Bryant, S. L., Huh, C., & Johnston, K. P. (2014). Carbon dioxide-in-water foams stabilized with a mixture of nanoparticles and surfactant for CO2 storage and utilization applications. *Energy Procedia, 63,* 7929-7938.

Xia, H. W., & Moore, I. D. (2006). Estimation of maximum mud pressure in purely cohesive material during directional drilling. *Geomechanics and Geoengineering: An International Journal, 1(1),* 3-11.

Xue, H. T., Z. N. Fang, Y. Yang, J. P. Huang and L. W. Zhou (2006), Contact angle determined by spontaneous dynamic capillary, *Chem Phys Lett, 432(1-3),* 326-330.

Yazhgur, P. A., Noskov, B. A., Liggieri, L., Lin, S. Y., Loglio, G., Miller, R., & Ravera, F. (2013). Dynamic properties of mixed nanoparticle/surfactant adsorption layers. *Soft Matter, 9(12),* 3305-3314.

Young, T. (1804), An essay on the cohesion of fluids, *Philos Trans R Soc London, 95,* 65-87.

Yu, H. S. (2013). *Cavity expansion methods in geomechanics*. Springer Science & Business Media.

Yu, H. S., & Rowe, R. K. (1999). Plasticity solutions for soil behaviour around contracting cavities and tunnels. *International Journal for Numerical and Analytical Methods in Geomechanics,* 23(12), 1245-1279.

Yu, L., & Wardlaw, N. C. (1986a). The influence of wettability and critical pore-throat size ratio on snap—off. *Journal of Colloid and Interface Science, 109*(2), 461-472.

Yu, L., & Wardlaw, N. C. (1986b). Mechanisms of nonwetting phase trapping during imbibition at slow rates. *Journal of colloid and interface science*, *109*(2), 473-486.

Zang, D. Y., Rio, E., Langevin, D., Wei, B., & Binks, B. P. (2010). Viscoelastic properties of silica nanoparticle monolayers at the air-water interface. *The European Physical Journal E: Soft Matter and Biological Physics, 31(2),* 125-134.

Zhang, C., Oostrom, M., Wietsma, T. W., Grate, J. W., & Warner, M. G. (2011). Influence of viscous and capillary forces on immiscible fluid displacement: Pore-scale experimental study in a water-wet micromodel demonstrating viscous and capillary fingering. *Energy & Fuels, 25(8),* 3493-3505.

Zhang, R. and P. Somasundaran (2006), Advances in adsorption of surfactants and their mixtures at solid/solution interfaces, *Adv Colloid Interfac, 123,* 213-229.

Zhang, T., Davidson, D., Bryant, S. L., & Huh, C. (2010). Nanoparticle-stabilized emulsions for applications in enhanced oil recovery. In *SPE improved oil recovery symposium*. Society of Petroleum Engineers.

Zhang, W., Li, Y., Xu, T., Cheng, H., Zheng, Y., & Xiong, P. (2009). Long-term variations of CO_2 trapped in different mechanisms in deep saline formations: a case study of the Songliao Basin, China. *International journal of greenhouse gas control, 3(2),* 161-180.

Zhao, B., MacMinn, C. W., & Juanes, R. (2016). Wettability control on multiphase flow in patterned microfluidics. *Proceedings of the National Academy of Sciences, 113(37),* 10251-10256.

Zhao, H., & Beysens, D. (1995). From droplet growth to film growth on a heterogeneous surface: condensation associated with a wettability gradient. *Langmuir, 11(2),* 627-634.

Zhou, D., & Blunt, M. (1997). Effect of spreading coefficient on the distribution of light non-aqueous phase liquid in the subsurface. *Journal of Contaminant Hydrology*, *25*(1-2), 1-19.

Zocchi, G., Shaw, B. E., Libchaber, A., & Kadanoff, L. P. (1987). Finger narrowing under local perturbations in the Saffman-Taylor problem. *Physical Review A, 36(4),* 1894.